University of Bergamo

PhD in Engineering and applied sciences - XXVI Cycle

Technologies for Energy and Environment

~ · ~

Academic Year 2022–2023

Three-dimensional unsteady CFD modeling of vertical axis wind turbines at different operating conditions: design issues and physical interpretations

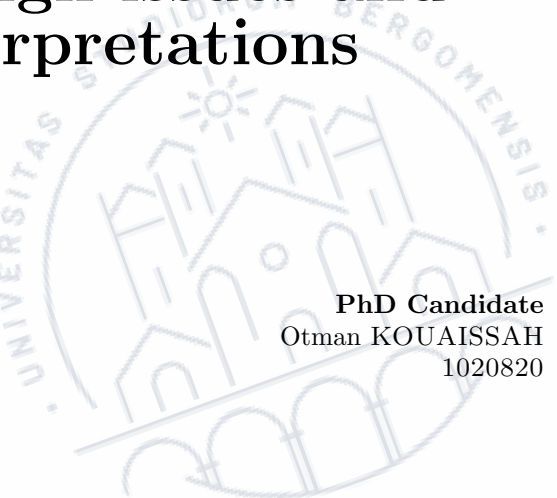

Supervisor
Prof.ssa Nicoletta Franchina

PhD Candidate
Otman KOUAISSAH
1020820

Final examination date: January 26, 2024

A mia mamma, mio padre, mia moglie, miei futuri figli e tutta la famiglia.

Acknowledgments

Completing this thesis would not have been possible without the support and guidance of numerous individuals, to whom I am deeply grateful. First and foremost, I would like to express my sincere gratitude to my thesis advisors, Nicoletta Franchina and Marco Savini. Their expertise, patience, and unwavering commitment to my success have been instrumental in guiding me through the research process. I am immensely grateful for the time and effort they invested in me and for their invaluable feedback and encouragement. I would also like to express my appreciation to Giacomo Persico for providing experimental data, and for his time and energy to participate in my study. Without the contributions of all, this research would not have been possible.

In addition to my academic advisors, I'm for sure indebted to my parents, my wife, and all my family members, friends, and colleagues, who have supported me throughout my academic journey. Their unchanging belief in me, their encouragement, and their love have been a source of motivation and inspiration, and I am truly fortunate to have them in my life.

Finally, I would like to thank the University of Bergamo, for the financial support and resources, which have enabled me to pursue this research. Their investment in my education and research has been instrumental in shaping my academic journey, and I am grateful for their contributions.

To everyone who has supported me along the way, thank you from the bottom of my heart. This thesis is the culmination of years of hard work, dedication, and perseverance, and I could not have done it without you.

Abstract

The shift towards greater use of renewable energy necessitates dependable, cutting-edge technical solutions that are both efficient and cost-effective. Wind energy possesses significant potential to fulfill this requirement. Vertical axis wind turbines (VAWTs) are ideally suited for the growing market of floating offshore wind and could reduce the levelized cost of energy for offshore platforms. The flow field around a VAWT rotor, in contrast, is characterized by its unsteadiness and complete three-dimensionality, primarily stemming from the interaction between the rotor blades and vortical structures. High-fidelity CFD constitutes a crucial tool for investigating intricate flow structures and optimizing the wind turbine at a reduced cost. In the context of this doctoral thesis, this tool was employed to evaluate and analyze the performance and physical phenomena characterizing the flow field of three vertical-axis turbines Troposkein, Deepwind Demonstrator, and H-shaped VAWT. The first two were subjected to experimental study at the wind tunnel facility of Politecnico di Milano. The experimental data were indispensable in validating the numerical results obtained.

The first case of the study focused on the small-scale Troposkein turbine, where a set of two-dimensional simulations of the equatorial section of the machine were conducted to evaluate various spatial resolutions and three turbulence models based on eddy-viscosity, specifically k-omega SST, and k-omega SST with low-Reynolds formulation, and Spalart-Allmaras. Subsequently, comprehensive three-dimensional simulations were performed under conditions of peak power and high TSR, enabling a thorough assessment of the models in comparison to experimental results. This investigation delves into the aerodynamics of the turbine, encompassing its spanwise variability, and the flow patterns both around and downstream of the rotor, with a specific focus on the distinctive nature of the troposkein rotor wake and the associated tip vortices. Afterward, an analysis on how the blade design influences the machine aerodynamics was presented, revealing that rotors fabricated using the simplest and most cost-effective blade bending technique surpass configurations created by manufacturing blades with plan airfoil sections following the troposkein curve. Based on the numerical settings employed in the preceding case, the second case study delves into the behavior of the Deepwind demonstrator, evaluating its performance under conditions of peak power and off-design. This second study was essential in verifying whether the validated numerical setup for the first turbine could be adaptable to another turbine characterized by different airfoil profile, varying curvature, rotation speeds, and a different range of Reynolds numbers. This investigation encompasses the study of the small-scale model in both upright and tilted operation conditions, which commonly characterize floating offshore installations. The energy harvesting process and the establishment of the near wake were considered. Furthermore, an analysis of a full-scale rotor is performed to assess performance parameters under uniform flow conditions. These results furnish valuable insights for the improvement of future designs and their associated installations. The third case study entails an extensive 3D CFD investigation of the performance and wake development characteristics of a straight-blade H-shaped VAWT in both an upright and tilted configuration. The VAWT model is examined at both peak power and off-design TSR values. The assessments are conducted with a focus on the intricate 3D flow field and the development of the near-wake region. The findings underscore the substantial influence of factors such as the tilted operational setting, the swept area variation, the 3D flow originating from the struts, and the effects of finite blade geometry on the machine's performance. Various tilt angles were thoroughly examined. The study offers a thorough analysis of turbine aerodynamics and spanwise variations to elucidate the fluid-dynamic phenomena and their implications on energy harvesting.

Contents

Chapter 1

Wind Energy

1.1 Wind Energy Global Market Trends

The transition to net-zero world emissions presents a significant challenge that requires a fundamental transformation of energy production systems and practices. The International Energy Agency (IEA) reported that global CO2 emissions increased by 1.7% in 2021, following a significant 7% decrease in 2020 due to the impact of the COVID-19 pandemic. This rise can be attributed to the resurgence of global economic activities in the transport and industrial sectors. Notably, the energy sector remains the largest contributor to CO2 emissions, accounting for over 70% of global greenhouse gas emissions in 2021 (IEA, 2022a). Significant efforts are required to achieve the objectives outlined in the Paris Agreement and effectively limit global warming to 1.5°C. Emissions must be reduced by 45% within 2030 to facilitate achieving net-zero emissions by 2050 (UN, 2022). This ambitious target highlights the urgency for revolutionary actions across multiple sectors, including energy production, transportation, and industry. This includes accelerating the deployment of renewable energy sources such as solar and wind power, expanding energy efficiency measures, adopting electrification in transportation, and promoting sustainable practices in industries. While this task seems undoubtedly challenging, it also presents significant opportunities for innovation, job creation, and improved quality of life.

In fact, the increased demand for energy, the rising cost of fossil fuels due to the last geopolitical conflicts, and the widespread belief that man-made global warming is taking place are forcing the development of renewable energy technologies. Countless experts consider wind energy to be a highly attractive solution, due to the enormous potential of offshore technology (IEA 2022b). Therefore, wind energy can play a significant role in combating climate change by reducing emissions.

The wind energy industry has made substantial progress in recent years and has continued to evolve rapidly since 2000 (IRENA 2022). Over the past two decades, the global installed capacity of wind energy, both onshore and offshore, has grown significantly. According to IRENA's data, the global weighted-average levelized cost of electricity (LCOE) of onshore installation fell by 56%, from USD 0,089/kWh to USD 0,039/kWh. During the same time period, the LCOE for newly installed offshore wind projects fell by 48% (IRENA 2022). A decrease in LCOE has shown that wind energy has become an economically beneficial source of energy. In 2021, a total of 830 GW of wind capacity was installed, with the majority of 93% located onshore and the remaining 7% offshore. This was a record year for the global wind power industry with a growth of 17%, and was the highest growth rate among all renewable energy technologies (IEA 2022b). To meet the wind power target of 7900 TWh in 2030 set by the net-zero emission goal, an average annual

expansion rate of 18% is required between 2022 and 2030 (IEA 2022b).

Figure 1.1: Global wind power onshore and offshore, new and total installations [GWEC2022]

The global wind energy market has been attesting a significant upward trend in recent years, driven by various factors such as increasing environmental concerns, favorable government policies, technological advancements, and cost reductions. This trend is expected to continue in the foreseeable future, with several key market dynamics at play. Figure 1.1 provides an accurate representation of the global wind power landscape by presenting two significant aspects: the cumulative total of installed wind power across the world and the new installations in 2021. It includes both onshore and offshore wind energy installations, providing a complete view of the progress and expansion of wind power generation on a global scale.

In Asia, China has emerged as the world's largest market for wind power. The country has made significant investments in wind energy infrastructure, resulting in a substantial increase in installed capacity. China has a strong onshore wind energy sector, with a focus on large-scale wind farms in regions with favorable wind resources. The country is also rapidly expanding its offshore wind capacity along its coastal areas. In addition, Thailand, South Korea, and Japan have recently intensified their investments in the field of wind energy. Recognizing the importance of transitioning towards sustainable and renewable energy sources.

In Europe, the United Kingdom has experienced significant growth in both onshore and offshore wind power. It has been a leader in offshore wind development, with several large-scale projects operating in its waters. The UK has set ambitious targets to increase offshore wind capacity, aiming to become a global hub for offshore wind technology and expertise. Also, Germany has been at the forefront of wind energy development in Europe. The country has a well-established onshore wind sector and has been increasingly focusing on offshore wind projects in the North Sea and Baltic Sea. Germany has implemented supportive policies and feed-in tariffs

to incentivize wind energy investments. Denmark has a long-standing history in wind energy and has been a pioneer in the field. The country has a strong onshore wind sector and has been actively developing offshore wind projects in the North Sea. Denmark is known for its advanced wind turbine technology and has a strong focus on research and development in the wind energy sector. Last but not least, the Netherlands has experienced substantial growth in wind energy. With increasing installed capacity, active construction, and ambitious targets for the future, the country has demonstrated a strong commitment to renewable energy and is making significant strides in harnessing the potential of wind power.

In North America, several states in the US, including Texas, Iowa, and California, have abundant wind resources and have invested heavily in wind power installations. Offshore wind development has higher momentum, particularly along the East Coast, with multiple projects in various stages of planning and development. In South America, Brazil has a significant wind energy market, primarily driven by its strong onshore wind resources. The country has been rapidly expanding its wind power capacity, with a focus on large-scale wind farms in the northeastern region. Brazil has implemented actions and supportive policies to encourage wind energy development and diversify its energy mix.

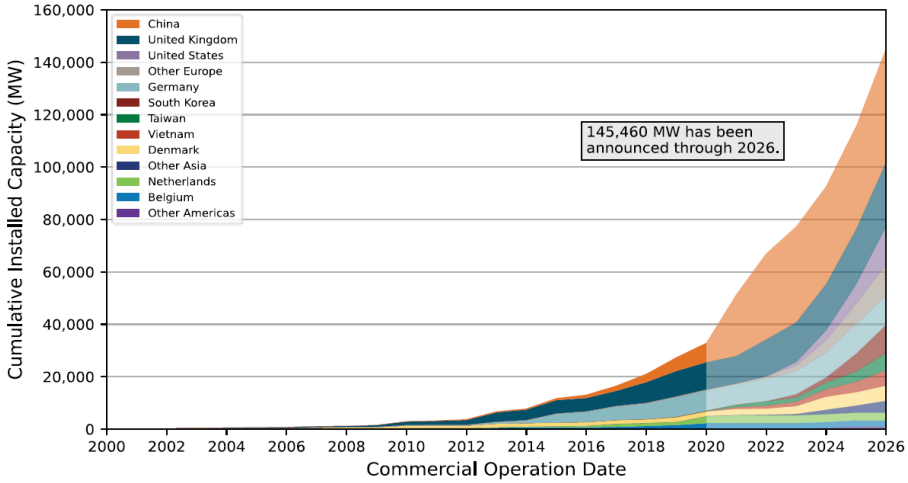

Figure 1.2: Estimated 2026 Cumulative Offshore Wind Capacity by Country Based on a Developer-Announced Commercial Operation Date[1]

Focusing more on offshore wind power, which as mentioned is also experiencing notable growth and is expected to become a key market segment. Offshore wind projects offer the potential for higher capacity installations, access to stronger and more consistent winds, and reduced visual impact compared to onshore projects.

As illustrated in Figure 1.2 [1], the estimated cumulative deployment of offshore wind energy by the year 2026 is projected to achieve an impressive capacity of around 145 GW. The rapid growth of the offshore wind energy sector, driven by advancements in technology, supportive government policies, and increasing investments, has led to substantial progress in harnessing the power of wind resources at sea. The anticipated 145 GW capacity demonstrates the significant contribution that offshore wind is making toward global renewable energy targets. This substantial deployment not only signifies the growing importance of offshore wind as a key player in the global energy transition but also highlights the industry's potential to continue its expansion in the coming years.

Technically, offshore wind energy can be deployed using two main technologies:
Fixed-bottom offshore wind refers to turbines that are firmly anchored to the seabed using foundations such as monopiles or jackets. This technology is suitable for water depths up to around 60 meters. Fixed-bottom platforms have been widely utilized and have a longer history of commercial deployment. They have proven to be reliable and cost-effective for shallow water locations. On the other hand, **floating offshore wind** involves turbines mounted on floating structures that are not fixed to the seabed. This technology enables the deployment of wind farms in deeper waters, conventionally greater than 50 meters, where fixed-bottom installations are not feasible. Floating platforms utilize various mooring systems to keep the turbines stable and in position. Although still in the early stages of commercialization, floating offshore wind has the potential to access larger wind resources in deep-water areas.

Figure 1.3 illustrates the global current status of the floating offshore wind energy market pipeline, focusing on various factors such as time, depth, project size, and country. The information presented covers projects up until 2026, specifically those that have reported water depth. Figure 1.3 demonstrates the evolution of the floating offshore wind energy market over time. Initially, there were small-scale prototypes with a single wind turbine between 2009 and 2015. This was followed by the development of multiturbine demonstration projects from 2016 to 2022. Beyond 2022, the industry anticipates the installation of the first commercial-scale floating offshore wind projects, which are expected to be significantly larger in size. As the project sizes increase, so do the water depths at which they are deployed.

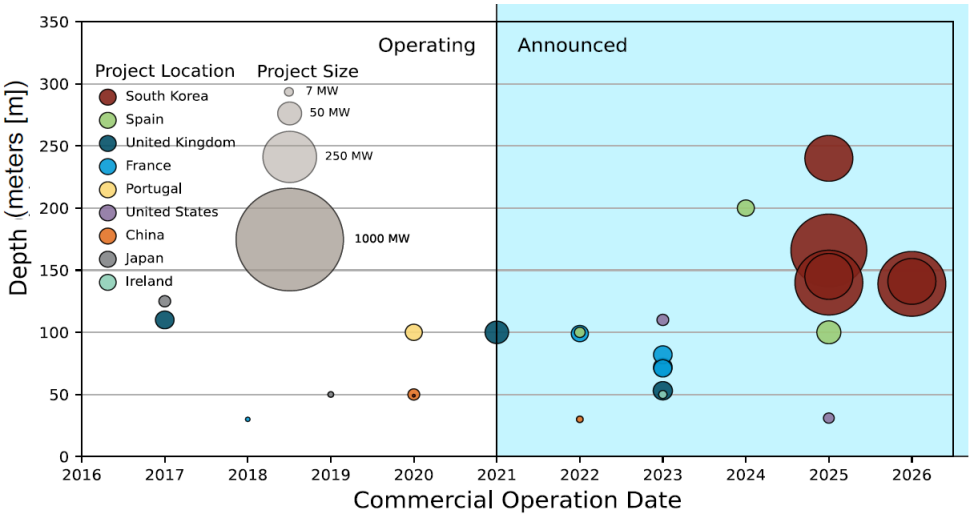

Figure 1.3: Global Floating Offshore Wind Energy Projects by Depth, Country, and Project Size[1]

As we will explore in the subsequent section, VAWTs demonstrate suitability for installation on floating platforms. Consequently, this integration of VAWTs on floating platforms has the potential to facilitate the expansion of wind energy into deeper waters.

1.2 VAWT's Technology

1.2.1 Introduction

Generating electrical energy from wind may seem simple at first glance. However, the rigorous description of fluid dynamics and the intricate design of the machine make it a highly complex process. Let's delve into the operating principle from an aerodynamic standpoint.

Wind power is a valuable resource that, to harness its potential, necessitates systems capable of converting a portion of kinetic energy into mechanical energy. This mechanical energy enables the rotation of the shaft in an electricity generator. Wind turbines are the specific devices we are referring to. They can be broadly categorized into two macro-families, depending on the orientation of the axis around which the rotor rotates: horizontal axis turbines (HAWTs) and vertical axis turbines (VAWTs). The majority of existing wind turbines are horizontal-axis, which continues to dominate the wind market (Hand and Cashman 2020). This is likely due to their efficiency and the ability to make profitable, large-scale turbines (Cuevas-Carvajal et al. 2022). The size of HAWTs has increased rapidly, having reached turbines rated for 14 MW of power, with a rotor diameter of 236 m (Electrek 2023). One limitation of HAWTs is that they must face the incoming wind direction, which necessitates additional costs for yawing systems and drivetrains to be fully efficient. Additionally, the electric generator is placed on the top of the shaft, making maintenance complicated. The height of the center of mass also demands high structural integrity, especially in floating offshore applications.

In contrast, there are several reasons which encourage adopting the VAWT technology. Here, we simply list a selection of them:(i) The heavy components are at a low level, which increases the stability of the structure and reduces installation, operation, and maintenance costs.(ii) The lack of need for yaw control since by design, the VAWT has an omnidirectional nature. (iii) Employing a direct-drive generator (DDG), so the complex speed-increasing multistage gearbox, which causes 20% of HAWTs failure, can be eliminated [51, 88]. (iv) The energy deficit in the counter-rotating VAWTs wake can be recovered in reduced distance according to field experiments [47]. (v) Up-scaling the VAWT architecture for floating off-shore applications doesn't run into any significant obstacle, it can be developed to be substantially larger than conventional HAWT. According to estimates, a VAWT's maximum structural potential is around 30 MW [34]. It is obvious that VAWT technology offers a highly promising option to exploit the huge potential of offshore wind resources in deep water areas, where up to eighty percent of the global wind resource is located. According to SANDIA National Lab. a floating VAWT with an efficient mooring system, can offer a cost of energy (COE) reduction of 20%, in comparison with the conventional HAWT technology. Even though the advantages of this technology are well documented in the literature, employing VAWTs remains a significant challenge in the wind energy industry. To overcome this challenge and work towards the development of more efficient and reliable turbines, the VAWT's design cannot be separated from an adequate aerodynamic study covering all the various aspects that influence its operation.

Vertical-axis wind turbines (VAWTs) can be categorized into two subcategories based on the design principle employed for generating mechanical torque: those relying on drag and those utilizing lift.

- **Savonius wind turbine:** It is named after its Finnish inventor, Sigurd J. Savonius. From an aerodynamic perspective, this turbine operates based on the drag force. It comprises a rotor device with two or three semi-cylindrical blades. In a horizontal cross-section, the two-bladed configuration forms an S-shape, see Figure 1.4a. The curved blades capture and harness the incoming wind while allowing the wind flowing in the opposite direction to pass through more easily. Consequently, the blades encounter less resistance when moving

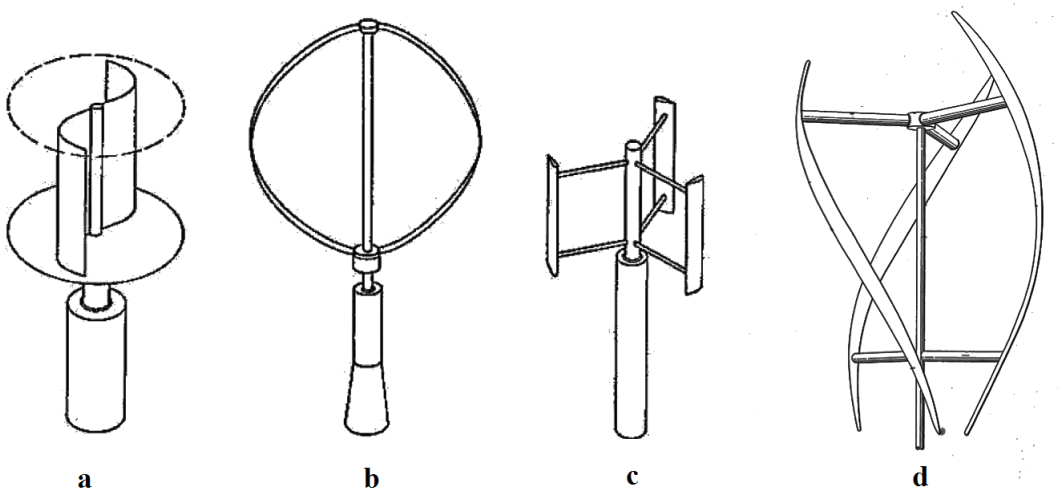

Figure 1.4: Classification of Vertical Axis Wind Turbines (VAWTs)

against the wind compared to when moving with the wind. This disparity in resistance causes the Savonius turbine to rotate. One notable feature of this turbine type is its ability to start automatically, which proves beneficial in overcoming the startup issues faced by Darrieus-type turbines.

- **Darrieus wind turbine:** This particular type of turbine was patented by George Darrieus in 1931, and it was named after him. Unlike the Savonius turbine, the Darrieus turbine relies on the principle of lift rather than drag from an aerodynamic standpoint. As a result, it exhibits higher efficiency. In fact, when the dimensions of the swept area are kept the same, they can generate approximately the same power as Horizontal-Axis Wind Turbines (HAWTs). Figure 1.4 illustrates the three configurations of Darrieus-type turbines (b, c, and d). These turbines would have gained significant popularity if not for their startup issue. To ensure that the lift generated on the turbine blades is capable of driving the generator, the rotor needs to reach a minimum speed. Therefore, a starting mechanism is often necessary.

In this thesis, as we will later explore, we will examine the Troposkien configuration 1.4b and H-shaped configuration 1.4c. Further detailed information regarding their geometric characteristics will be provided later.

1.2.2 VAWTs Applications

The primary application revolves around the utilization of the VAWTs in urban environments, where the wind flow tends to be less predictable. This unique characteristic of VAWTs sets them apart as a superior choice compared to traditional horizontal turbine structures, especially when it comes to accommodating the limitations imposed by urban environments. The less reliable wind patterns prevalent in cities and urban areas can pose significant challenges for the efficient operation of wind turbines. However, VAWTs demonstrate remarkable adaptability to such conditions, allowing them to effectively harness the available wind energy. Their vertical orientation enables them to capture wind from various directions, making them less dependent on consistent wind flow patterns. This flexibility ensures a more consistent power generation, even in turbulent urban environments. Furthermore, the compact design of VAWTs makes them highly suitable for on-ground installations in crowded urban spaces. Unlike taller horizontal turbines, VAWTs can be conveniently positioned closer to the ground, minimizing the impact on the surrounding landscape. This advantage not only facilitates easier integration into urban settings but also reduces potential aesthetic concerns associated with taller structures. Moreover, VAWTs offer an advantage by being mountable onto buildings and rooftops. This adaptability allows for the exploitation of otherwise underutilized spaces, such as the tops of buildings, where wind resources are often more accessible.

Figure 1.5: Exemplary Urban Applications of Vertical Axis Wind Turbines

As mentioned, another significant application of VAWTs is their deployment in floating offshore environments. By utilizing VAWTs in floating offshore installations, several advantages can be realized. The inherent design characteristics of VAWTs, such as their ability to capture wind from various directions, as well as having the heavier components at a lower level enhance the structural stability and result in cost reductions for installation, operation, and maintenance. This makes them well-suited for the dynamic and changing wind conditions experienced in offshore environments. In fact, in the last decade, multiple noteworthy projects have been developed, and a few notable examples include the European projects DeepWind [17, 19, 20], X-Rotor [63, 36], alongside emerging startup enterprises such as SeaTwirl [2] and World Wide Wind [3].

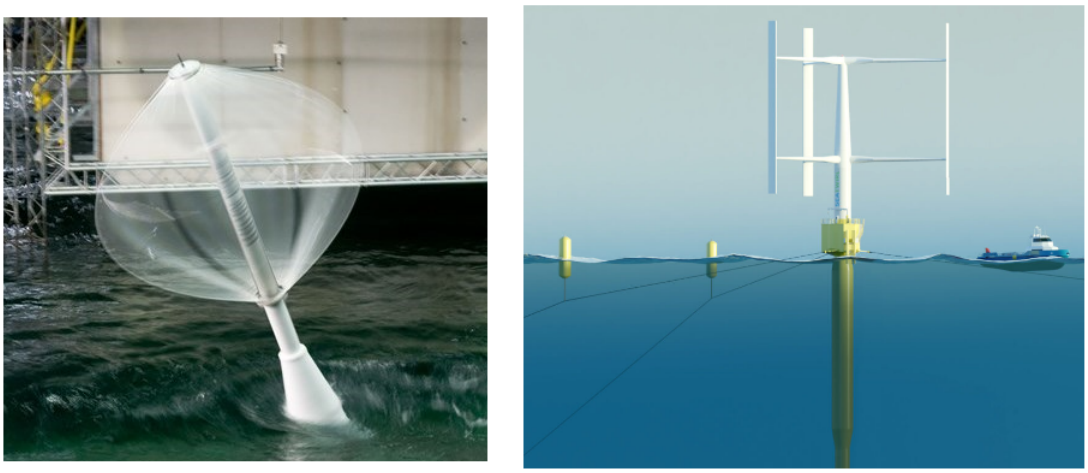

a b

Figure 1.6: Floating VAWTs Examples: a) DeepWind Project - b) 1MW SeaTwirl Prototype

1.2.3 VAWTs Terminology

In order to understand the core operating principle, it is necessary to define a few key terms. Commencing with the airfoil, which refers to the cross-sectional shape of a blade designed to generate lift. It play a crucial role in harnessing wind energy efficiently. It is also worth noting that the sections of turbo-machinery blades or propellers are constructed using airfoil concepts, as the wings of an airplane. Figure 1.7 summarises the main geometric parameters of an airfoil.

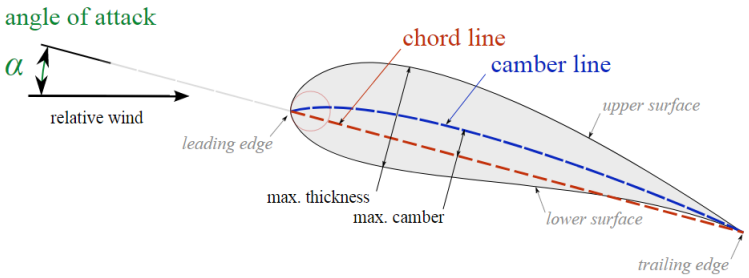

Figure 1.7: Key Geometric Parameters of an Airfoil

- **Chord line:** The chord of the airfoil is usually employed as the characteristic length for calculating the Reynolds number or to define the aerodynamic coefficients.
- **Camber line:** The mean line of the profile, representing its curvature. It's aligned with its chord in the case of symmetry and exhibiting a curved shape when asymmetrical.
- **Angle of attack:** It's the angle formed between the chord direction and the relative wind.
- **Max thickness:** The maximum thickness of the profile, it is usually located at quarter of the chord from its leading edge.
- **Leading Edge:** It's the part of profile which first meets the oncoming air. It's the point with the greatest curvature.
- **Trailing Edge:** It's the rear edge of the profile, characterised by minimal curvature.

The key outcome of aerodynamic analysis lies in determining the aerodynamic forces acting upon the airfoil. As a convention, the resulting aerodynamic force is typically decomposed into two components:

- **Lift:** Refers to the perpendicular component of aerodynamic force in relation to the direction of the oncoming flow. Generated by the pressure difference between the **pressure side** characterized by high pressure due to flow deceleration, and the **suction side** characterized by low pressure caused by to the flow acceleration.
- **Drag:** It is the component of aerodynamic force that acts parallel to the oncoming flow direction. This force consists of three primary terms: frictional resistance, form resistance, and induced resistance. Frictional resistance is primarily influenced by fluid viscosity, form resistance is associated with the specific shape of the body, and induced resistance is determined by the amount of downwash induced near the airfoil (this deviation in flow results in the airfoil behaving as if it had a reduced angle of incidence).

The two aerodynamic forces, which have been already defined, act along a line intersecting the chord at a specific location called the airfoil's center of pressure.
The two forces and the moment generated can be expressed in terms of dimensionless coefficients, named respectively the lift coefficient C_L, drag coefficient C_D and moment coefficient C_M. It is noteworthy that moments in this context must be referenced to a fixed point in space. Consequently, we can define two distinct moments: the first moment pertains to the airfoil and is defined in relation to the center of mass, while the second moment is relative to the turbine and is defined with respect to the axis of rotation.

- **Lift coefficient:**

$$C_L = \frac{L}{\frac{1}{2}\rho V^2 S}, \tag{1.1}$$

- **Drag coefficient:**

$$C_D = \frac{D}{\frac{1}{2}\rho V^2 S}, \tag{1.2}$$

where V is the wind speed, ρ is the density, and S is the swept area.

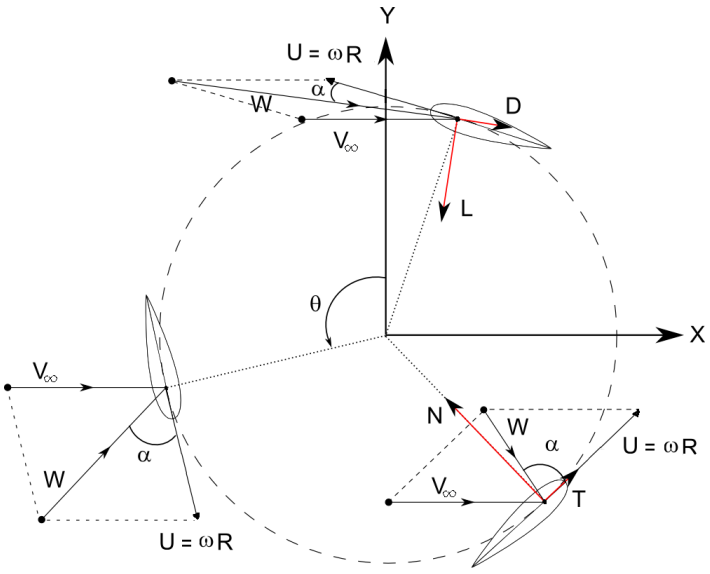

Figure 1.8: Aerodynamic Forces and Speed Triangles of VAWTs

In conjunction, the lift and drag give rise to the production of other two forces, the normal and tangential force, respectively equal to:

$$F_N = \tfrac{1}{2}\rho W^2 S C_N,$$

$$F_T = \tfrac{1}{2}\rho W^2 S C_T.$$

Where the normal coefficient C_N and the tangential coefficient C_T are defined as:

$$C_N = C_L cos\alpha + C_D sen\alpha,$$

$$C_T = C_L sen\alpha - C_D cos\alpha.$$

The moment generated by the forces:

$$M(\theta) = rF_T + bF_N = \frac{1}{2}\rho W^2 S[rC_T + bC_N], \tag{1.3}$$

where r is the turbine radius and b indicates the distance between the centre of pressure and the anchorage point. At this point we are able to define the **Moment Coefficient:**

$$C_M = \frac{M}{\frac{1}{2}\rho V^2 S}, \tag{1.4}$$

An important parameter to analyze the performance of wind turbines is the **Tip Speed Ratio** (TSR or λ), which is defined as the ratio between the peripheral speed of the blades and the speed of the incoming undisturbed wind.

$$\lambda = \frac{U}{V_\infty} = \frac{\pi D n}{V_\infty} = \frac{\omega r}{V_\infty}. \tag{1.5}$$

The efficiency and power output of a wind turbine are significantly influenced by the TSR. A higher TSR indicates that the blades are rotating at a faster speed compared to the incoming wind, which may result in increased power generation.

The angle of attack α, which is utilized to calculate C_T and C_N, is a function of the TSR and the azimuth position θ. It can be approximately expressed by the following equation:

$$\alpha = tan^{-1}\left(\frac{sin\theta}{cos\theta + \lambda}\right), \tag{1.6}$$

Figure 1.9 shows the variation of the angle of attack as a function of the azimuth angle, for three different TSR values:

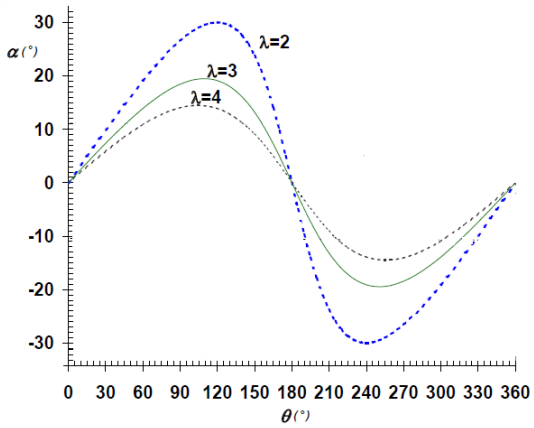

Figure 1.9: Variation of Airfoil Angle of Attack with TSR and Azimuthal Position

Figure 1.9 clearly illustrates the direct relationship between the decrease in Tip Speed Ratio (TSR) and the corresponding increase in the angle of attack. This indicates that the VAWT's blades are subjected to a greater chance of encountering stall occurrences during the revolution.

Consequently, it becomes imperative to introduce the definition of the power coefficient and clarify the process of calculating the power harvested by the wind turbine:

- **Power Coefficient:** $C_p = C_M \lambda$.
- **Harvested Power:** $P_{harvested} = \frac{1}{2} \rho C_p A V^3$.

Figure 1.10 illustrates the C_P vs TSR curve, for various wind turbine designs.

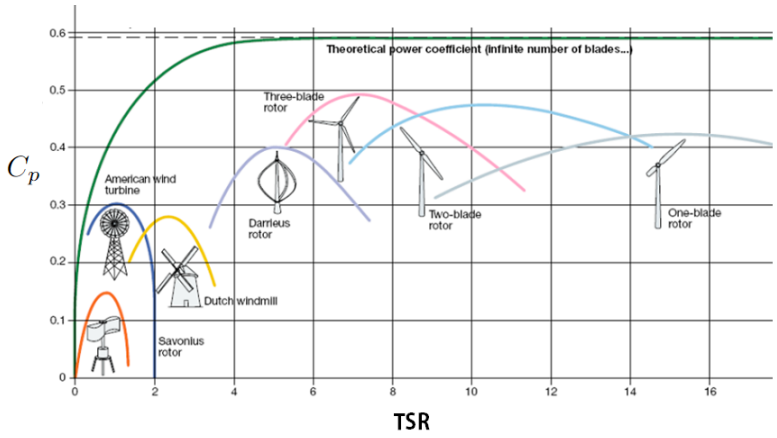

Figure 1.10: Power Coefficient of Wind Turbines as a Function of the TSR

Remarkably, as the TSR increases, the C_P also rises, reaching a peak value at an optimal TSR. This indicates that the turbine is efficiently converting wind energy into power. However, if the TSR continues to increase beyond this optimal point, the C_P gradually decreases due to factors such as increased drag and turbulence. Therefore, it is crucial to operate the wind turbine within the TSR range where the C_P is maximized to achieve the optimal power output. As mentioned above. the examined VAWTs are Darrieus rotors, which typically operate within a tip speed ratio (TSR) range of 3-7.

1.2.4 VAWT design parameters

There are many design parameters that affect the aerodynamic performance of the VAWT. In this section, a brief review of these design parameters shown in Figure 1.11 will be given.

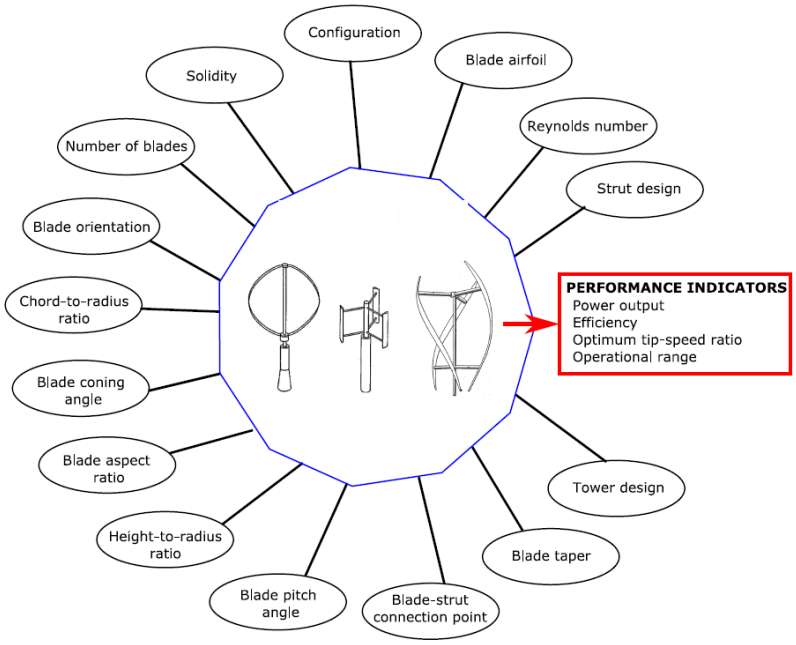

Figure 1.11: Key Design Parameters Impacting VAWT Performance

- **1- Solidity**:
  The VAWT solidity represents the ratio of the total blade plan-form area NcH to the turbine's swept area DH. This parameter has been defined in two forms, either σ= Nc/D or σ= Nc/R by various researchers. The latter definition, which is used predominately in the literature, is adopted. As reported in Figure 1.12, solidity has a significant impact on the aerodynamic performance of a VAWT, both on the C_P-max and the optimal TSR. The most noticeable effect of increased solidity is that the C_P curve is shifted to the left (lower TSRs torque), as well as a reduction in the range of turbine operation. A very low solidity is not desirable due to high rotation speed (high optimal-TSR), which means significant centrifugal loads, more blockage effect, and losses at the tip and on the struts. On the other hand, high solidity is not preferred from an aerodynamic point of view (i.e. operating in low optimal TSR means slower rotating, high torque, and dynamic stall (high AOA). It's recommended in the literature that the solidity must be between 0,2 and 0,3 [77, 27, 58, 25].

- **2- Number of blades**:
  The blade number is an important design element that must be balanced between the blade stiffness, aerodynamic efficiency, and economic considerations. The turbine solidity is directly proportional to the blade's number by definition. Blackwell et al. [23] investigated the blade number effect on the SNL 2-m turbine, maintaining the same solidity and chordal Reynolds number for two turbines (with 2 and 3 blades). It's clear, that to maintain the

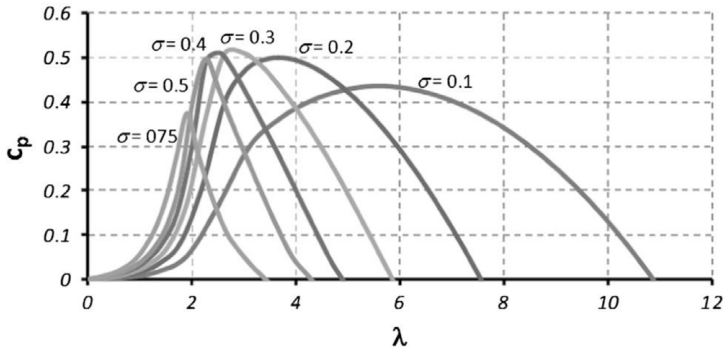

Figure 1.12: The power coefficient curve as a function turbine's solidity with straight NACA0018 blades [25]

same solidity the blade chord should be different, and so to maintain the same chordal number the rotation speed must be higher (1.5 times) in the 3-blade case. The peak efficiency was reached by both. But from the structural point of view, high rotation speed is not desirable (i.e. high centrifugal loads). Since the Reynolds number should be kept high, the study suggests the blade number should be small. Another important factor is that the blade number affects the global torque of the turbine, more blades create less changing instantaneous torque reducing the torque ripple. The VAWT's self-starting is also affected by the number of blades, and this ability improves as the blade's number is increased. However, it's commonly known that a low number of blades (2 or 3) is the most suitable solution.

- **3- Reynolds number**:
  The Reynolds number is an essential parameter in aerodynamics and it should always be taken into account while designing wind turbines. The higher the Reynolds number, the larger the airfoil static stall angle of attack. In fact, increasing the Reynolds number improves the VAWT's efficiency for the whole operation range, as exhibited in Figure 1.13. Increasing the Reynolds number causes a stall delay and so the optimum TSR decreases. This suggests that a wind farm with large-scale VAWTs (high Re) is more efficient than a farm with small-scale turbines covering the same area. Also, a high Reynolds number improves the self-starting ability which has encouraged the use of larger chords in the design of VAWTs [78].

- **4- Blade airfoil:**
  The VAWT COE is hugely affected by the blade airfoil. Furthermore, the airfoil selection affects the aerodynamic efficiency and structural integrity of each blade. The VAWT's unsteady behavior, with regular changes in the AOA and relative velocity, makes choosing a blade airfoil extremely difficult. The design parameters of the airfoil include the chord length, leading-edge radius, thickness-to-chord ratio, trailing edge profile, maximum thickness location, and percentage camber. These parameters are illustrated in Figure 1.7. The symmetrical 4-digit airfoils were used in the first VAWTs prototypes, from NACA 0012 (12% of thickness-to-chord ratio) to NACA 0021 (21%), (the latter is considered here). The operational nature of the VAWT was the first reason to choose these symmetrical airfoils, as the low-pressure surface and the high-pressure surface change during each turbine's revolution. The second reason is the huge availability of experimental data at

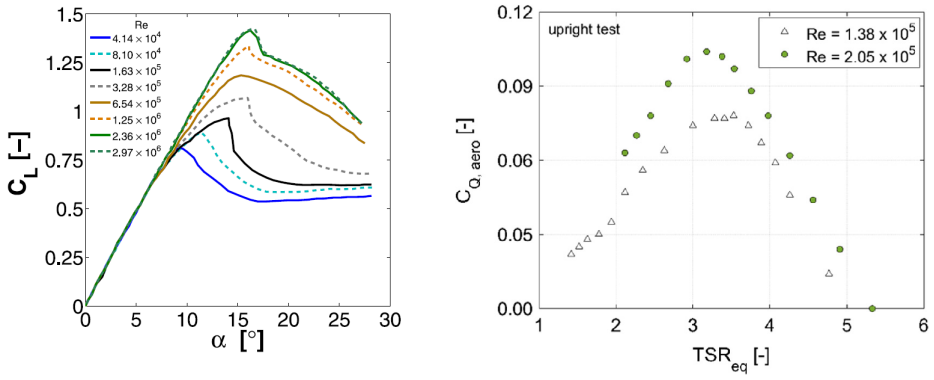

Figure 1.13: Reynolds effects on a Single Sirfoil[44], and on VAWT Performance[16]

different Reynolds numbers. The use of NACA 4-digit with a significant thickness-to-chord ratio (18% and 21%) is required from the structural stiffness standpoint, even if increasing this ratio, deteriorates the performance of the VAWTs from an aerodynamic viewpoint. Sandia National Laboratory developed the SAND airfoils, which were designed to produce NLF (natural laminar flow) over almost all of the blade chord due to the location of the maximum thickness (x/c about 40%). With this kind of blade, it was difficult to achieve the laminar flow during the operation, due to erosion of the blade's leading edge [7]. Another airfoil developed by the University of Glasgow, for the stall-regulated VAWTs, is the GUVA 10, which is symmetrical, sharp-nosed with 18% thickness. It gives a very similar performance to the NACA 0018 but with a lower stalling AOA [29]. Some early studies suggested that VAWT efficiency can be improved by adopting blades with a slight camber. This is because when the camber is added, the upwind part of the VAWT revolution benefits from improved lift also at smaller AOA, although on the other part (downwind), the performance becomes worse. Therefore too much camber is not recommended. In fact, to produce the highest C_P, the camber should be less than 3% [59]. From a study on airfoil optimization, Claessens [55] developed the DU-06-W200 (Delft- University-2006-WindTurbineApplication-20.0%Thickness). It's a laminar airfoil with 0.8% camber Figure 1.14, which features NLF to reduce the drag. Tests in the wind tunnel showed that it behaves approximately the same as the NACA0018 at the negative AOA. While at positive AOA, the performance is better due to a higher lift curve slope. This leads to a shift of the C_P curve towards the right, see Figure 1.14.

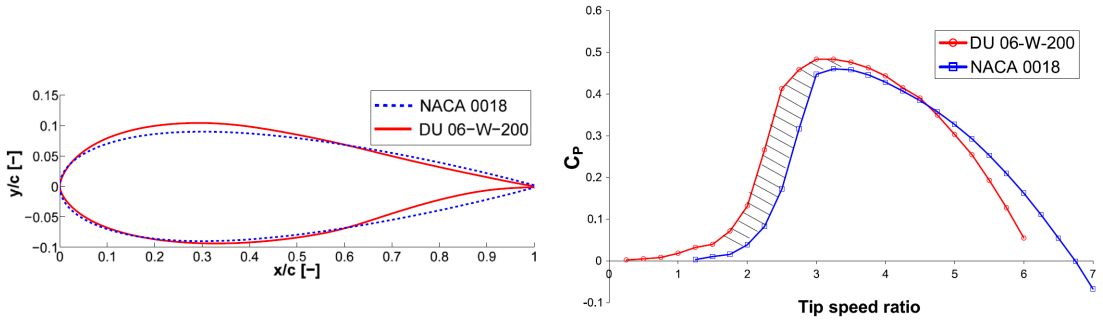

Figure 1.14: Shape and Performance comparison of NACA 0018 and DU 06-W200 Airfoils [55]

- **5- Strut design:**
  The struts connect the blades of the VAWT to its central tower. Clearly, they are always necessary only for the straight-bladed VAWTs. For the curved-bladed they are optional. They are needed to give structural support by resisting the gravitational, inertial, and aerodynamic loads generated by the blades. Apart from these structural merits, their presence introduces a flow disturbance and creates two types of parasitic drag (one from the struts themselves and one from their interface with the blades) [7]. Figure 1.16 shows the comparisons conducted on the SNL 17-m Darrieus, with and without the struts. It was found that the presence of struts reduces significantly the maximum power output [93]. The performance is sensitive to the addition of a support structure, especially at high tip-speed ratios. The drag introduced by the struts can be reduced by applying a strut section that is aerodynamically streamlined. A NACA0021 as strut section and a cylindrical strut cross-section were investigated [9]. The strut losses with NACA0021 were found to be much lower. It was indicated that streamlined struts should be used especially for low-solidity turbines. The drag generated ad interface between the blade and strut is related to the formation of the "horseshoe vortex" and can be alleviated by using a fairing. In fact, the fairing merges the boundary layers of the struts and blades smoothly, reducing the flow separation. Another important factor in the design of struts is their orientation and arrangement. In fact, the struts are usually horizontal and connected to the blades with a T-joint configuration. In some cases, they may be inclined. The latter configuration can be adopted to reduce the tower height and/or to obtain a lower center of gravity. From the aerodynamic point of view, it's not recommended to have acute angles at the joint point, since the interface drag is lower with the T-joint case. From a structural standpoint, it's preferred to have struts connected perpendicularly to the blade since in this configuration the normal loads of the blades will be transferred to the struts in pure compression or tension (without imparting bending moments [40]). The horizontal struts can support the blades in different ways, as illustrated in Figure 1.15. The cantilever supported is preferred for minimizing the parasitic losses. However, for a standard H-shaped VAWT, the use of two struts is recommended to reduce the bending moment [48, 8].

- **6- Height-to-Radius ratio and Blade Aspect Ratio:**
  This ratio is one of the most important parameters of the VAWTs design, especially for the straight-blades. In fact, fixing the swept area, initially, it might seem preferable to use low H/R ratio to maximize the chordal Reynolds number. Indeed, increasing the radius allows the blade chord to be larger [24]. Since that H/R is equal to the product of the chord to

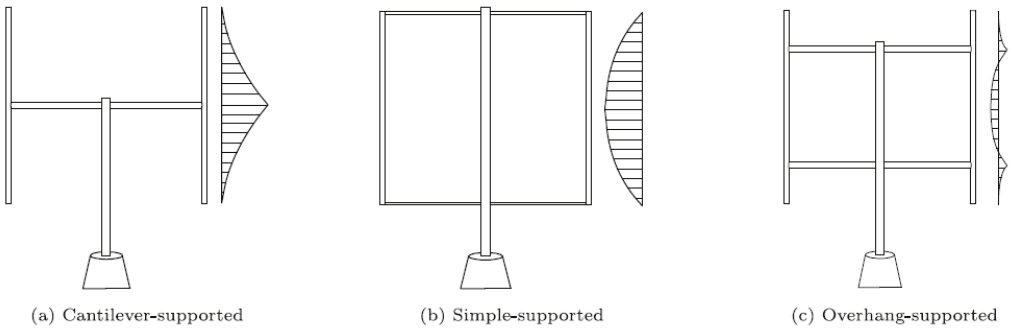

(a) Cantilever-supported (b) Simple-supported (c) Overhang-supported

Figure 1.15: Three Strut Arrangements with Bending Moment Diagrams[42]

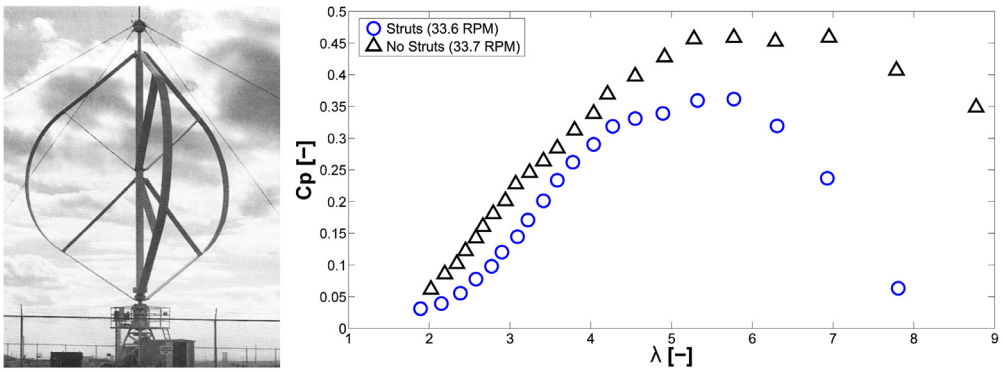

Figure 1.16: The Impact of Struts on the Performance of the SNL 17-m Turbine[93]

radius ratio and the blades-aspect-ratio (H/R=H/c x c/R). So increasing the chord means the blades will have a low aspect ratio which will inevitably result in greater losses at the blade tip. A study conducted by Zanforlin et al. [81] identified that the Reynolds number effects are less dominant than the tip loss effects. According to various studies, it is advised to avoid using small blade aspect ratios, and to achieve respectable performance it must surpass 7,5. However, it was identified that the peak efficiency increase with H/R, but the blade failure probability also increase with H/R.

- **7- Chord to radius ratio (Curvature Index):**
  The VAWT's cycloidal motion means that its blades are subject to a curvilinear flow. In fact, a symmetrical blade immersed in a curvilinear flow is similar to a cambered one at incidence in rectilinear flow 1.17. Numerical studies conducted by Rainbird et al. [76] found the following: - As the c/R is increased, the virtual incidence increases. - Fixing c/R, a slight increase in the virtual incidence with increasing the tip speed ratio.

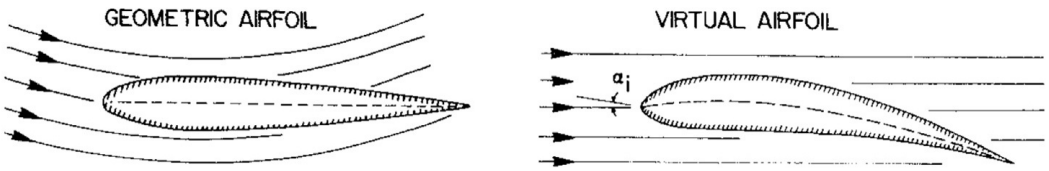

Figure 1.17: Flow Curvature Influence on a VAWT Airfoil[62]

- **8- Blade pitch angle:**
  The blade pitch angle is defined as the angle between the blade chord and the line tangent to the pitch circle at the blade-strut-connection point (i.e. c/4 or c/2). The neutral blade pitch angle is when the tangent line and the blade chord are colinear. This angle can be positive "toe-in" or negative "toe-out" as shown in Figure 1.18. It was identified from experimental and numerical studies that a small negative pitch angle (β=-2°) improves the performance (about 10% [56, 46]), because implementing a negative pitch angle reduces the excessive angle of attack on the upwind side where the turbine produces more power, and delay the occurrence of dynamic stall. Instead, a positive β forces stall to occur earlier.

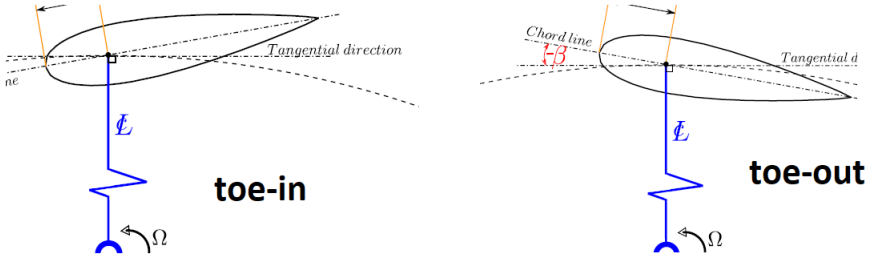

Figure 1.18: Types of fixed blade pitch angles

Chapter 2

Applied Numerical Methods

2.1 Introduction

Over the past three decades, the size of commercial wind turbines has significantly increased. Initially, in the early 1980s, they were about 50 kW in capacity, but now they have evolved into multi-megawatt (MW) turbines with rotor diameters exceeding 200 m. Despite predictions of reaching an optimal mid-range size and periods of stagnation, commercial wind turbines have consistently grown in size. Over a span of ten years, the installed generator power has approximately increased 5 times. The primary objective behind this growth is to decrease the cost of energy production. As long as increasing the turbine size leads to cost reduction, it is expected that wind turbines will continue to increase in size for many years to come. However, there are certain factors that could halt this trend, such as challenges associated with manufacturing large blades, as well as handling the weight-induced stress that becomes more and more important when the turbine's diameter is augmented and its rotation speed is reduced.
Alternatively, a more advanced approach to harnessing more wind energy is to enhance aerodynamic efficiency through optimization techniques in the initial design. In the development of new wind turbines, optimizing the energy output and minimizing production costs have become crucial concerns, necessitating aerodynamic and structural optimization. Consequently, reducing the cost of energy per unit produced by a wind turbine is a significant objective in modern wind turbine research. However, since the target is to reduce the LCOE, an aerodynamic optimal rotor may not always be the most cost-effective.

Having accurate and efficient models to predict wind turbine performance is crucial in obtaining reliable optimum designs for wind turbine rotors. This is because optimization techniques rely on these models, which include both aerodynamic and structural components. Consequently, the outcomes of an optimization procedure are significantly influenced by the mathematical and numerical models employed. Therefore, the quality and effectiveness of these models play a vital role in ensuring the reliability of the final design of wind turbine rotors.

Researchers have shown a growing interest in rotor aerodynamics in recent years, driven by the demands of the wind energy industry. Notably, there have been remarkable advancements in the development of numerical simulation tools for optimizing rotor performance, modeling wind turbine wakes, and analyzing the aerodynamics of wind farms. These advancements, facilitated by modern computational fluid dynamics (CFD) tools and computational resources, have played a vital role in significantly advancing the state-of-the-art in rotor aerodynamics. Through CFD, engineers have been able to formulate and validate engineering principles for a wide range of previously unsolved problems. Experimental data and CFD computations using innovative tech-

niques are now used to derive airfoil data for blade design. However, the classical method for assessing wind turbine aerodynamics, known as the Blade Element Method (BEM) technique, which is known for its speed and reliability in aerodynamic optimization, remains in use today but with various additional corrections. This adaptation enables the BEM technique to address a broader range of operational conditions.

The figure below illustrates the various numerical methods used to simulate the aerodynamics of wind turbines. With the shift from employing inviscid models to adopting more advanced methodologies, the fidelity of the simulation improves considerably. However, this improvement comes at the expense of a substantial increase in computational requirements.

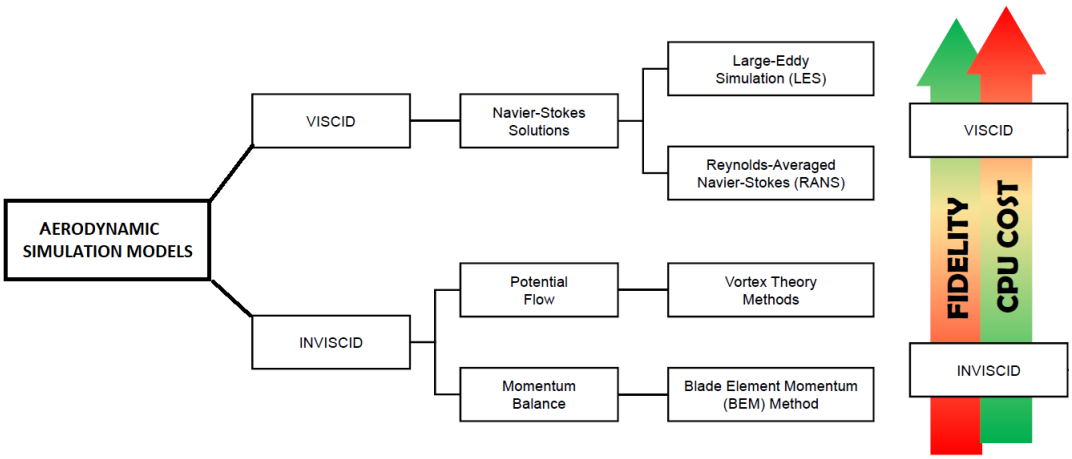

Figure 2.1: Numerical Approaches in Investigating Aerodynamics

In this section, the aim is to provide a brief overview of these diverse aerodynamic models that have been employed to optimize the design of wind turbines. Subsequently, our attention will shift towards emphasizing the CFD model adopted specifically within the context of this thesis.

2.2 Inviscid Models

2.2.1 Overview on BEM Method

The Blade Element Momentum theory (BEM) holds a prominent position as a widely adopted industry standard methodology, extending its influence to the present day. It distinguishes itself through its notable accuracy when thoughtfully configured, its favorable computational efficiency, and its inherent adaptability and customizability. However, it is essential to recognize the inherent limitations of this approach, particularly in terms of its ability to provide a comprehensive depiction of the flow field and its indirect treatment of airfoil aerodynamics. Instead of directly solving these aerodynamic phenomena, BEM relies on the utilization of assembled parameters to approximate and represent them. Specifically, the turbine is assimilated as an actuator disk, effectively extracting energy from the fluid flow.

The BEM theory is a combination of the momentum theory, originally developed by Glauert for propellers and by Betz for windmills, and the blade element theory. The momentum theory involves analyzing a control volume to conserve momentum, while the blade element theory focuses on analyzing the forces acting on a blade section based on the incoming flow and blade

geometry. In the BEM theory, the forces calculated using the blade element method are linked to the change in momentum as predicted by the momentum theory. This connection allows for calculations of the performance characteristics for each annular section of the rotor. In fact, in the BEM method, the rotor is divided into streamtubes, which can be visualized as annular sections with an infinitesimally small thickness denoted by dr, see Figure 2.2 for HAWT applications.

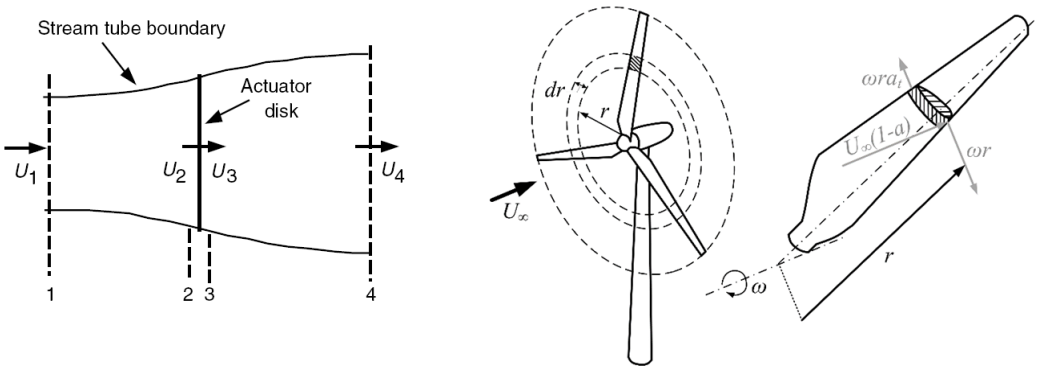

Figure 2.2: Illustration of the Blade Element Method (BEM) Approach

The conservation of momentum equation in the streamwise direction is employed to model the thrust of the rotor. In this approach, the rotor's thrust is represented as a deceleration of the flow, resulting in the expansion of the streamtube.

$$\frac{dT}{dr} = \rho U^2 \pi r 4a(1-a) \tag{2.1}$$

The exchanged torque is obtained by the conservation of angular momentum:

$$\frac{dQ}{dr} = U\Omega r^3 \pi 4a'(1-a) \tag{2.2}$$

Where a and a' are the backbone of the BEM theory. They are defined as follows:

$$a = \frac{1}{4sin^2\phi/(\sigma C_n)+1} \qquad a' = \frac{1}{4sin\phi cos\phi/(\sigma C_t)-1} \tag{2.3}$$

where ϕ is the flow angle, i.e. the angle between the local relative speed and the rotor plane. σ=N$_n$ c/2πr is the local solidity.

In the BEM method, the entirety of the equation system, known for its non-linear and implicit nature, necessitates a solution process that can either involve the implementation of a non-linear technique to solve the complete set of equations or the adoption of a simple iterative updating method. The latter choice proves to be the most convenient for various reasons, and the procedure for obtaining a solution may be outlined as follows:

1. Dividing the rotor blade into a series of span-wise segments, typically ranging from 20 to 30 elements, and initiate an iterative process for each individual segment.

2. Make an initial estimation (Guess) for the variables a and a'. This estimation can be derived either from the values obtained in the preceding element or, for instance, by assigning a value of 1/3 to a and 0 to a'.

3. Calculate the flow angle using the given expression: $\phi = tan^{-1}\left(\frac{1-a}{\lambda x(1+a')}\right)$ where $\lambda = \frac{\Omega R}{V_\infty}$ is the Tip Speed Ratio and $x = r/R$.

4. Compute the angle of attack ($\alpha = \phi - \gamma$). Utilize this information to derive and determine the airfoil characteristics $C_l = C_l(\alpha)$ and $C_d = C_d(\alpha)$.

5. Compute the normal and tangential force coefficients C_n and C_t as follows: $C_n = C_l cos\phi + C_d sin\phi$ and $C_t = C_l sin\phi - C_d cos\phi$.

6. Update a and a′, then continue the iterative process until convergence.

For each element around 10 iterations should be sufficient in order to achieve acceptably converged values if the turbine is running in its usual wind turbine state. However, at off-design conditions, convergence may be problematic and this represents one of the BEM limitations. BEM theory reformulated according to the so-called Double Multiple stream tube model presented by [69] can applied to VAWTs, as done by [82], see figure2.3, where some modifications were introduced to improve the local load prediction; the method however still requires having accurate database to reach accurate prediction.

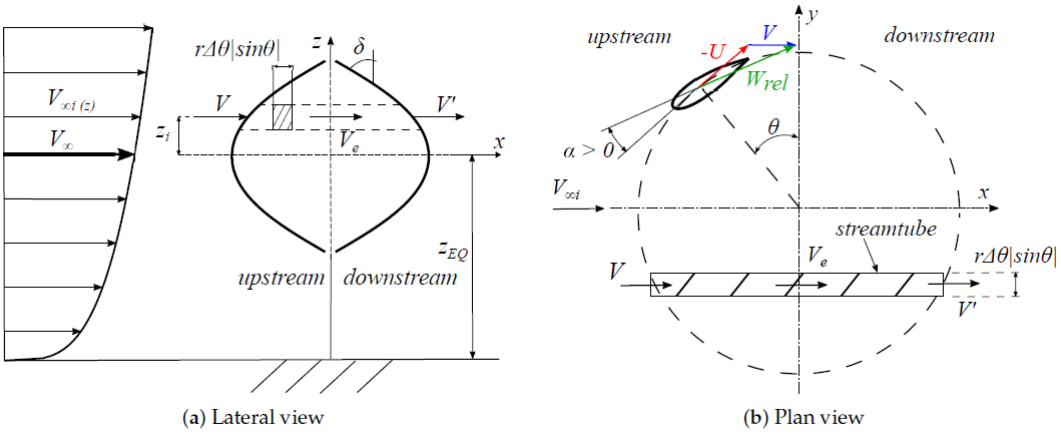

Figure 2.3: Schematic of the DMST model reference frame[82]

2.2.2 Overview on Vortex Method

The utilization of vortex methods has been extensively explored in aircraft and helicopter research to model the wake and air loads in different operational conditions. Currently, these methods are becoming an attractive tools for the analysis and design of wind turbine rotors. This approach allows for a significant interaction between the design method and blade geometry, resulting in a more comprehensive aerodynamic description than BEM methods. In fact, in comparison to the BEM method, it offers greater accuracy in capturing physical solutions for attached flow conditions by incorporating boundary layer corrections. Moreover, the vortex method remains valid across a broader range of turbine operating conditions.

Vortex methods propose two approaches to model the trailing and shed vortices produced by wind turbine blades: utilizing either freely or restrictedly moving vortex. The prescribed

wake demands less computational effort compared to the free wake approach, but it necessitates experimental data to ensure its validity across a wide range of operating conditions. In opposition, the free wake model stands out as the most computationally demanding. However, this latter offers superior accuracy in predicting wake geometry and loads compared to the prescribed wake model, primarily due to its less restrictive assumptions.

The Vortex flow theory is based on the assumption of an incompressible flow ($\nabla \cdot V = 0$) and an irrotational flow (∇ x V = 0) at all points, except for the vortex's origin, where the velocity is infinite. Furthermore, in vortex theory, the vortical structure of the wake can be represented through the utilization of either vortex filaments or vortex particles. A vortex filament is a model that involves concentrated vortices aligned along an axis, with a singularity located at the center. In addition, the Biot-Savart law allows the calculation of the velocity induced. However, the Biot-Savart law exhibits a singularity when the point at which the induced velocity is being evaluated coincides with the axis of the vortex filament. Moreover, when the evaluation point is in close proximity to the vortex filament, an unphysical and excessively large induced velocity occurs at that specific location. To deal with this matter, one potential solution is to utilize a viscous vortex model with a finite core size, which involves incorporating a multiplication factor to mitigate the singularity (cut-off radius r_c). Therefore, the Biot-Savart low becomes:

$$Vind = -\frac{1}{4\pi} \int \Gamma \frac{r \times \delta l}{r^3 + r_c^2} \tag{2.4}$$

where Γ represents the strength of the vortex filament.

Currently, in the field of wind energy, one notable and noteworthy application of the vortex model is the QBLADE software. QBLADE is specifically built upon the Lifting Line Free Vortex Wake (LLFVW) concept. Similar to BEM method, the LLFVW model also relies on the utilization of two-dimensional sectional airfoil polar data to compute the blade forces. The main distinction lies in the explicit resolution of the rotor wake, which is shed from the blades. This represents a significant advancement compared to the conventional approaches employed in the BEM Method, which often require the inclusion of numerous empirical corrections within the simulated system. By explicitly modeling the dynamics of the wake, the need for correction models is avoided, leading to more physically accurate results. Simulation results demonstrate notable improvements, particularly in scenarios where the assumptions of the BEM Method are violated. These scenarios encompass unsteady operations, significant blade deformations, and high tip speed ratios approaching turbulent wake states. These conditions are increasingly prevalent as the industry trend leans towards larger rotor sizes and offshore floating wind turbines.

In this framework, the rotor is modeled using a lifting line situated at the quarter chord position of the 2D airfoil sections. Additionally, each blade panel is represented by a vortex ring comprised of four straight vortex filaments. The determination of the circulation of the bound vortex lines, which constitute the lifting line, relies on the relative inflow velocity and the lift and drag coefficients acquired from tabulated airfoil data. The calculation of the sectional circulation follows the principles of the Kutta-Joukowski theorem: $\delta F_L(\alpha) = \rho V_{rel} \times \delta\Gamma$, where ∂F_L is the sectional lift force and ρ is the fluid density. The relative velocity V_{rel} is determined by combining the free stream velocity, blade motion, and induced velocity. The induced velocity is computed using the Biot-Savart equation, which considers the contributions from all vortex elements on the blade and in the wake.

In each time step (see figure 2.5), the circulation distribution along the blade is determined, employing an iterative process that ensures the alignment of predicted forces based on the Kutta-Joukowski theorem and the blade element theorem. During the iteration, updates are made solely to the bound vorticity distribution, while the influence of wake elements on the blade is evaluated

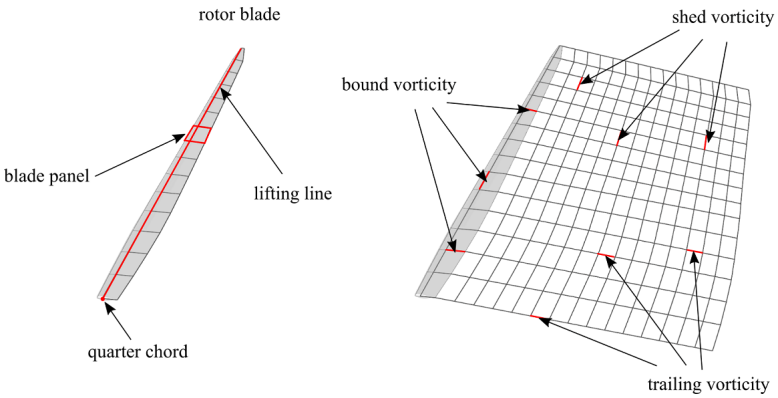

Figure 2.4: Key Elements of Blade and Wake Models in the LLFVW Algorithm[4]

only once. Once convergence is achieved, the rotor rotation is advanced for a single time step. The free wake vortex elements are convected based on the local inflow and local induced velocity. Following the wake convection step, new vortex elements are generated between the trailing edge of each blade panel and the last row of wake vortices that have been carried away from the trailing edge.

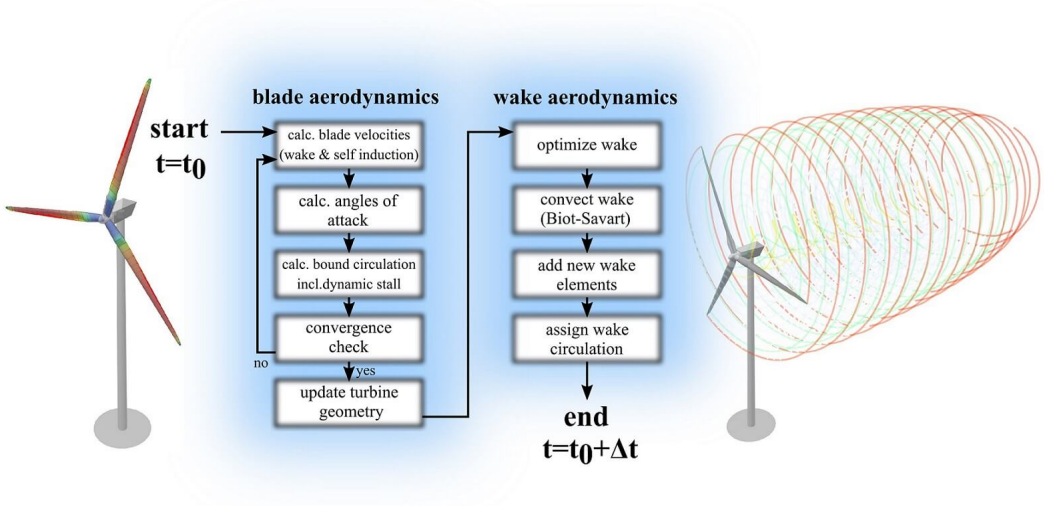

Figure 2.5: Aerodynamic calculations for a single time-step in QBlade[4]

As a final step, the circulation is calculated and assigned to the newly released vortex lines by adhering to the Kutta condition.

$$\Gamma_{trail} = \frac{\partial \Gamma_{bound}}{\partial x}\Delta x, \qquad \Gamma_{shed} = \frac{\partial \Gamma_{bound}}{\partial t}\Delta t. \tag{2.5}$$

The shed and trailing vortices are interconnected through shared vortex nodes. During the free wake convection step, the evolution of the wake is evaluated by advancing the positions of these vortex nodes over time. Each newly created vortex node is connected to at least one shed

and one trailing vortex filament, resulting in approximately half the number of vortex nodes compared to the total number of vortex filaments. As a result, the Biot-Savart equation needs to be evaluated a reduced number of times, which reduces the computational cost by a factor of 2 due to the interconnectivity of the wake lattice. To optimize the wake structure and reduce the number of free vortices within the wake, a method has been implemented to remove individual vortices from the wake mesh by detaching vortex filaments from their corresponding nodes. During each step of the simulation, a check is performed to eliminate isolated vortex nodes that are not attached to any vortex filament. The removal of vortices from the wake lattice reduces the influence of interconnections as more vortices are removed.

The vortex model can also be considered as potential tool for VAWTs simulations to predict the load at reduced CPU cost. However proper sub-models and corrections are still needed, see e.g [60].

Inviscid models are easily applicable to the HAWTs. Yet, they have several disadvantages, such as neglecting the effects of viscosity, which lead to inaccurate predictions of flow separation, boundary layer effects, and wake dynamics near the blades. They oversimplify the flow physics, assuming idealized conditions and resulting in significant discrepancies with real-world behavior. They fail to capture the complex wake dynamics behind wind turbines, which can affect power production and turbine interactions. Moreover, these models are limited in simulating wind turbines under different operating conditions. For accurate simulations, more advanced computational fluid dynamics models are necessary, considering the full Navier-Stokes equations, and turbulence models, and accounting for viscous effects, wake dynamics, and a wide range of operating conditions. The vortex

2.3 Viscous model: CFD

Computational Fluid Dynamics (CFD) comprises a set of methodologies that enable the numerical simulation of fluid motion, heat exchange, and related phenomena, including combustion and chemical reactions, by utilizing computer-based techniques. This technique finds extensive application in engineering, as employing CFD software to address fluid-dynamic problems offers numerous advantages, such as:

- CFD simulations provide detailed insights into fluid behavior, allowing engineers to accurately analyze complex flow patterns, turbulence, and fluid-structure interactions.
- Cost and time efficiency: By employing CFD, engineers can conduct virtual experiments and optimize designs without the need for physical prototypes.
- Design Optimization: CFD software enables iterative design improvements, allowing engineers to explore numerous design variations and optimize performance parameters for better efficiency, reliability, and safety.
- CFD simulations generate visual representations, such as velocity vectors and streamline plots, facilitating understanding flow characteristics.
- CFD models enable the prediction of key performance metrics, such as lift and drag forces, momentum, pressure distributions...etc, assisting in the evaluation and comparison of design alternatives.

2.3.1 Structure of CFD Code

Most of the commercial codes currently used in engineering, such as Star CCM+, which is used in this thesis work, have an interface that allows the user to easily set up the various calculation and analysis options. The first question that comes to mind is: how is a CFD code structured?

A CFD code generally consists of three main parts, which correspond to the three phases of analysis of the problem to be solved, in order are:

- **Pre-processing:** In this phase, the physical problem is defined and then implemented as a mathematical model. The calculation domain is divided into several elements to create a calculation grid (mesh) in which the properties and boundary conditions are set. As the overall accuracy of the simulation is heavily dependent on the quality and density of the mesh, it is important to create a grid that is not uniform over the whole domain but fine where the gradients of the variable quantities are greater and coarse in the region characterized by slight changes in flow conditions.
- **Solver:** The numerical resolution algorithm represents the core of a CFD code. The following approach is used by all major CFD solvers:
  - Modeling the unknowns of the problem using simple analytic functions,
  - Discretization of governing equations by substituting previous functions,
  - Solving the algebraic system of equations.
- **Post-processing:** At this stage, the obtained numerical solution is analyzed. The output of the solver is a vector that allows obtaining the value of the quantities of interest (pressure, velocity, and so on...) in the considered domain. This data must be collected, and processed in the most suitable way for analysis, to produce a physical representation of the solution.

2.3.2 Navier–Stokes equations

The fundamental governing equations for the description of fluid flow motion, known as the Navier-Stokes equations, represent the formulation of conservation principles within a given volume. These equations can be examined through two distinct approaches:

- **Eulerian Approach:** The region being studied is referred to as a control volume since it remains fixed in space while the fluid molecules contained within it undergo changes over time. The control volume, as a standalone system, is considered open, enabling the exchange of both mass and energy with the surrounding fluid
- **Lagrangian Approach:** The region being investigated is known as a material volume as it moves along with the fluid, ensuring that the fluid molecules within it remains constant. The system consisting solely of the material volume is considered closed, as it does not exchange mass with the surrounding fluid but only exchanges energy.

The volume under study implies the verification of three fundamental laws as a general requirement. These laws can be outlined as follows:

- Conservation of mass:
$$m = cost \rightarrow \frac{dm}{dt} = 0 \tag{2.6}$$
- Newton's second law:
$$\vec{F} = m\vec{a} = \frac{dp}{dt} \tag{2.7}$$
- First principle of thermodynamics (conservation of energy)
$$\frac{dE}{dt} = \frac{dQ}{dt} + \frac{dL}{dt} \tag{2.8}$$

Wind turbines typically operate at tip speeds below 100 m/s, resulting in incompressible flow around them. Therefore, in this section, we will solely focus on presenting the equations associated with incompressible flow

- **Conservation of mass:** The mass of a fluid can be mathematically described as a function of its density and the volume it occupies:
$$m = \int_V \rho \, dV \tag{2.9}$$
Considering an open system, applying the Reynolds transport theorem: "The variation of a generic extensive quantity relative to the volume of a mass, corresponds to the variation of the quantity itself in the control volume CV plus the flux of the quantity through the surface of the control volume". Then the law of conservation of the mass becomes:
$$\frac{dm}{dt} = \int_V \frac{\partial \rho}{\partial t} dV + \int_S \rho U \cdot n dS \tag{2.10}$$
where the first addend is the mass variation in the control volume considered, while the second is the mass flow across the CV surface, and n is the normal vector at each point of

the surface. If we then apply Gauss's divergence theorem, in order to convert the surface integral into a volume integral, we obtain:

$$\int_V \frac{\partial \rho}{\partial t} dV + \int_V \nabla \cdot (\rho U) dV = 0 \tag{2.11}$$

which in differential form is written as:

$$\frac{\partial \rho}{\partial t} + \nabla \cdot (\rho U) = 0 \quad \rightarrow \quad \frac{\partial \rho}{\partial t} + U \nabla \cdot \rho + \rho \nabla \cdot U = 0 \tag{2.12}$$

For incompressible flow, since ρ is constant, ***the continuity equation*** reduces to:

$$\nabla \cdot U = 0 \tag{2.13}$$

- **Conservation of Momentum:** The principle of momentum conservation originates from Newton's second law of motion. By defining 'm' as the mass of the particle, we can express:

$$\frac{dp}{dt} = \frac{d(mU)}{dt} = \vec{F} \tag{2.14}$$

$\vec{F}$ is the sum of the forces applied to the particle, i.e. both volume and surface forces:

$$\vec{F} = \int_V \rho f \; dV + \int_S TS \cdot n \; dS \tag{2.15}$$

Where $\boldsymbol{f}$ indicates the entity of volume forces per unit mass. $\boldsymbol{TS}$ is the stress tensor, acting on the surface, defined as follows:

$$TS = -p + \tau \tag{2.16}$$

$\boldsymbol{p}$ indicates the hydro-static component of the stress tensor, which corresponds to the pressure $\boldsymbol{p=pI}$, where $\boldsymbol{I}$ is the identity matrix, τ, on the other hand, is the viscous stress tensor defined as follows:

$$\tau = \mu[\nabla(U) + \nabla^T(U)] \tag{2.17}$$

Therefore, we obtain:

$$\frac{dp}{dt} = \int_V \rho f \; dV + \int_S TS \cdot n \; dS \tag{2.18}$$

Applying the Reynolds transport theorem to the left-hand term:

$$\frac{dp}{dt} = \int_V \frac{\partial}{\partial t}(\rho U) \; dV + \int_S \rho U (U \cdot n) \; dS \tag{2.19}$$

By employing the divergence theorem:

$$\int_V \frac{\partial}{\partial t}(\rho U) \; dV + \int_V \nabla(\rho U U) \; dV = \int_V \rho f \; dV + \int_V \nabla \cdot TS \; dV \tag{2.20}$$

Expressing this equation in its differential form and substituting the components of $\boldsymbol{TS}$, we can rewrite it as follows:

$$\frac{\partial}{\partial t}(\rho U) + \nabla(\rho U U) = \nabla \cdot \tau - \nabla \cdot (p) + \rho f \tag{2.21}$$

Rewriting in an extended version:

$$\begin{cases} \rho\frac{Du}{Dt} = \rho f_x - \frac{\partial p}{\partial x} + \mu(\frac{\partial^2 u}{\partial x^2} + \frac{\partial^2 u}{\partial y^2} + \frac{\partial^2 u}{\partial z^2}) \\ \rho\frac{Dv}{Dt} = \rho f_y - \frac{\partial p}{\partial y} + \mu(\frac{\partial^2 v}{\partial x^2} + \frac{\partial^2 v}{\partial y^2} + \frac{\partial^2 v}{\partial z^2}) \\ \rho\frac{Dw}{Dt} = \rho f_z - \frac{\partial p}{\partial z} + \mu(\frac{\partial^2 w}{\partial x^2} + \frac{\partial^2 w}{\partial y^2} + \frac{\partial^2 w}{\partial z^2}) \end{cases} \tag{2.22}$$

Considering the previously mentioned continuity equation as well. The derived equations correspond to the well-known Navier-Stokes equations for incompressible flow. They are second-order and non-linear differential equations with four unknowns.

- **Conservation of kinetic energy:** By considering the simplified equation governing the conservation of momentum:

$$\rho\frac{DU}{Dt} = \nabla \cdot \tau \tag{2.23}$$

Performing scalar multiplication of both sides of the equation by U:

$$U \cdot \rho\frac{DU}{Dt} = U \cdot (\nabla \cdot \tau) \tag{2.24}$$

The **LHS** *left hand side* term can be demonstrated to be equal to:

$$U \cdot \rho\frac{DU}{Dt} = \rho\frac{De_{kin}}{Dt} \tag{2.25}$$

While the **RHS** *right hand side* term can be demonstrated to be equal to:

$$U \cdot (\nabla \cdot \tau) = \nabla \cdot (\tau \cdot U) - 2\mu S : S \tag{2.26}$$

Where $S = \frac{\mu[\nabla(U)+\nabla(U)^T]}{2}$, called *strain rate tensor*. Therefore, we obtain:

$$\rho\frac{De_{kin}}{Dt} = \nabla \cdot (\tau \cdot U) - 2\mu S : S \tag{2.27}$$

$2\mu S : S$ represents the *dissipation* term, i.e. it transforms the kinetic energy into internal energy. While $\tau \cdot U$ is the contribution due to the forces acting on the surface of the CV.

- **Conservation of total energy:** It's well-known that:

$$\frac{DE_t}{Dt} = \dot{Q} + \dot{W} \tag{2.28}$$

Where $\dot{Q}$ and $\dot{W}$ are the thermal and the mechanical power respectively. Defining $E_t = me_t$, with $e_t = e_{kin} + e_{int} + e_{chim} + e_{pot}$, which refers to the total energy per mass unit. By neglecting potential energy and energy associated with chemical or nuclear reactions, the equation can be expressed using the transport theorem as follows:

$$\int_V \frac{\partial(\rho e_t)}{\partial t}\, dV + \int_S \rho e_t U \cdot \mathbf{n} dS = \int_S k\nabla T \cdot \mathbf{n} dS + \int_S \tau \cdot U \cdot \mathbf{n} dS \tag{2.29}$$

Where k is the thermal conductivity and **T** is the temperature. With a few intermediate steps, we can derive the following:

$$\rho\frac{De_t}{Dt} = \rho\frac{De_{kin}}{Dt} + \rho\frac{De_{int}}{Dt} = \nabla \cdot (\tau \cdot U) + \nabla \cdot (k\nabla T) \tag{2.30}$$

By substituting the kinetic energy equation and incorporating the term $p\nabla \cdot U$, which is present only in a compressible flow, we can derive the conservation of internal energy. This can be expressed as follows:

$$\rho\frac{De_{int}}{Dt} = \nabla \cdot (k\nabla T) + 2\mu S : S - p\nabla \cdot U \tag{2.31}$$

2.3.3 Turbulence modelling

Turbulence is inherently a stochastic phenomenon capable of efficiently transporting and diffusing momentum through velocity and pressure fluctuations. A turbulent flow is characterized by spatial and temporal variations, even though in certain instances, it may maintain constant average values over time. The Reynolds number, which represents the ratio of inertial forces to viscous forces, plays a crucial role in characterizing the nature of a flow. This parameter becomes particularly significant as it determines the type of flow behavior. At sufficiently high Reynolds numbers, viscous effects become negligible, and energy is transferred through an inviscid process that is independent of viscosity. Large eddies are inherently unstable and consequently fragment into smaller eddies, progressively transferring energy to increasingly smaller scales. These smaller eddies eventually dissipate turbulent kinetic energy as a result of viscosity. This phenomenon is commonly referred to as the "**Energy cascade**". This concept of the energy cascade was first introduced by *Rischardson* in 1922. Taken up by *Kolmogorov* in 1941, based on some simple similarity assumptions: *Kolmogorov microscales theory.* This theory mainly answers to:
-What is the scale of the smallest eddies that are accountable for the dissipation of energy?
-As the characteristic size decreases, how do the characteristic velocity and time scales alter?

The assumptions of Kolmogorov's theory are:
1- Local isotropy: For sufficiently high Reynolds numbers, it is observed that only the small scales of a turbulent flow exhibit static isotropy, meaning they are independent of translations, rotations, and reflections. Conversely, the large scales of the flow remain anisotropic. To distinguish between the large anisotropic and small isotropic eddies, a reference length is introduced to serve as a demarcation point.: $l_r = \frac{L}{6}$.
2- First similarity hypothesis: For each turbulent flow (High Reynolds numbers), small-scale statistics have a universal form uniquely determined by ν and ε (the dynamic viscosity and energy dissipation term). An expression of the characteristic quantities of small scales can be derived employing dimensional analysis:
- *Characteristic length*: $\eta = \frac{\nu^{3/4}}{\varepsilon^{1/4}}$
- *Characteristic time*: $t_\eta = (\frac{\nu}{\varepsilon})^{1/2}$
- *Characteristic velocity*: $u_\eta = (\nu\varepsilon)^{1/4}$.

By utilizing these terms in calculations, the Reynolds number for small scales can be determined to be on the order of unity, indicating that the magnitude of viscous forces is approximately equal to that of inertial forces. Moreover, it can be inferred that the disparity between the two scales is primarily dependent on the Reynolds number, following a certain relationship:

$$\frac{L}{\eta} = Re^{3/4} \quad , \quad \frac{U}{u_\eta} = Re^{1/4} \quad , \quad \frac{t}{t_\eta} = Re^{1/2}$$

3- Second similarity hypothesis: For high Reynolds numbers, the statistical characteristics of the flux at intermediate scales "r" within the interval $L \gg r \gg \eta$ (where L is the integral scale and η is the Kolmogorov microscale) exhibit a universal form that solely relies on the energy dissipation rate ε and is independent of the viscosity ν. Thus, the influence of viscosity becomes negligible in this range. This interval is referred to as the "inertial sub-range" as it represents the region where energy is transferred from large eddies to small dissipating eddies, signifying a transitional flow of energy.

In order to numerically simulate a turbulent flow, it is essential to consider the inherent characteristics of the real velocity field, which is three-dimensional, random, and unsteady. Additionally, turbulent flows exhibit a wide range of temporal and spatial scales. As a result, discretization of the convective term becomes necessary. To achieve this, one of the following techniques is employed, they are distinguished based on the variables being solved.

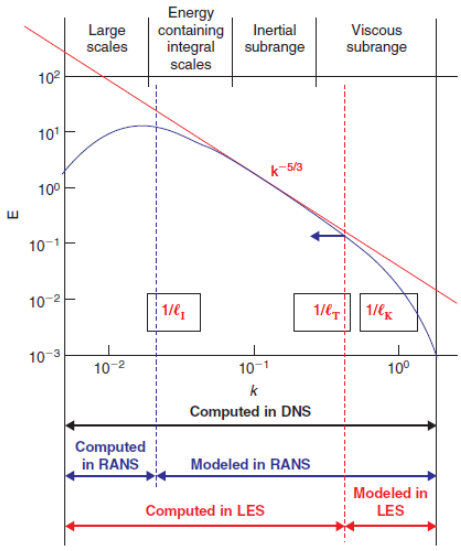

Figure 2.6: Schematic Illustration of Turbulence Modeling Scales

- **DNS** (*Direct numerical simulation*): In this approach, we simulate all scales, both spatial and temporal, and precisely we consider the variables U(x, t) and p(x, t). This method is known for its high accuracy and comprehensiveness. However, its applicability is limited to certain Reynolds number values and relatively simple geometries. Moreover, the computational demands of this approach are directly proportional to the Reynolds number, and this proportionality can be shown to be approximately cubic. As a result, numerical simulations become excessively onerous for any existing computer.

- **LES** (*Large eddies simulation*): The variables, in this approach, become $\overline{U}(x,t)$ e $\overline{p}(x,t)$, which indicate the filtered (not the averaged) magnitudes; The large scales are simulated while the small scales are modeled. The decomposition used in this technique is as follows: $U(x,t) = \overline{U}(x,t) + u'(x,t)$, where $\overline{U}(x,t)$ depends on a parameter that chooses which scales should be simulated and which ones should be modeled, $u'(x,t)$ instead is the residual component. The computational cost is however high and currently, it's used mostly only in academic research.

- **RANS** (*Reynolds averaged Navier-Stokes equations*): The variables involved are $\langle U \rangle$, $\langle p \rangle$, ν_T, $\langle u'u' \rangle$, where the calculation of the last variable, the Reynolds stress tensor, is the most expensive. This technique is of significant practical interest due to its remarkably low computational cost. Furthermore, the thesis work focuses on investigating the mean flow behavior and capturing averaged quantities rather than resolving micro-scale turbulence structures. Therefore, this is the employed technique. Later on, we will delve into the origins of this term, its modeling, and the specific conditions under which it applies.

RANS modeling, introduced by Reynolds in 1894, uses the following decomposition of the velocity field:

$$U(x,t) = \langle U(x,t)\rangle + u'(x,t),$$

where $\langle U(x,t)\rangle$ is the averaged value of U over a certain period of time, which is small enough in relation to the phenomena to be tracked but high enough in comparison to the turbulence disturbances. $u'(x,t)$, on the other hand, represents the fluctuation of U.

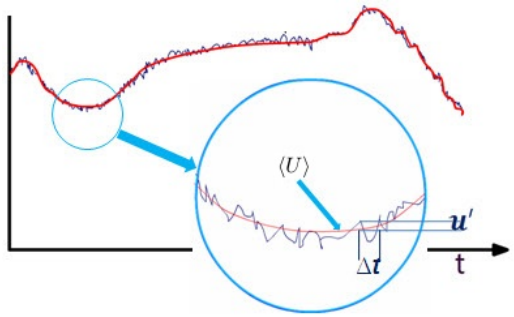

Figure 2.7: Schematic illustration of RANS decomposition

By revisiting the Navier-Stokes equations and employing the Reynolds decomposition, we can establish the fundamental framework of RANS modeling as follows:

$$\begin{cases} \nabla.\langle U\rangle = 0 \\ \rho\frac{\overline{D}\langle U\rangle}{\overline{D}t} = \nabla.[\mu(\nabla\langle U\rangle + \nabla\langle U\rangle^T) - \langle p\rangle I - \rho\langle u'u'\rangle] \\ B.C \end{cases} \tag{2.32}$$

where the terms on the right-hand side of the momentum conservation equation are described as follows:

- $\mu(\nabla\langle U\rangle + \nabla\langle U\rangle^T)$: represents the viscous stresses that transport the momentum to the molecular scales.
- $\langle p\rangle I$: the isotropic stress component due to the mean pressure field.
- $\langle u'u'\rangle$:*The Reynolds stress tensor*, responsible for the momentum transfer due to the fluctuations. It is a symmetric tensor, therefore $\langle u'_i u'_j\rangle = \langle u'_j u'_i\rangle$. As a result, it has only six unknowns instead of nine.

The Boussinesq hypothesis: The set of RANS equations that need to be solved consists of four equations: one for continuity and three for momentum conservation. In contrast, there are ten unknowns: six related to the stress tensor, three associated with the average velocity field, and one for the average pressure. To ensure a closed problem, we would require an additional six equations, or alternatively, utilize approximations to describe the stress tensor. One possible approach to address this is by employing the Boussinesq hypothesis, although its applicability may not always be valid.

Before delving into this topic, it is beneficial to introduce the concept of the *turbulent kinetic energy* κ per unit mass of fluctuations, which can be expressed in the following two manners:

$$\kappa = \tfrac{1}{2}tr\langle u'u'\rangle = \tfrac{1}{2}\langle u'\cdot u'\rangle$$

The tensor $\langle u'u' \rangle$ can be decomposed into an isotropic component $\langle u'u' \rangle^I$ and in a deviatoric component $\langle u'u' \rangle^D$.

$$\langle u'u' \rangle^I = \tfrac{1}{3} tr(\langle u'u' \rangle) I = \tfrac{2}{3} \kappa I$$
$$\langle u'u' \rangle^D = \langle u'u' \rangle - \tfrac{2}{3} \kappa I$$

Boussinesq's hypothesis states that the deviatoric component of the Reynolds stress tensor is proportional to the averaged strain rate tensor.

$$\langle u'u' \rangle^D = -2\nu_T \langle S \rangle$$

The proportionality constant is ν_T, called *turbulent viscosity*. Defining $\mu = \rho\nu$ & $\mu_T = \rho\nu_T$, the momentum equation becomes:

$$\rho \frac{\overline{D}\langle U \rangle}{\overline{D}t} = \nabla \cdot [\rho(\nu + \nu_T)(\nabla \langle U \rangle + \nabla \langle U \rangle^T) - (\langle p \rangle + \frac{2}{3}\kappa) I] \tag{2.33}$$

That is:

$$\rho \frac{\overline{D}\langle U \rangle}{\overline{D}t} = \nabla \cdot 2\rho\nu_{eff} \langle S \rangle - \nabla \cdot (\langle p \rangle + \frac{2}{3}\kappa) I \tag{2.34}$$

Where $\nu_{eff} = \nu + \nu_T$ is called *effective dynamic viscosity*, and considers the enhancement of momentum diffusivity caused by fluctuations. As a result, instead of dealing with five unknowns, here we have only one (ν_T). We have nearly resolved the problem; the only remaining step is to determine an appropriate method for defining ν_T, which enables achieving a closed problem. The determination of turbulent viscosity ν_T involves the introduction of a turbulence model, which can be either a two-equation (k-ε & k-ω) or one-equation model (Spalart-Allmaras). This thesis work focuses on two turbulence models, the k-ω SST and Spalart-Allmaras Model. Consequently, our theory illustration will be limited to these two models.

2.3.4 K-omega SST Model

The k-omega SST turbulence model represents an advancement of the original k-omega model, developed by *Menter* in 1993 [61]. This model utilizes two equations to define turbulent viscosity. The SST version offers the advantage of smoothly transitioning from a classical k-ω model near the wall, where it produces accurate results, to a k-ε model further away from the wall. The k-ε model is known for its ability to predict fluid behavior in such regions. Consequently, the k-omega SST model is frequently employed to solve viscous boundary layer scales, thereby enhancing accuracy in scenarios involving adverse pressure gradients and boundary layer separation.

The two equations of the model relate respectively to:

- k, the turbulent kinetic energy:

$$\frac{\partial(\rho\kappa)}{\partial t} + \frac{\partial(\rho v_j \kappa)}{\partial x_j} = P - \beta^* \rho\omega\kappa + \frac{\partial\left[(\mu + \sigma_\kappa \mu_T)\frac{\partial \kappa}{\partial x_j}\right]}{\partial x_j}, \tag{2.35}$$

- ω, specific dissipation of κ, defined as $\omega = \frac{\varepsilon}{\kappa}$:

$$\frac{\partial(\rho\omega)}{\partial t} + \frac{\partial(\rho v_j \omega)}{\partial x_j} = \frac{\gamma}{\nu_T} P - \beta^* \rho\omega^2 + \frac{\partial\left[(\mu + \sigma_\omega \mu_T)\frac{\partial \omega}{\partial x_j}\right]}{\partial x_j} + 2(1 - F_1)\frac{\rho\sigma_{\omega 2}}{\partial x_j}\frac{\partial \kappa}{\partial x_j}\frac{\partial \omega}{\partial x_j} \tag{2.36}$$

  Where $\varepsilon = \frac{d\kappa}{dt}$ is the dissipation of turbulent kinetic energy that transforms kinetic energy into internal energy.

The following definition is used for the turbulent viscosity equation (with $\mu_T = \rho\nu_T$):

$$\mu_T = \frac{\rho a_1 \kappa}{max(a_1\omega, \Omega F_2)}, \tag{2.37}$$

F_1 is the function that combines the k-omega model used in the near-wall region to the k-ε model that is employed in the undisturbed flow zone, away from the wall. It is defined as:

$$F_1 = tanh({arg_1}^4),$$

$$arg_1 = min\left[max\left(\frac{\sqrt{k}}{\beta^*\omega d}, \frac{500\nu}{d^2\omega}\right), \frac{4\rho\sigma_{\omega 2}k}{CD_{k\omega}d^2}\right] \tag{2.38}$$

Where d represents the distance to the nearest wall, while $CD_{k\omega}$ represents the positive part of the partial derivative of turbulent kinetic energy and dissipation:

$$CD_{k\omega} = max\left(2\rho\sigma_{\omega 2}\frac{1}{\omega}\frac{\partial k}{\partial x_j}\frac{\partial \omega}{\partial x_j}, 10^{-20}\right) \tag{2.39}$$

On the other hand, F_2 is the function used in turbulent viscosity:

$$F_2 = tanh({arg_2}^4),$$

$$arg_1 = min\left[max\left(\frac{\sqrt{k}}{\beta^*\omega d}, \frac{500\nu}{d^2\omega}\right)\right]. \tag{2.40}$$

The model constants are:

$$a_1 = 0.31, \beta^* = 0.09, \chi = 0.41$$

The coefficients of the SST model are derived from the set of the functions ϕ_1 for the k-omega model and ϕ_2 for the k-ε model:

$$\phi = F_1\phi_1 + (1 - F_1)\phi_2 \tag{2.41}$$

The remaining constants are divided between the k-omega model and the k-ε model:

$$\sigma_{k1} = 0.85, \sigma_{\omega 1} = 0.5, \beta_1 = 0.075.$$

$$\sigma_{k2} = 1.0, \sigma_{\omega 2} = 0.856, \beta_2 = 0.0828.$$

The wall conditions for energy and dissipation are respectively:

$$k = 0, \quad \omega = 10\frac{6\mu L}{\rho\beta_1(d_1)^2},$$

As mentioned above, d_1 represents the distance to the nearest cell's node.

2.3.5 Spalart-Allmaras Model

The Spalart-Allmaras turbulence model employs a single transport equation to accurately depict turbulent kinematic viscosity. This model has been specially designed to cater to both aerodynamic applications and those involving turbomachinery. Despite the inclusion of multiple parameters and coefficients, the Spalart-Allmaras turbulence model offers computational efficiency compared to two-equation turbulence models. This advantage arises from the fact that

only a single dynamic differential equation needs to be solved. The single dynamic equation in this model describes a kinematic variable known as the Spalart-Allmaras variable $\tilde{v}$.

$$\mu_T = \rho\tilde{v} f_{v1} \tag{2.42}$$

The damping function, f_{v1}, is computed using the following formula:

$$f_{v1} = \frac{\chi^3}{\chi^3 + C_{v1}^3} \qquad \chi = \frac{\rho\hat{v}}{\mu_T} \tag{2.43}$$

The transport equation for the modified diffusivity, $\tilde{v}$, is expressed as follows:

$$\frac{\partial(\rho\tilde{v})}{\partial t} + \nabla\cdot(\rho\tilde{v}\overline{u}) = \frac{1}{\sigma_{\tilde{v}}}\nabla\cdot\left[(\mu+\rho\tilde{v})\nabla\tilde{v}\right] + P_{\tilde{v}} + S_{\tilde{v}} \tag{2.44}$$

Where $S_{\tilde{v}}$ is a user-defined source term, and $P_{\tilde{v}}$ is the production term, which is composed of a combination of the following terms: the non-conservative diffusion term, the turbulent production term, the nonlinear production term, and the turbulent dissipation term. The computation of the aforementioned terms, along with their respective constants, is extensively documented in the literature.

2.3.6 Wall Treatment

In order to accurately simulate the flow behavior in the near-wall zones, it is imperative to provide a comprehensive description of the boundary layer and its corresponding sub-zones. Therefore, it proves beneficial to establish a clear definition of the characteristic quantities:

- **Wall shear stresses**: Due solely to the presence of the viscous component.

$$\tau_w = \rho\nu\left(\frac{\partial\langle U\rangle}{\partial y}\right)_{y=0}$$

- **Friction velocity**:

$$u_\tau = \sqrt{\frac{\tau_w}{\rho}}$$

- **Viscous lengthscale**:

$$\delta_\nu = \nu\sqrt{\frac{\rho}{\tau_w}} = \frac{\nu}{u_\tau}$$

- **Y plus**: The distance from the wall is measured according to the defined viscous lengths.

$$y^+ = \frac{y}{\delta_\nu} = \frac{u_\tau y}{\nu}$$

It is evident that the expression of y^+ exhibits similarity to the definition of a local Reynolds number. As a result, the value of this quantity determines the relative importance of both the viscous and turbulent effects.

The figure below illustrates the relationship between the two types of stress and their respective trends as a function of y^+:

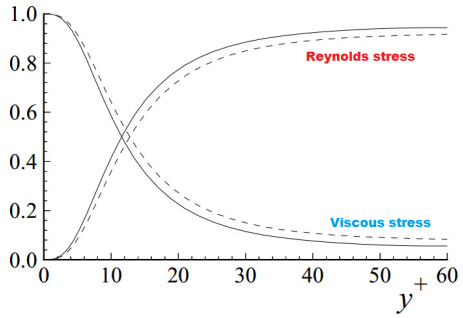

Figure 2.8: Reynolds & Viscous stress trend as a function of y^+

Based on the value of the already defined parameter y^+, the boundary layer can be classified into the following distinct regions:

- **Viscous sublayer**: $y^+ < 5$. The Reynolds stresses are negligible compared to viscous stresses. By defining the dimensionless velocity (the viscous scales averaged velocity profile) with $u^+ = \frac{\langle U \rangle}{u_\tau}$. It can be affirmed that in this specific area, y^+ is equivalent to u^+.
- **Buffer layer**: $y^+ < 50$. The viscous effects continue to influence the total shear stress.
- **Outer layer** : $y^+ > 50$. In this zone the viscous effects become negligible.

Within the region where $y^+ > 30$, the velocity profile adheres to the logarithmic law as follows:

$$y^+ = \frac{1}{\kappa} ln(y^+) + B,$$

where $\kappa = 0.41$ called *von Karman*'s constant, and B=5.2= constant.

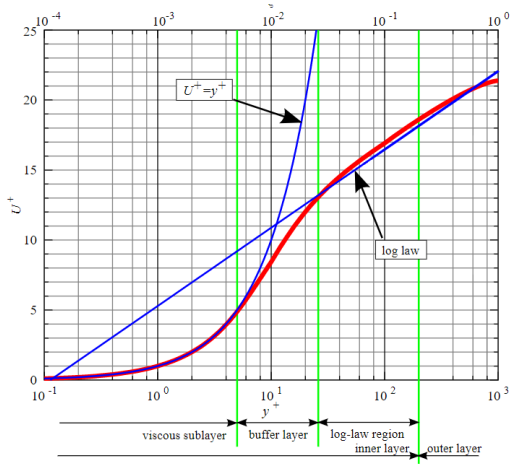

Figure 2.9: Trend of the two wall laws as a function of y^+

The wall treatment in Star CCM+ exhibits a strong correlation with the chosen turbulence model. Once the turbulence model is selected, the associated wall treatment method is automatically determined. In the Star CCM+ software, a range of wall treatment options is available, encompassing the following variants:

- **High-y+ wall treatment:** This wall treatment methodology is predicated on the assumption that the cells adjacent to the wall are situated within the logarithmic region, wherein the application of wall functions is relevant. These wall functions entail a set of mathematical relationships employed to establish appropriate boundary conditions. Consequently, this approach renders the turbulence model valid solely in regions external to the boundary layer, where viscous stresses exert minimal influence. Conversely, the boundary layer region, wherein viscous stresses play a significant role, remains unresolved within this framework.

- **Low-y+ wall treatment:** This particular wall treatment approach is specifically applicable to turbulence models designed for low Reynolds numbers. It operates on the assumption that the viscous sublayer is accurately resolved. Low Reynolds number models are known to be valid across the entire boundary layer, encompassing the viscous sublayer. However, in order to resolve the intricacies of the viscous sublayer, such models necessitate a sufficiently fine grid resolution. Consequently, the computational cost associated with these models can be quite significant, and it tends to increase with higher Reynolds numbers

- **All-y+ wall treatment:** This wall treatment represents a hybrid approach that aims to replicate the characteristics of both high-y+ wall treatment for coarse grids and low-y+ wall treatment for fine grids. As such, it attempts to provide accurate results even for grids with intermediate resolutions, particularly when the cell centroid lies within the buffer region of the stratum limit. By employing this hybrid treatment, the ALL Y+ approach achieves a balanced simulation of the wall boundary layer dynamics across a range of grid resolutions, thereby enabling reliable predictions in scenarios where the grid falls within the transitional regime.

In our different case study, the ALL Y+ wall treatment is employed.

2.3.7 Spatial Discretization

The term discretization refers to the substitution of an exact and continuous solution of our system of partial differential equations (PDE) by an approximated numerical solution in a discrete domain. It can be implemented with different methods:

- Finite Element Method FEM

- Finite difference method FDM

- Finite Volume Method FVM

The majority of the commercial codes currently in use, including Star CCM+, are based on the finite-volume discretization method. The main reasons lie in its simplicity, generality and it's ability to use both structured and unstructured mesh.
The finite volume method was developed in the 1970s in the field of computational fluid dynamics. In this methodology the computational domain is divided into many small volumes called 'cells',

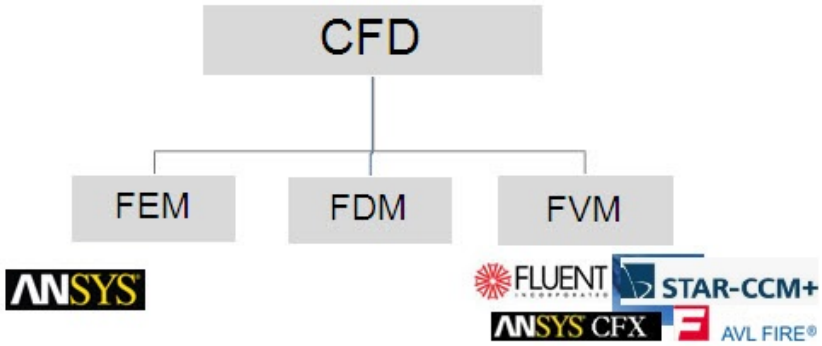

Figure 2.10: CFD Discretization Techniques and Examples of Commercial Softwares

and the discretization is applied directly to the equations written for a finite control volume in integral form. Let's consider the following conservation equation written in integral form:

$$\frac{d}{dt}\int_{\Omega}\Phi d\Omega = -\int_{S}\Phi V\cdot ndS + \int_{S}\chi\nabla\Phi\cdot ndS + \int_{\Omega}Qd\Omega. \tag{2.45}$$

This equation is written for a generic scalar quantity Φ, for an arbitrary control volume Ω and its surface S with a normal vector n.
The term on the left of the equation represents the total variation of Φ inside Ω, while the integrals on the right-hand side represent how Φ can change (convective and diffusive flow).
The finite volume scheme is derived by applying this conservation equation on each cell of the computational domain. The next step is to approximate the integrals of the equation, by substituting each integral with a discretized algebraic equation. At this point the discretized equations of all our domain cells form the numerical system to be solved. More attention must be paid on the boundary of the computational domain, where the surface integrals are modified to take account of the imposed boundary conditions.

2.3.8 Temporal Discretization

In this section, we will provide a concise overview of the discretization process for the unsteady term in the conservation equation. Various methods have been developed to tackle this task, all of which rely on the finite difference method. However, our discussion will center on highlighting the two most widely employed schemes, which are considered standard practices in the field:

- **Explicit:**
  This categorization is referred to as explicit because it enables us to explicitly express our unknown variable in relation to the known quantities. It employs a forward time scheme, which means it progresses the solution in a time-stepping manner. Typically, it is coupled with a space-centered scheme, resulting in its designation as *FTSC (Forward Time Centered Space)*.

$$\frac{u_i^{n+1}-u_i^n}{\Delta t} + a\frac{u_{i+1}^n - u_{i-1}^n}{2\Delta x} - \nu\frac{u_{i+1}^n - 2u_i^n + u_{i-1}^n}{\Delta x^2} = 0. \tag{2.46}$$

  Where: $u_i^{n+1} = f(u_i^n, u_{i-1}^n, u_{i+1}^n)$.

- **Implicit:**
  The solution is implicit, meaning it is not feasible to express the unknown variable explicitly in terms of the other quantities. Consequently, all the terms are computed at the time "n+1," except for the term present in the time derivative. This approach is known as a backward time scheme, as it involves backward stepping in time. It is commonly referred to as *BTCS: Backward Time Centered Space* due to its combination with a centered space scheme.

$$\frac{u_i^{n+1} - u_i^n}{\Delta t} + a\frac{u_{i+1}^{n+1} - u_{i-1}^{n+1}}{2\Delta x} - \nu\frac{u_{i+1}^{n+1} - 2u_i^{n+1} + u_{i-1}^{n+1}}{\Delta x^2} = 0. \tag{2.47}$$

Interestingly, while an implicit scheme requires more computational effort compared to its explicit counterpart, it offers several advantages that make it widely employed in practice. One notable benefit of implicit methods is their improved numerical stability properties. They are less prone to numerical instabilities, which can occur with explicit methods. Moreover, implicit schemes allow for the utilization of larger time steps, which can significantly expedite the convergence toward the desired solution. This capability arises from the inherent nature of implicit methods, where all terms except the time derivative are evaluated at the future time level (n+1). By incorporating information from future time levels, implicit schemes exhibit better stability and are capable of capturing transient phenomena with greater precision. Additionally, implicit methods provide flexibility in handling a wide range of problems, including those with highly nonlinear or non-uniform behavior. Their ability to handle stiff equations, which involve rapid changes or disparate time scales, further enhances their utility in practical applications.

2.3.9 Boundary Conditions

Each CFD simulation focuses on a specific aspect of the physical reality under investigation. Upon reaching the boundary of the numerical domain, careful consideration must be given to the encountered conditions, which necessitates the utilization of boundary condition classes to simplify the task. This phase carries significant importance as an inappropriate selection of conditions can undermine both the stability and efficiency of the solution. In this section, we illustrate a selection of frequently employed boundary conditions within the field of CFD.

- **Wall:** This condition is employed when solid walls are present, specifically in our case, referring to the surface of the blades and spokes. The no-slip condition serves as the default setting for viscous flows, ensuring that there is zero relative velocity between the fluid and the solid boundary. Additionally, for turbulent flows, the calculation of shear stress is performed using the designated turbulence model chosen for the simulation.

- **Velocity-Inlet:** This condition is employed to establish the flow velocity, along with all associated scalar properties of the flow, at the inlet zone. It offers the flexibility to specify either constant or variable parameters, as well as they can alternately be distributed uniformly or not uniformly along the boundary itself.

- **Pressure outlet:** By applying this condition, a predetermined static outlet pressure is set, while simultaneously allowing for a range of back-flow conditions to mitigate convergence challenges. Additionally, in simulations involving rotating domains, a radial equilibrium distribution is incorporated, enabling the determination of the pressure gradient as a function of the distance from the axis of rotation, denoted as 'r,' and the tangential velocity component, denoted V_t.

$$\frac{\partial p}{\partial r} = \rho \frac{V_t^2}{r}$$

- **Simmetry:** This condition establishes a mirrored face or surface and should be exclusively applied when the physical object or geometry, as well as the anticipated flow field pattern of the resulting solution, exhibit mirror symmetry along that specific surface.

In our analysis, all of these boundary conditions were employed. In the 2D study, only the first three conditions were utilized, whereas the last condition was incorporated specifically for the 3D case. This addition allowed us to leverage the symmetry plane, thereby avoiding the need to simulate the entire height of the turbine in some specific cases.

2.3.10 Coupled and Segregated Flow

To solve the pressure and velocity equations in computational fluid dynamics, both coupled and segregated flow models can be used with different numerical algorithms and techniques. Each of these flow models has its advantages and considerations:

- **Coupled Flow Model:** It offers a computational approach that solves the conservation equations of mass, momentum, and energy simultaneously through pseudo-time marching. This formulation exhibits robustness in accurately capturing flows with dominant source terms, such as rotational flows. Additionally, the computational time required by the Coupled Flow model scales linearly with the number of cells, ensuring that the convergence speed does not excessively deteriorate with increasing grid resolution. The model also supports the incorporation of preconditioning matrices within the governing equations, both in integral and discretized forms. As a result, it enables the solution of compressible and incompressible flows across a wide range of speeds.

- **Segregated Flow Model:** It represents a distinct resolution algorithm where the governing equations are solved sequentially, i.e., independently of each other. This approach proves to be memory-efficient since the equations only need to be stored in memory one at a time when discretized. However, the Segregated Flow model exhibits relatively slow convergence due to the decoupled nature of the solution process, as each equation is resolved independently without considering the full coupling among the governing equations.

Chapter 3

Research Framework

3.1 Introduction

In deep-sea areas (more than 50 m depth), which possess the majority of the offshore wind energy potential, installing wind turbines on floating foundations is the only feasible solution [45]. This introduces a new set of challenges as the tower and rotor are subjected to highly unsteady loads caused by the presence of sea waves [45]. Further research and development efforts are required for floating offshore wind turbines (FOWTs). In fact, these efforts are being undertaken as part of international research projects such as OC6 or IEA Task 47. Consequently, exploring alternative configurations becomes crucial from both scientific and technical perspectives.
In such a research context, the lift-driven VAWTs, based on the Darrieus patent [5], represent a distinctive alternative configuration that has the potential to compete with the HAWTs. Darrieus obtained a patent for his idea prior to the widespread adoption of Horizontal Axis Wind Turbines (HAWTs). During the patent presentation, his concept was believed to surpass all other existing devices for converting wind energy in terms of theoretical performance. Although the VAWT was defeated by the HAWT in both onshore and offshore fixed-bottom wind farm setups. This was primarily due to the VAWT's complex aerodynamics, which led to inherent rotor unsteadiness, periodic operation of airfoils in post-stall and deep-stall conditions, and the involvement of fully three-dimensional aerodynamics, for both H-shaped and the 'egg-beater' rotor design [49]. These three primary characteristics posed significant limitations to the development of VAWTs across multiple aspects: i) The inherent unsteadiness of VAWTs resulted in time-varying fatigue loads on the blades and supporting structures such as spokes and struts. This also led to pulsating bending moments on the tower structure, often necessitating the use of guy wires for the egg-beater rotors. ii) The initiation of stall conditions in VAWTs led to reduced efficiency and introduced uncertainty into the design process. iii) The distinctive shape of the VAWT rotor greatly complicated the calibration of engineering design codes. This complexity arose from the reliance of these codes on either experimental benchmark data or on fully 3D and unsteady CFD. Despite these complex aerodynamic aspects and their resulting effects, the VAWT technology offers distinct advantages over the HAWT [32]. As mentioned, some of these are particularly relevant for Floating Offshore Wind Turbines (FOWTs): i) The VAWT design allows the rotor to be less affected by changes in yaw angle and flow skewness, which are promoted by the motion of the platform [79]. ii) Installing the gearbox, electric generator, and other heavy components at the base of the turbine can reduce installation and maintenance costs [57]. iii) The increase in blade root tensile stress with the rotor diameter, caused by the weight-induced moment, can be alleviated by adjusting the H/D ratio. This is an advantage that HAWTs cannot achieve.

The application of VAWTs in the context of Floating Offshore Wind Turbines was introduced through the EU-FP7 Deepwind research program [70]. This program focused on exploring the scalability of VAWT rotors to larger dimensions, which is crucial for reducing the levelized cost of energy LCOE. The DeepWind project demonstrated that the troposkein shape, possibly with certain modifications as discussed in [70], could be an optimal rotor configuration actually feasible in FOWTs applications.

As previously mentioned, lift-driven VAWTs showcase a wide array of configurations [18], including the H-shaped, Troposkien [15], V-shaped [86], and Helical [90]. This Ph.D. thesis centers on the aerodynamic behavior of the first two solutions while operating in different flow conditions. An overview of the analyzed cases is provided in this chapter, while the in-depth studies are presented separately in the next chapters.

3.1.1 Summary and Motivations

Parameter	Troposkein model	Deepwind Demonstrator	H-shaped model
Blades	3	3	3
Blades height[m]	1.51	1.902	2.02
Rotor Diameter[m]	1.51	2.02	2.02
Chord[m]	0.086	0.101	0.101
Solidity[Nc/R]	0.34	0.30	0.30
Rotation speed[rpm]	400	300	300
Blade airfoil	NACA0021	DU06W200	NACA0021
Swept area[m^2]	1.5	2.63	4.08
Rotor tilt angle	0°	0° - 15°	0°-10°-20°-30°
Reynolds$_{eq}$ @ Peak condition	1.2 x 10^5	1.8 x 10^5	1.8 x 10^5

Table 3.1: Cases of studies: Summary

Table 3.1 summarizes the various design and operational parameters associated with the three case studies. Although the initial impression might suggest a similarity between the first two machines configured with troposkein shape, a closer examination reveals fundamental distinctions, as detailed in the table. The decision to investigate both machines stems from two primary motivations. Firstly, it is attributed to the availability of experimental data, which proved essential in validating the chosen numerical settings. Secondly, this choice was driven by the desire to ascertain whether the observed results and performance trends exhibit variations, and if so, to comprehend the nature of these variations in response to alterations in the machine's design and operational conditions. Following the considerations on the machine solidity given in Chapter 1, the selected machines are characterized by a solidity value of approximately 0.3. This is tightly related to a design approach for small-scale relatively high-solidity VAWTs, in order to keep optimum turbine rotational velocity, properly to minimize vibrations. Different operating conditions were investigated on the small-lab troposkein model and the Deepwind demonstrator with the objective of assessing the impact of the blade airfoil and the blade stocking line on the performance indexes. The inherent non-linearity of relevant fluid dynamic phenomena makes more complex the evaluation of the machine behavior and thus restricted and selected topics of interest and parameters of variations are considered among those available from experimental data sets. Taking into account these considerations, the two troposkein-based VAWTs have

been studied to draw physical interpretations and performance evaluations for typical design and off-design operation conditions. The relevant parameters of variation having an impact are the blade design, the flow regime, and the upright and inclined state.

Subsequently, the third case study related to the H-shaped VAWT emerged as a natural progression from the examination of the second machine. Its objective was to conduct a comprehensive exploration of the tilted operational condition that characterizes vertical-axis wind turbines deployed in floating applications. It is worth noting that only a few works in the existing literature offer insight into this particular operation condition. The H-shaped configuration provides the advantage that a portion of it encounters a clean flow in the downwind zone, in addition to an increase in its swept area, resulting in higher power harvesting. This advantage is absent in the troposkein configuration.

3.2 Cases of Study: Overview

3.2.1 Troposkein VAWT

During the 1970s and 1980s, the troposkein VAWT technology underwent a systematic study at Sandia Lab [43, 22, 75]. However, it fell behind in competition against the HAWT, leading to a halt in VAWT development. Renewed interest in VAWTs emerged in the early 21st century, with a particular focus on small-scale distributed applications. In such contexts, simpler rotor designs like straight-blade H-shaped rotors proved more cost-effective than troposkein designs. Consequently, the majority of research efforts shifted towards these types of VAWTs, resulting in a significant expansion of knowledge in the field. Recent works have enriched the experimental database on prototypes at the laboratory scale [65, 35, 87, 31, 52, 54, 15], enhancing modeling techniques [85, 12, 10, 11, 26, 21], and investigating operational issues concerning VAWTs[78, 50, 66, 14, 64, 41]. Over the past twenty years, there has been a scarcity of studies focusing on the detailed aerodynamics of the troposkein configuration. Some documented studies have examined experimental models of troposkein VAWTs in laboratory settings [17, 15, 73], while others have employed low-fidelity engineering tools for theoretical analysis [82] (using a blade-element momentum model) and [83] (using a lifting-line free-vortex wake model). Additionally, CFD simulations have been presented in [28, 89]. This creates a noticeable disparity between the level of understanding achieved for simplified straight-blade VAWT rotors and the knowledge currently available for the troposkein configuration. To bridge this gap, high-fidelity CFD investigations can play a key role. They possess the capability to provide reliable assessments of performance and loads, as well as generate good representations of airflow, which are necessary for a comprehensive understanding of the aerodynamics of the turbine.

The chapter related to the Troposkien VAWT introduces a computational study conducted on a laboratory model of a troposkein VAWT. The study is supported by a comprehensive collection of experimental data regarding the turbine's performance and the velocity field in its wake, which has been documented in references [15]. Initially, the machine is studied with a series of two-dimensional (2D) simulations, specifically targeting the equatorial section of the rotor. The aim of those simulations is to gather initial insights into the machine's performance across its entire operational range. These computations serve a dual purpose: (i) to evaluate and refine the CFD tool being utilized and (ii) to acquire an initial understanding of modeling and operational challenges associated with the turbine. Afterward, full 3D simulations are presented and discussed for the turbine operating at high load and at peak efficiency conditions. By comparing the experimental data with the results obtained from 2D/3D CFD simulations important and peculiar features of the troposkein rotor aerodynamics are revealed. To further enhance the understanding of the design of the troposkein rotor, the impact of the blade stacking angle

is examined through a dedicated set of 3D CFD simulations. The investigation gives valuable recommendations and guidelines for the design of future troposkein rotors.

3.2.2 Deepwind Demonstrator

The FP7 European-funded DeepWind Project was presented in 2010, during a period marked by significant advancements in emerging technologies. These advancements encompassed the development of floating spar buoys, mooring systems, direct drive sub-sea generators, and a highly-controlled pultrusion process for blade manufacturing. These innovations were effectively incorporated to achieve the goal of developing a more economically efficient turbine in contrast to conventional models [17]. The Deepwind concept introduced a novel approach, featuring a large-scale Troposkien-shaped VAWT with a capacity of 5 MW (with potential considerations for further expansion up to 20 MW), positioned on a floating platform as its base, with the integration of a direct drive sub-sea generator into its structure.

In order to foster the deployment of the DeepWind concept, different studies were carried out to improve the design and behavior of this machine [70, 72, 17, 19, 20]. One essential consideration in the DeepWind concept's design is to limit the inclination angle to no more than 14 degrees [71]. Despite the integration of spar technology into the floating platform and a low center of gravity providing a significant stabilizing force, there's an expectation that the rotor may experience tilting during operation. This tilting action acts similarly to a gyroscopic effect, causing the rotor to trace an elliptical trajectory on the water surfaces [71]. Experiments using a scaled model of the DeepWind turbine were conducted in the Politecnico di Milano wind tunnel, to assess the turbine's performance under both upright and tilted configurations [17]. Specifically, the investigation was conducted to quantify the impact of a 15-degree tilt angle. This particular challenge has raised several concerns regarding the aerodynamic behavior of the turbine. The experimental results obtained on the DeepWind demonstrator in [17] draw attention to the C_P decrease in skewed flow conditions.

Therefore further investigations were necessary to gain a deeper understanding of the machine, both in upright and tilted conditions. The chapter related to the Deepwind Demonstrator presents a comprehensive numerical study aimed at gaining insights into the performance of the Deepwind concept, with a comparison to available experimental data covering both upright and tilted conditions, with detailed descriptions of the numerical settings and preliminary considerations regarding turbulence modeling. In the upright orientation, 2D and 3D computations were performed to assess the predictive capabilities of the chosen discretization schemes by evaluating the integral power coefficient, providing an early quantification of turbine performance. In the tilted condition, due to the absence of symmetry, only the 3D simulations were performed. A relevant issue connected to the performance reduction in the presence of tilting is the lowered effective incoming velocity. In addition, the turbine architecture minimizes the rotor sensitivity to skewed flows, and lower aerodynamic efficiency is expected when the rotor is tilted (as instead obtained when an H-shaped VAWT is tilted - no fresh air benefits). For a more detailed assessment of energy harvesting capability, the near wake-field was pointwise computed, examining how the turbine extracts energy across the spanwise position in order to capture local flow field behavior. Moreover, considerations regarding near-wake recovery, are reported. The study also sheds light on the limitations of the scaled rotor model, as it doesn't match the Reynolds number of the full-scale model.

3.2.3 H-shaped Configuration

An accurate assessment of H-shaped VAWT's performance necessitates the comprehensive evaluation of the impact of skewed flow conditions. The inclined condition is a peculiarity of the floating application with the spar-buoy substructure, but a similar skewed flow also affects the flow on top of high-rise buildings due to the flow blockage caused by the building itself, making this latter case aerodynamically similar to VAWTs in floating offshore applications, as shown in [13]. As reported in the open literature (see e.g.[80, 84, 66]) H-Darrieus VAWTs in skewed flow may increase their harvesting capability above that for upright conditions.
Given that the VAWT configurations exhibit a lower center of gravity and permit a greater range of floater tilt angles, it is common practice to design VAWTs with a static tilt angle that is typically double the value employed in horizontal wind turbines, as indicated by [33]. VAWTs typically feature a static tilt angle within the range of 10-15 degrees. In the case of H-shaped VAWTs installed on offshore floating platforms, special consideration is given to maintain dynamic tilt angles and accelerations at the electrical generator at minimal levels. Consequently, these H-shaped VAWTs are engineered to ensure that the pitch and roll angles about the vertical axis do not surpass a critical threshold of approximately $\pm 15°$. However, higher inclination angles have been considered for example in [53, 84] for a floating offshore installation and in [80] for a roof-located wind turbine. In the latter case, the maximum power coefficient as a function of the skew angle started to decrease at about 25 degrees inclination.
The main purpose of the H-shaped VAWT chapter is to provide a step forward in comprehending VAWT aerodynamics and their performance prediction when dealing with skewed flows. Computational Fluid Dynamics (CFD) was applied to obtain a high-fidelity representation of the flow field, thus achieving a deeper insight into the complex fluid dynamic behavior characterizing the H-shaped VAWT operating in upright and tilted configurations. The computational setting adopted was extensively validated against experiments [37, 39, 38] carried out to investigate the performance of H-shaped and Troposkein VAWTs. Various factors contribute to the overall behavior of the turbine, including geometry parameters, design criteria, and operating conditions. Preliminary test cases are presented to study the energy harvesting process and related wake development when the machine is operating in an upright position. A detailed baseline study is thus presented to understand how the energy harvesting capability is established at different operating conditions within different sections of the machine, splitting the overall power collected at the shaft by considering turbine slices (spanwise defined) to characterize the impact of flow field structures on the turbine performance. Evaluation of the viscous losses due to struts, blade tips, and vortical structures arising within and downstream of the rotor is provided. Then the tilted configuration is investigated by considering different inclination angles and operating conditions.

Chapter 4

Case 1: Troposkein VAWT

4.1 Case study

The turbine under consideration is a 1-kW class machine with specific dimensions and characteristics. It possesses an equatorial radius of 0.755 m, a height of 1.51 m, and a blade length of 2.233 m. These dimensions result in a swept area of 1.5 m^2. The rotor consists of three blades that employ NACA0021 profiles, each with a chord length of 85 mm. The operational points of this turbine are established at a fixed angular speed of 400 rpm. This machine serves a dual purpose. On one hand, it can be viewed as a real-scale turbine suitable for distributed micro-generation. On the other hand, it can be seen as a small-scale laboratory model representing a utility-scale device. To evaluate its performance, experimental tests were conducted in the large-scale wind tunnel of the Politecnico di Milano [15].
In Figure 4.1, the upper half of the turbine and its corresponding coordinate system are illustrated. The blade stacking line, denoted as r(z), is positioned at the midchord of the airfoil. The cylindrical coordinates can be referenced in [15]. Beginning at $\theta = 0^o$, the turbine's first and second quarters correspond to the upwind side, while the third and fourth quarters represent the downwind side. Likewise, the fourth and first quarters can be identified as the windward portion of the revolution, whereas the second and third quarters constitute the leeward section.

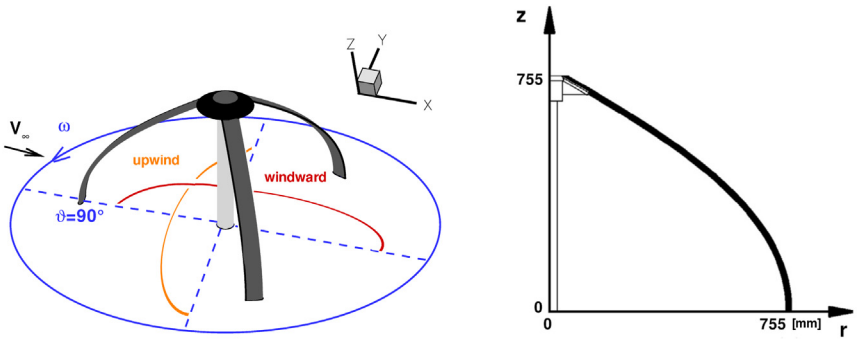

Figure 4.1: 3D troposkein VAWT (left) – blade radial profile r(z) (right).

In this study, two variations of the rotor are taken into account, with both versions sharing the same number of blades, blade profile, and troposkein curve. The first turbine, referred to as the "base" or "slanted" rotor, represents the laboratory model used for testing in the wind tunnel. In

this particular turbine, the rotor was constructed by bending the initially straight blade beams to match the prescribed troposkein curve(z). Consequently, the blade profile is perpendicular to the troposkein curve rather than aligned with the axis of rotation. As a result, except for the midspan section, the profile exhibits increased thickness when observed in a plane perpendicular to the axis of rotation. Within the quasi-linear segment of the troposkein, which encompasses approximately half of the rotor's axial span, the airfoil thickness increases to approximately 30 % of the chord length. To assess the potential impact on performance and load due to the chosen manufacturing method, which is undoubtedly the most cost-effective, a second turbine model was developed. This model incorporates plane airfoil profiles (perpendicular to the turbine axis) consistently along the entire blade. Therefore, this turbine is referred to as the "plane" rotor throughout the following analysis. Figure 4.2 illustrates the variation in blade profile thickness as one moves towards the turbine tip, specifically in the section marked as slice number 10. It is important to note that the turbine with the plane version of the blade profile was solely simulated numerically. The obtained results will be analyzed and compared to those achieved for the "base" turbine.

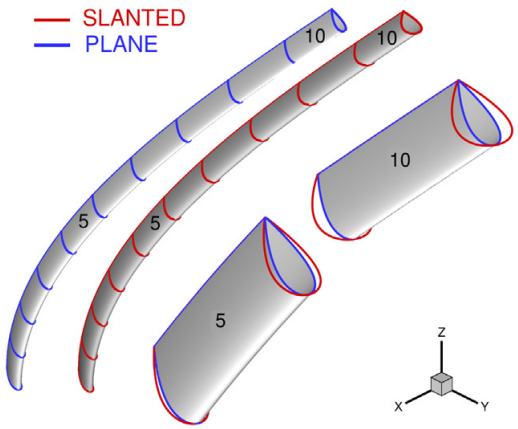

Figure 4.2: Blade profile and cross section for the "slanted" and " plane" version of the blade.

4.1.1 Computational models

The main focus of this study involves conducting high-fidelity simulations of VAWTs. Starting with the one mentioned earlier, the simulations include detailed 2D calculations of the equatorial section of the turbine, which are applicable to both the plane and slanted rotor configurations. Additionally, 3D simulations are performed on a half model of the turbine for the two mentioned configurations (plane and slanted). The CFD solver STAR-CCM+, developed by Siemens, was utilized to perform flow calculations. To accurately capture the flow behavior within the turbine, the U-RANS equations were solved along with turbulence models that effectively resolved the flow near the wall. For this study, the $k-\omega$ SST turbulence model is considered in two formulations: the standard fully-turbulent (or high-Reynolds) version and its low-Reynolds counterpart (referred to as HR and LR, respectively). Additionally, the Spalart-Allmaras model (denoted SA) is considered as another turbulence model option. It is important to note that the low-Reynolds version of the $k-\omega$ two-equation model incorporates ad-hoc modifications to the model coefficients. These modifications are specifically designed to handle natural transition effects in a computationally efficient manner, following the approach proposed by Wilcox [92]. Furthermore,

the SA model initially developed for simulating external flows, has recently been explored in the context of local transition approaches. It has been tested for airfoils operating at Reynolds numbers commonly observed in wind turbine blade sections [30]. The fluid was considered to be incompressible with constant thermophysical properties. Second-order accurate schemes were employed for both the divergence and Laplacian terms in the equations, as well as for temporal discretization. The time advancement was based on a backward differentiation formula BDF2, ensuring accurate temporal resolution. As established in different previous studies [37, 39], the choice of time step value significantly affects the accuracy of the solution and should be carefully determined in conjunction with other solver parameters. In this particular study, 720 time steps per revolution were utilized. This value was determined after conducting a preliminary sensitivity analysis, which indicated that additional refinement (1440 time step) was unnecessary. At each time step, the system of governing equations was solved using an algebraic multigrid solver. The solver iterated until a predetermined accuracy threshold was met, ensuring the desired level of solution accuracy. The computations were conducted for each operating condition until a periodic solution was obtained. In each analyzed test case, the achievement of a stable flow field was observed following at least 20 revolutions of the turbine. The mean torque value, computed at the shaft and averaged over a single revolution of the rotor, was recorded. To ensure the attainment of satisfactory periodicity, the last ten mean torque values were continuously monitored. To determine the periodicity of the computations, the root-mean-square (RMS) value, based on the ten recent revolutions, was considered. This RMS value was normalized over the corresponding mean value and compared against a predefined threshold. The computations were considered periodic when the normalized RMS value reached a fixed threshold.
The prescribed boundary conditions at the inlet surface include a fixed freestream velocity, a turbulence intensity of 1%, and a turbulent viscosity ratio of 1. These selected turbulence values were chosen in accordance with experimental turbulence data. For the lateral, downstream, and top boundaries (in 3D simulations), static pressure is prescribed. The no-slip condition is enforced on solid (rotating) surfaces. Additionally, a symmetry condition is applied to the equatorial plane in the 3D simulations. In fact, due to the rotor's shape and the uniform inlet flow in the reference-controlled experiment, the aerodynamics of the rotor and the development of its wake can be considered symmetric.
The simulations were conducted with domains appropriately expanded beyond the rotor. The extension of the domain is a critical factor in optimizing memory usage, CPU time, and overall computational expenses. For effectively configuring the domain for a H-shaped VAWT, established guidelines are reported in [37]. However, The last mentioned study confirmed that in three-dimensional simulations, the blockage caused by the rotor was lower compared to two-dimensional simulations. This is due to the fact that in 3D, the flow that bypasses the rotor is not limited to lateral movement but can also pass above the rotor. In the current study, the troposkein shape of the considered rotor results in an additional reduction in turbine blockage compared to the H-shaped configuration. As a result, the criteria established in the previous work regarding the H-shaped rotor ([37]) can be directly applied in this case. After conducting a sensitivity analysis using progressively larger meshes, the computational domain for 2D simulations was ultimately expanded to cover a distance of 4.5 equatorial rotor diameters upstream from the rotation axis, 12 diameters laterally, and 3 diameters downstream. Due to the reduced blockage effect mentioned earlier, the 3D simulations utilized the same domain as the 2D simulations, with the exception of the lateral boundaries, which were positioned at a distance of only 3 diameters from the axis. Finally, the spanwise extension of the 3D domain reached a height equal to twice that of the half-turbine model.

4.1.2 Mesh resolution

In this research, the U-RANS equations are employed to solve fluid flow problems. The integration was performed over unstructured hybrid meshes, which consist of cells with varying shapes. Specifically, quadrilateral and hexahedral elements were utilized in the O-grid surrounding the blades, while polygonal elements were employed away from the walls. The selection of mesh resolution was based on a comprehensive grid-convergence study conducted on an H-shaped VAWT [37]. However, the aforementioned study was limited in its applicability to the definition of the 2D mesh in the equatorial section. In contrast, the herein research was specifically focused on establishing the criterion for constructing the 3D mesh over the troposkein rotor, which will be thoroughly examined and addressed. For the initial 2D analysis of the vertical-axis wind turbine, an equatorial mesh consisting of 200,000 cells, referred to as the "fine" mesh (2Df), was utilized. This mesh was constructed based on established literature guidelines [37] and maintained a minimum spacing perpendicular to the airfoil surfaces, which is $2 \cdot 10^{-4}$ times the blade chord. In all the cases presented in this study, the chosen minimum spacing was found to be adequate, guaranteeing a y^+ value below one on all wall surfaces.
Figure 4.3 illustrates the mesh of the inner rotating domain, as well as a close-up near the blade's solid surface.

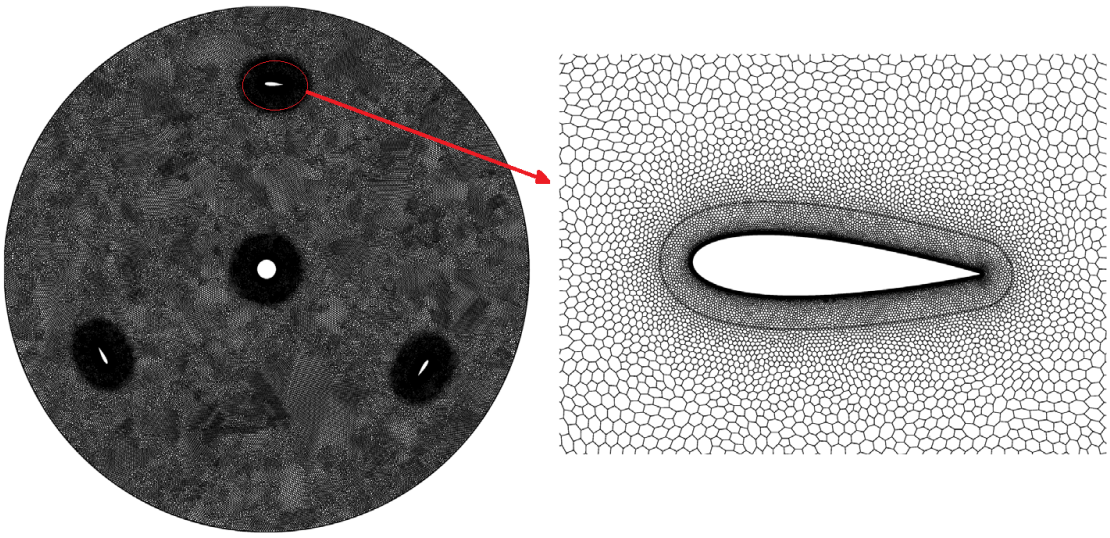

Figure 4.3: 2D fine grid: detail of the rotor region (left) and around an airfoil (right).

In addition, creating an appropriate 3D mesh for a troposkein VAWT is a relatively new and challenging task in scientific research, carrying significant technical implications. The same topic was addressed in [37] for an H-shaped VAWT. However, due to the complex geometry of troposkein rotors, it is not feasible to directly apply the criteria discussed in the last cited study to the present context. Without explicit guidelines, one could potentially choose to construct the 3D mesh by utilizing the same resolution as the 2D mesh. Indeed, the length scales of the local flow structures, such as airfoil wakes, detachment vortices, and pressure fields, generated around the airfoils in the equatorial section, are anticipated to maintain a consistent order of magnitude across all rotor sections along the machine's span. This is due to the lack of variation in the blade profile. Furthermore, it is expected that the spatial scales of 3D flow phenomena occurring in the tip regions of the rotor will be at least one order of magnitude larger than those

related to the airfoils. This significant difference in scale arises from the fact that the rotor itself is approximately ten times larger than the individual airfoil. However, adopting the resolution of the finely detailed 2D mesh would create a 3D grid consisting of over 50 million elements. This very large value could impede the ability to conduct multiple CFD analyses for diverse operating conditions and blade configurations, which is the primary objective of this study.

To ascertain the maximum cell size that can yield precise two-dimensional outcomes, a thorough grid dependence analysis of the 2D equatorial mesh was undertaken prior to commencing the 3D simulations. The initial mesh, denoted as "coarse" or 2Dc hereafter, was generated utilizing 50,000 cells. Subsequently, we employed the same resolution of the "coarse" mesh to construct the 3D mesh, resulting in the creation of a grid comprising approximately 10.7 million elements. This element count is comparable to those employed in previous investigations concerning the H-shape rotor. Furthermore, in order to achieve a balance between computational efficiency and enhanced accuracy, an intermediate grid, denoted as "medium" or 2Dm hereafter, was generated, consisting of 120,000 cells.

Upon utilizing the three aforementioned meshes, initial two-dimensional computations conducted at TSR_{eq}= 4.0 exhibited minimal disparities. However, as the analysis was extended to lower TSRs, notable discrepancies emerged, probably attributable to the increased separation and subsequent activation of vortex shedding observed under those operational conditions.
Except for the two lowest TSRs, where the coarse mesh demonstrated evident limitations in generating accurate outcomes, Table 4.1 displays the 2D power coefficient across the entire operational range for the aforementioned meshes with different turbulence models.

		TSR2.0	TSR2.4	TSR3.1	TSR4.0
2Dc	HR	-	-	0.338	0.270
	LR	-	-	0.351	0.284
	SA	-	-	0.362	0.240
2Dm	HR	0.067	0.137	0.365	0.269
	LR	0.108	0.203	0.379	0.286
	SA	0.141	0.273	0.385	0.260
2Df	HR	0.071	0.165	0.366	0.271
	LR	0.110	0.205	0.380	0.283
	SA	0.142	0.271	0.386	0.262
Exp	-	0.092	0.189	0.345	0.220

Table 4.1: Power coefficient as a function of TSR computed on different 2D grids, using selected turbulence models, in comparison with measurements

Irrespective of the turbulence model employed, the "medium" grid consistently yielded grid-independent results for TSR_{eq} values of 4.0 and 3.1, as confirmed by the obtained results. Therefore, the "medium" mesh was selected as the initial basis for generating a subsequent 3D mesh. Herein, all solid surfaces were ensured to maintain a y^+ value in the order of unity, while preserving the same characteristic spacing as the medium mesh. Particularly, this medium-sized 3D mesh encompassed a total of nearly 32 million elements. Figure 4.4 shows spanwise images of the coarse and medium 3D meshes.

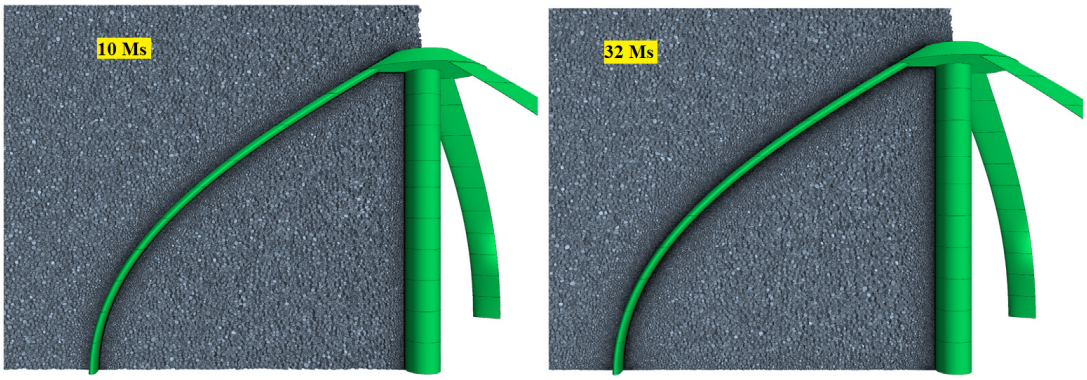

Figure 4.4: 3D computational domain, 10Ms (left) vs 32Ms (right) cells.

4.1.3 Turbulence model screening

Turbulence modeling constitutes a critical aspect in the computational analysis of VAWTs. Achieving a computationally efficient, reliable, and precise approach that comprehensively covers the entire operational range of such fluid machinery is undeniably challenging. This complexity stems from the presence of attached and separated flow regions during the turbine's revolution, which are influenced by various factors, including (i) potential dynamic stall phenomena, (ii) diverse transition onset points, and (iii) temporally varying conditions. Addressing these intricacies and accurately capturing the fluid dynamics in VAWTs necessitates a well-designed turbulence modeling strategy. Furthermore, intricate and unstable vortical structures periodically manifest and intersect with the turbine blades.

In the preceding studies concerning an H-shaped VAWT with identical characteristics in terms of airfoil profile, swept area, and blade number, the employed turbulence model was the $k-\omega$ SST model. Additionally, the investigation took into account in particular the so-called low-Reynolds formulation of the $k-\omega$ SST model [92], a variant that has demonstrated notable efficacy, specifically in scenarios characterized by high TSRs. It is important to observe that, with the speed of revolution maintained constant across the entire operational range, a rise in the TSR results in a decrease in the freestream velocity, consequently leading to a reduction in the approaching Reynolds number. In the context of Troposkein VAWTs, a notable and fundamental aspect arises, setting it apart from H-type VAWTs, which is the substantial variation of the TSR along the span of the Troposkein VAWT blades. In contrast to H-type VAWTs, where the TSR maintains a relatively uniform value across the rotor span, troposkein VAWTs exhibit significant variations in TSR along the blade span. This particular characteristic poses a challenge when conducting analyses and simulations to understand the aerodynamic behavior of troposkein VAWTs comprehensively. Consequently, in-depth investigations are imperative to unravel the complexities and intricacies inherent in troposkein VAWT performance, particularly in relation to the influence of spanwise TSR variations on their overall aerodynamic performance. Regardless of the equatorial TSR value, a noteworthy observation emerges whereby, as one moves away from the equatorial section, there is a substantial reduction in the local TSR. This reduction consequently results in significant variations in the angles of attack on the airfoil and local Reynolds number along the span of the turbine blades. Concurrently, the local blade solidity experiences a substantial increase. These pronounced variations in TSR, angles of attack, Reynolds number, and blade solidity emphasize the complexity and non-uniform nature of the aerodynamic conditions prevailing along the span of the equatorial plane in such turbines. It

could be contended that the turbine sections located proximate to the midspan region are the primary conduits through which the majority of the mass flow rate passes, consequently resulting in the accumulation of the predominant driving torque.
Nevertheless, it is crucial to acknowledge that the drag induced by the low-Reynolds regions situated in the upper quartile sections of the rotor (below 25% and above 75% of the rotor's total span) can exert a significant influence on the turbine's overall performance. This observation is in agreement with the outcomes of recent BEM analyses conducted on the current turbine [82], particularly under conditions of high TSR.
The present study undertook a comprehensive investigation to evaluate turbulence modeling approaches. Specifically, both low-Reynolds $k-\omega$ SST model, along with the Spalart–Allmaras model, were considered in this screening process. The primary objective was to assess the performance of these turbulence models in the context of the considered wind turbine. A 2D campaign was conducted as part of this investigation, and the outcomes of this campaign have been presented in Figure 4.5. It shows a comparative analysis of the computed C_P using LR and SA on the medium grid, compared with experimental data. The complete results of the model screening for all the evaluated grids are presented in Table 4.1. An observation derived from these data indicates that, irrespective of the chosen turbulence model, the predicted performance levels exhibit higher proximity to each other around the peak efficiency condition compared to the situation at maximum TSR. Furthermore, the most substantial disparities in the obtained results, arising from the utilization of different turbulence models, are observed at lower TSRs. In fact, under these specified operational conditions, the flow exhibits increased unsteadiness, accompanied by elevated variations in the angle of attack and Reynolds number. The related flow field is distinguished by pronounced flow detachment, periodic re-attachments on solid walls, and vortex shedding from the airfoil. However, turbulence models based on eddy viscosity encounter a notable challenge when attempting to simulate these complex phenomena. For cases where the TSR values align with peak performance or surpass it, the aerodynamics of the blade exhibit decreased occurrence of flow separation, while attached flow conditions become more influential in determining overall turbine performance. As a result, the role of transition might play a more relevant role on turbine aerodynamics. Undoubtedly, this constitutes a crucial aspect in the current investigation, considering the maximum Reynolds number of approximately 2.10^5. Moreover, the blade surface exhibits a smooth configuration, and the incoming turbulence intensity is exceptionally low, standing at 0.1%, coherently with the reference experiments, performed in a controlled environment. The varying significance of aerodynamic characteristics across different operational conditions entails a notable impact on the predictive capacity of the model. Specifically, when employing the HR model, the calculations consistently exhibit a tendency to underestimate the turbine power coefficient, with this discrepancy being more pronounced at lower TSR. Moreover, it is well-established, and further supported by comparative BEM predictions [82], that the 3D outcomes yield efficiencies lower than those derived from the two-dimensional (2D) simulations. This observation raises concerns regarding the reliability of predictions obtained with the conventional SST model.
The LR model was proposed by Wilcox [92] with the aim of simulating the effects of natural transition. This involved the manipulation of model coefficients to postpone the inception of the turbulent boundary layer. As a consequence, the LR model effectively reproduces the enhancement of turbulent quantities within the boundary layer. Considering the aforementioned, it is evident that the LR model exhibits greater capability in replicating turbine aerodynamics, especially at high TSRs. Particularly, in this load condition, the LR model outperforms the SA turbulence model in terms of reproducing turbine performance. Conversely, the SA turbulence model appears to provide a more accurate description of turbine performance at low TSR, where the airfoils experience substantial separations and the relevance of transition may

be reduced. However, to gain a more comprehensive understanding of the model comparison, a thorough assessment through full 3D analyses is imperative, a subject that will be addressed in the subsequent section.

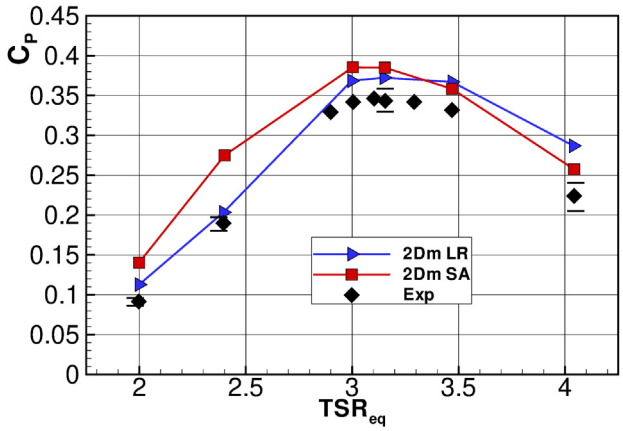

Figure 4.5: 2D power coefficient versus TSR_{eq}: experiments and CFD.

4.2 3D Results and Analysis

In this section, a comprehensive investigation is conducted to analyze the performance of the Troposkein turbine under examination, considering two different operating conditions, TSR_{eq}=4.0 and 3.1. The accuracy and reliability of the calculated results are assessed in relation to various key parameters, followed by a comparison with the experimental data.
The aerodynamic properties and operational effectiveness of the Troposkein VAWT are further examined using instantaneous and time-averaged flow fields derived from a dataset of 120 solution data fields that encompass the entire revolution. By adopting this extensive analytical approach, a thorough understanding of the Troposkein turbine's behavior is obtained, shedding light on its performance in both considered operating conditions.
The aerodynamics of a Troposkein rotor undoubtedly exhibit greater complexity in comparison to an H-shaped rotor, where the 3D aspects mainly arise from the presence of struts and finite blade effects. To comprehensively understand the flow field and rotor performance, as well as to accurately discuss their spanwise evolution, the turbine half-height was discretized into ten parallel slices. This division facilitates the distinct analysis of the forces and moments acting on each individual rotor slice. Moreover, this approach enables a direct and convenient comparison with low-fidelity engineering models, such as Blade Element Methods, which independently address the aerodynamic problem for each slice or section along the rotor's span. The ability to perform such comparisons enhances the understanding of the troposkein rotor's aerodynamic behavior and opens avenues for improved modeling and analysis techniques in the field of wind energy research.
The primary aim of this section is twofold. Firstly, it seeks to perform a comprehensive evaluation of the turbine's overall performance by conducting a comparative analysis between CFD predictions and data obtained from prior experimental studies. Secondly, the section aims to conduct a careful examination of the velocity and turbulence flow fields. The purpose of this examination is to acquire profound insights into the aerodynamic characteristics that define the

specific operating conditions under investigation.

4.2.1 Turbine's performance

Table 4.2 presents an all-encompassing summary of the predicted performance of the examined VAWT. To ensure a thorough analysis, it incorporates the three different turbulence models aforementioned; SA, LR and HR.

		TSR3.1	TSR4.0
3D-10Ms	HR	0.220	0.167
	LR	0.249	0.181
	SA	0.274	0.167
3D-32Ms	HR	0.257	0.186
	LR	0.276	0.202
	SA	0.296	0.181
Exp	-	0.345	0.220

Table 4.2: Power coefficient as a function of TSR_{eq} computed on different 3D grids, using different turbulence models, in comparison with measurements

However, the 3D HR simulations significantly underestimate the wind energy extraction of the turbine under both wind speed conditions (TSR_{eq}=3.1 & 4.0). This observation is in line with the expected results obtained from the two-dimensional simulations. In light of this outcome, going forward, the analysis is restricted to simulations performed with the LR and SA models. Figure 4.6 shows a comparison between the performance estimates, the 2D, 3D CFD, and experiments.

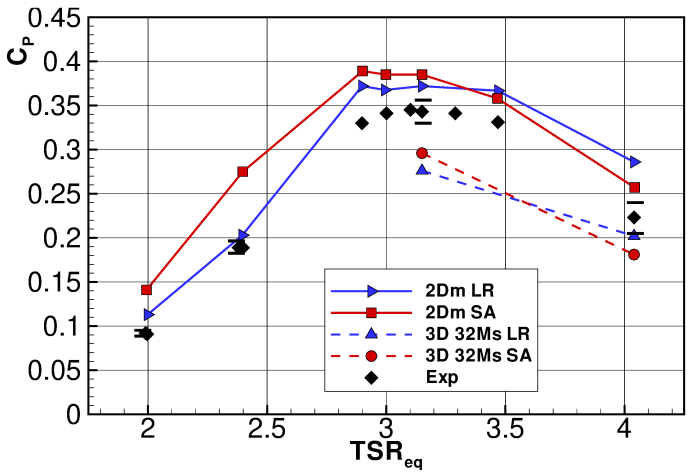

Figure 4.6: 2D and 3D power coefficient as a function of the TSR_{eq} computed on medium 2D grid and on 3D grids using LR and SA models in comparison with measurements

For the 3D case, it is evident that irrespective of the specific grid or model employed, the predicted performance level exhibits good alignment with the measured power coefficient at the higher TSR_{eq} (4.0) rather than at the condition of peak efficiency.
From a qualitative perspective, the 3D performance curve exhibits the expected reduction in

power coefficient due to the overall influence of three-dimensional losses and flow phenomena. However, the comparison among the models also reveals a distinguishable 'shift' of the curve towards higher tip-speed ratio (TSR) values. In the context of 2D simulations, a significant deviation in the predictive capability of the LR model is observed, as it underestimates the performance for TSR_{eq} values lower than 3.1. Interestingly, in the 3D case, a similar observation is made, but the estimated intersection point between the LR and SA curves shifts to a TSR_{eq} value of approximately 3.6. However, it can be observed that the LR model appears to be more appropriate than the SA model in the vicinity of the higher TSR_{eq} condition. Conversely, an opposite trend is observed near the condition of peak efficiency.
Presently, the focus is directed toward conducting a meticulous examination of the 3D analysis, specifically targeting both the peak condition and the higher load condition. These two distinct scenarios have a crucial role in acquiring a comprehensive understanding of the system's behavior and performance.

PEAK CONDITION: TSR_{eq}=3.1

The investigation focuses primarily on the peak power condition, which holds paramount significance during the turbine's operation. Figure 4.7 presents a comprehensive analysis of the rotor's overall performance by illustrating the spanwise evolution of the C_P coefficient for the chosen grids and models. As previously mentioned, the spanwise decomposition of the rotor aerodynamics aims to reveal the distinctive contributions of each radial section to the overall turbine performance, thereby highlighting the influence of the TSR variability along the blade span: Local TSR (see the top of Figure 4.7). It is noteworthy that the reference area employed in computing local performance pertains to the respective 'stream-tube' section, defined as the product of the average radius of the section and its corresponding height. The uniformity in the latter parameter across all sections is emphasized, wherein it equates to one-twentieth of the total turbine height.

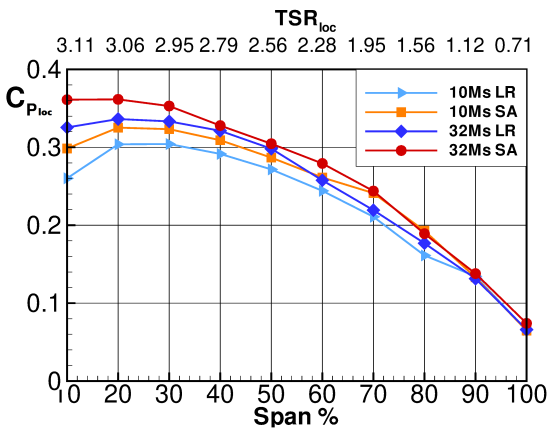

Figure 4.7: Power coefficient at different spanwise position, TSR_{eq}= 3.1

The trend demonstrates that there exist notable disparities in the C_P values anticipated by two models LR and SA. These differences are consistently observed across the entire span, with variations extending up to 80% of the characteristic length H*/2. Particularly noteworthy is the distinguishable discrepancy observed in the midspan region, where the SA model converges towards the two-dimensional prediction (0.35), while the LR model exhibits an underestimation

of the 2D value, displaying instead a localized decreasing trend. Notably, analogous outcomes are observed when employing a coarser grid comprising 10 million cells. The SA model's superior predictive performance compared to the LR outcome is to be expected, particularly due to the gradual decrease in TSR across the blade's span. This outcome well aligns with the previously discussed 2D findings. In addition, in the region where H*/2 exceeds 80%, concurrent with TSR declining below 1.5 and Reynolds number falling below 50000, notable separations occur, causing the models to exhibit similar behavior.

HIGH TSR CONDITION: TSR_{eq}=4.0

At TSR_{eq} = 4.0 (Figure 4.8), both the LR and SA models yield comparable results in both the equatorial section (up to 20% of H*/2) and the tip region (above 70% of H*/2). However, in the central region of the machine (between 30% and 60% of the H*/2), the LR model demonstrates a tendency to yield higher C_P values. This pattern is consistent even when employing a coarse mesh composed of 10 million elements. Progressing along the blade span, the rotor experiences a considerable decrease in tip speed ratio, resulting in the heightened significance of the initiation of detached flows. Especially, in the tip region of the rotor, where the tip speed ratio drops below 2 and the lowest Reynolds number descends below 100,000, leading to the triggering of a leading edge stall, both models exhibit nearly identical power extraction predictions.

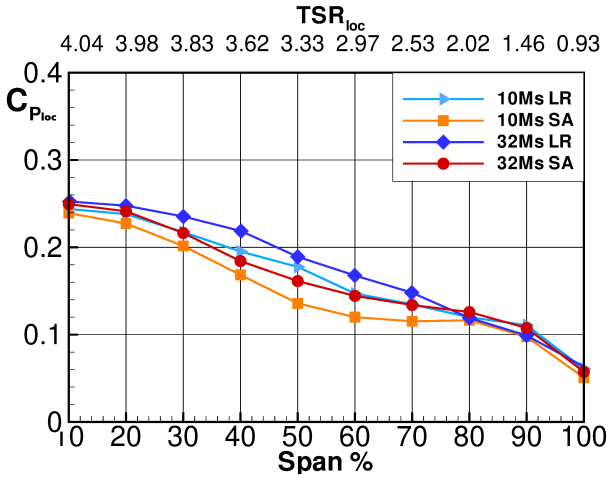

Figure 4.8: Power coefficient at different spanwise position, TSR_{eq}= 4.0

4.2.2 Turbine's wake

A profound comprehension of the turbine's behavior and operational mechanisms necessitates a thorough exploration of the turbine's wake. This task requires a thorough investigation that spans across computational techniques, intricately delving into the principles of flow physics. For each TSR condition, computations were performed to obtain the time-averaged wake (after reaching periodicity, and over one complete turbine revolution). Particular attention was directed towards investigating the near wake region, and these analyses were conducted with reliance on the available experimental data.
Figure 4.9 depicts the near wake profile at midspan, illustrating a comparison between the 2D and 3D calculations and the corresponding measured data at X/R_{eq}= 1.7 for the considered

operation conditions. Focusing on the 3D results, in the two cases, the implementation of the SA model yields satisfactory agreement with the measured velocity data. Conversely, the outcomes obtained through the utilization of the LR model manifest the most notable deviations from measurements on the leeward side. This discrepancy arises due to the substantial angles of attack encountered by the blade, prompting the detachment of vortices. Consequently, the wind stream experiences reduced work exchange, leading to a thinner wake and a diminished velocity deficit in the wake region. Although the LR model yields a C_P value that approaches the experimental datum at TSR_{eq}=4.0, it is noteworthy that the SA model provides superior predictive capabilities concerning the local wake profile. The streamwise velocity deficit in the wake plays a crucial role as an indicator of the mechanical energy extracted from the wind, essentially representing the amount that is efficiently harnessed at the shaft, dependent on fluid-dynamic efficiency. Nevertheless, the wake's evolution and recovery are intricately influenced by various other viscous and turbulent flow phenomena, which, in this context, are observed to be more effectively captured by the SA model rather than the LR model.

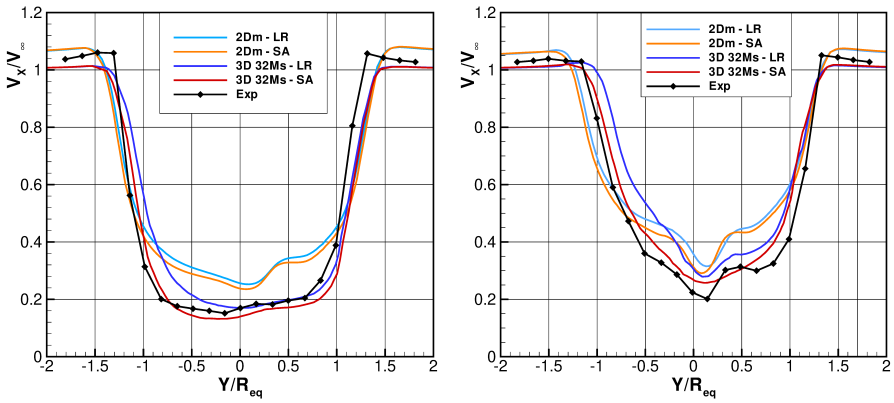

Figure 4.9: Wake profile (time-averaged), CFD and experiments: Streamwise velocity on symmetry plane at $\mathrm{X/R}_{eq}$ = 1.7 for TSR_{eq}=4.0, 3.1 (left, right)

The wake behavior displays consistent trends at different spanwise positions, as illustrated in Figure 4.10 for the near wake during peak efficiency conditions. Moreover, the velocity profiles derived from the SA model on the more refined 3D computational mesh demonstrate substantially better agreement with the experimental measurements.

Figure 4.11 depicts both experimental and computational wake profiles at the position $\mathrm{X/R}_{eq}$=1.7, for the peak operation condition. It should be noted that the experimental contours are based on measurements taken from the lower half of the turbine, specifically where the holding post is attached. In contrast, the computed field encompasses the upper half of the VAWT due to the impracticability of simulating the lower half, which would necessitate modeling the entire rotor. Despite this discrepancy arising from the different reference locations, the computed streamwise velocity deficit exhibits a noteworthy level of concurrence with experimental observations, manifesting consistent agreement in terms of both wake shape and width.

The elevated velocity region observed at the upper center of Figure 4.11 can be attributed to the existence of a downwash phenomenon, which is absent in the experiments due to the presence of the holding post and serves to re-energize the flow after crossing the turbine.

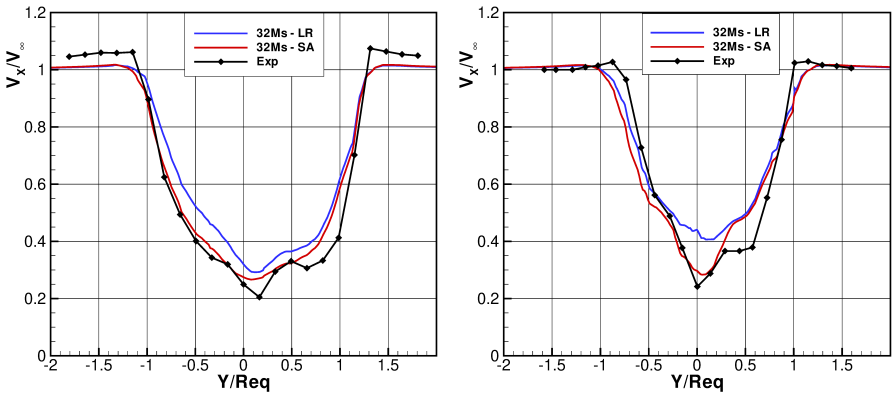

Figure 4.10: Wake profile (time-averaged), CFD and experiments: non dimensional streamwise velocity at selected Z/H* = positions 0.15 and 0.57, left/right, for 3D computations on 10Ms/32Ms grids at TSR_{eq}=3.1

4.2.3 Troposkein VAWT aerodynamics

The interaction between vortical structures and the solid blades holds indisputable significance in influencing the operational efficiency of the VAWT. Furthermore, the continuous development of vortices within and behind the turbine rotor introduces a notable level of intricacy into the fluid-dynamic characteristics of this specific machine type. In order to augment the explanations and interpretations previously offered, this section of the study presents instantaneous and time-averaged contours, computed over the last turbine revolution, following the attainment of periodicity. The contours refer to the 2Dm grid and the 32 million cells grid in 3D, employing the SA turbulence model unless stated otherwise. In particular, contour plots over a number of predefined planes that are aligned orthogonally to the cartesian coordinates are used to represent non-dimensional solution quantities. These chosen planes are Y/R_{eq}= 0.0 in the transverse direction, X/R_{eq}= 0, and X/R_{eq}= 0.5 in the streamwise direction.
In general, for high TSR values, the vortical structures exhibit relatively slow downstream convection (low flow speed). In contrast, at lower TSR values, in addition to the more rapid downstream convection of vortices, the flow around the blades can be affected by the occurrence of dynamic stall hysteresis cycles. Especially when dealing with high angles of attack (low TSR), the influence of dynamic stall hysteresis cycles becomes particularly pronounced.

Figure 4.13 represents a visualization of the streamwise velocity at TSR_{eq}=3.1 for both 2D and 3D cases, offering insights into the evolution of the wake behind the turbine rotor. It illustrates the expansion of the 2D wake with a wider angle, highlighting the absence of the mitigating influence contributed by the third dimension, which would otherwise attenuate the blockage effects. However, of particular interest is the observation that, notwithstanding the variations in wake characteristics, the C_P of the turbine in the equatorial section, as derived from the first slice of the 3D simulation, aligns closely with the value obtained from the 2D simulation (particularly concerning the SA model). This alignment suggests a substantial similarity in rotor aerodynamics between the two distinct simulation approaches. As both the 2D and 3D simulations were conducted without any unintended blockage effects arising from the domain extension, the dissimilarities observed in the downstream flow fields between the two cases are attributed to the distinct blockage characteristics inherent in the respective wakes. Specifically,

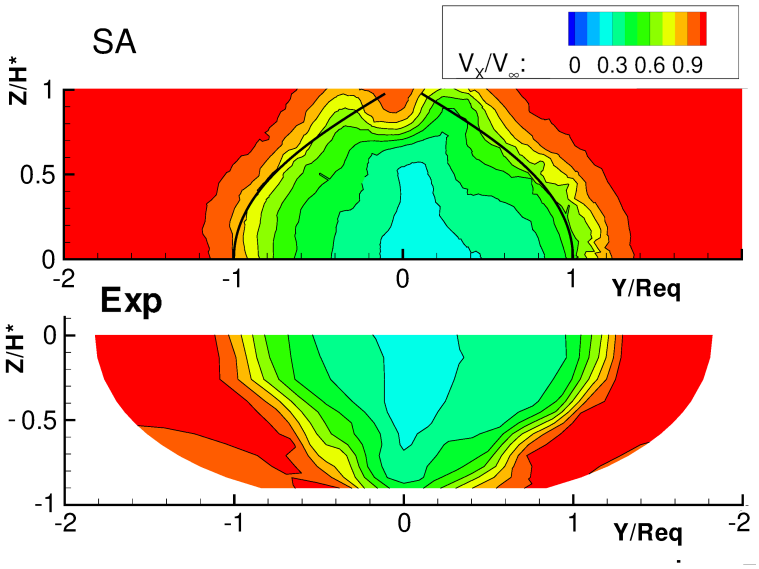

Figure 4.11: Wake at TSR_{eq}=3.1 on the 32Ms grid: measured and predicted streamwise (time-averaged) velocity on the flat surface X/R_{eq}=1.7.

the disparity can be attributed to the considerably larger blockage associated with the wake in the 2D equatorial model compared to the 3D troposkein model. The latter exhibits a spanwise reduction in wake extension, resulting in an overall lower wake blockage, thereby influencing the flow field, even at midspan. This constitutes a compelling aspect of troposkein rotors, necessitating the use of fully three-dimensional flow simulations to accurately predict the wake behavior, also in the equatorial section. At a precise azimuthal location, Figure 4.14 exhibits the instantaneous development of vortical structures downstream along the axial direction. These localized flow features yield notable influence on the energy harvesting process; however, their exhaustive analysis presents inherent complexities. To extract valuable insights from the flow field, the implementation of time-averaged flow fields has proven to be more beneficial, serving as a means to investigate the flow evolution as it interacts with the turbine. In this context, Figure 4.12 illustrates the streamwise and axial non-dimensional velocities at Y/R_{eq}=0. In close proximity to the top of the turbine, a geometrical obstruction arises at the junction between the blades and the holding post. This effect, in combination with blockage resulting from the substantial solidity of the structure, compels the flow to accelerate and bypass the rotor as if encountering a solid obstacle. The illustrated flow field distinctly exhibits the downwash phenomenon occurring downstream of the turbine shaft, as well as the re-energization of the tip wake flow within the domain characterized by negative axial velocity.

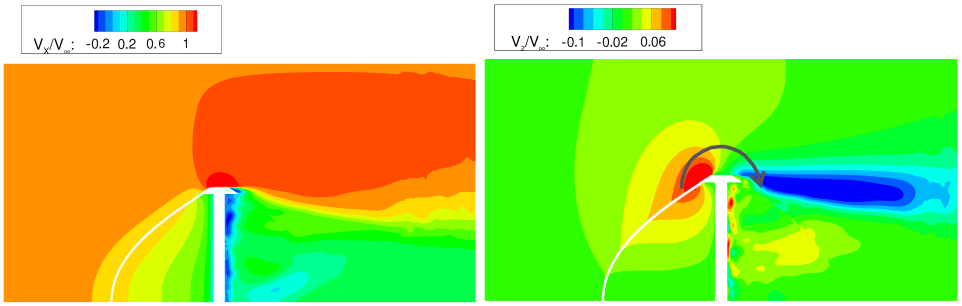

Figure 4.12: TSR_{eq}=3.1, time-averaged streamwise (left) and axial (right) velocity at $Y/R_{eq} = 0$.

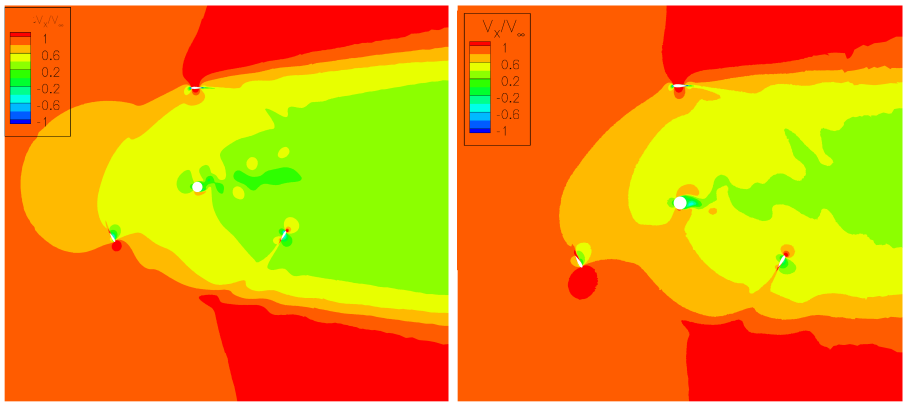

Figure 4.13: TSR_{eq}=3.1 istantaneous streamwise velocity of 2D (left) and 3D (right) computations on the equatorial plane

Figure 4.15 reveals the gradual rise in axial velocity towards the tip, influenced by the blade's lean. The particular blade shape redirects the incoming flow upward during the upwind part of the turbine revolution, while an opposing effect occurs during the downwind part of the revolution.
The aforementioned effects are notably more pronounced in the windward region, particularly due to the higher relative flow velocity compared to the leeward portion of the revolution, as in the upwind region the blade progresses against the wind. Furthermore, within the windward region, the fluid dynamics experience minimal perturbations, and there is an absence of significant vortex detachment phenomena. In the right frame of the figure, it is evident that, as one progresses downwind, the upward motion on both sides gradually tends to equalize after the X=0 point. This behavior is attributed to the more pronounced influence of the blade lean in the downwind-windward quadrant. The downwash near the mid-longitudinal plane (Y/R_{eq}=0) combines, at the blade tip, with this upward motion, leading to the emergence of two prominently counter-rotating vortices. These vortices are notably remarkable in the right frame of Figure 4.15.
Ultimately, it is distinguishable that the central region of the wake experiences a positive axial displacement due to the entrainment influence exerted by the local streamwise acceleration. The exhibition of spanwise motions gives rise to the formation of two counter-rotating vortices in

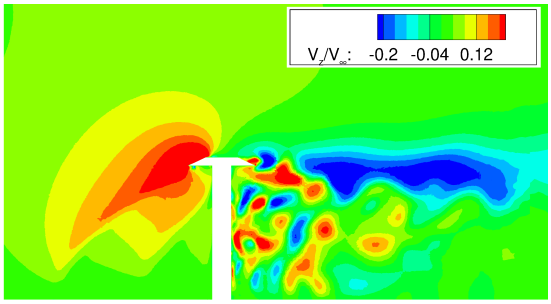

Figure 4.14: TSR_{eq}=3.1 istantaneous axial velocity at $Y/R_{eq} = 0$.

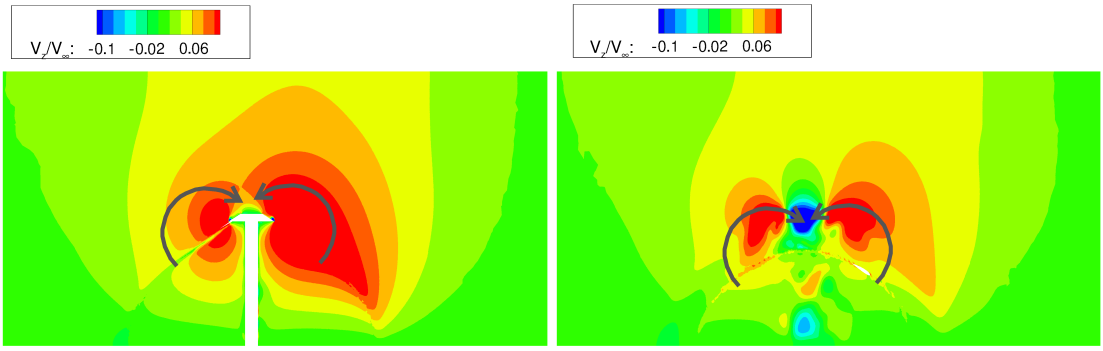

Figure 4.15: TSR_{eq}=3.1, time-averaged axial velocity at $X/R_{eq} = 0$ (left) and 0.5 (right).

the region proximate to the blade tip. Consequently, these vortices lead to the peculiar shape of the wake that is visually evident in Figure 4.11, in the proximity of the turbine tip. An emphasis must be placed on the noteworthy aspect that the aforementioned three-dimensional macroscopic characteristics persist at the TSR_{eq} of 4.0, although with a discernible reduction in their intensity.

4.3 Blade design: slanted vs plane

In the design of VAWTs, the configuration of the blades necessitates careful consideration of diverse factors encompassing aerodynamics, structural integrity, and manufacturing feasibility. The primary objective of this section's investigation centers on a comprehensive examination of the aerodynamics and operational performance of troposkein VAWT that exhibit distinct blade configurations. In the first case, the blade is created by simply bending one initially straight beam, producing a "slanted" blade, corresponding to the turbine mentioned in the earlier sections. In the second case, a 'plane' blade design is contemplated, wherein the NACA0021 profile is consistently applied along the rotor span, aligning with the troposkein stacking line. The slanted blade is distinguished by an airfoil profile that demonstrates a continuous variation in shape along its span when assessed in a plane perpendicular to the turbine axis. Notably, the blade's thickness gradually increases as it moves away from the midspan region. In light of

the current rotor configuration, the troposkein curve in the tip regions is characterized by an almost linear segment, displaying a slope of approximately 40 degrees. Consequently, this specific rotor design yields an airfoil maximum thickness, referenced in a horizontal plane, amounting to 32.5% of the chord length. On the other hand, the plane blade enables the maintenance of a consistent airfoil shape. However, achieving this airfoil shape requires a more intricate and costly manufacturing process. Figure 4.16 facilitates the observation and comparison of discrepancies between the slanted and plane blade configurations within a cross-sectional plane positioned equidistantly between the midspan and the turbine tip.
The fundamental objective of this analysis is to discern and compare the distinct behaviors exhibited by the two turbine configurations, with the ultimate aim of deriving essential design insights. Consequently, the principal focus does not lie in attaining the most precise estimation of the turbine's power coefficient. Rather, it is directed towards obtaining reliable indications of their relative capacity to efficiently harness wind energy. Within this context, the present section carefully investigates the disparities between the slanted-blade and plane-blade turbines, placing particular emphasis on the variations observed along the span, given that the equatorial section remains identical for both machines, by considering the 10 million mesh.

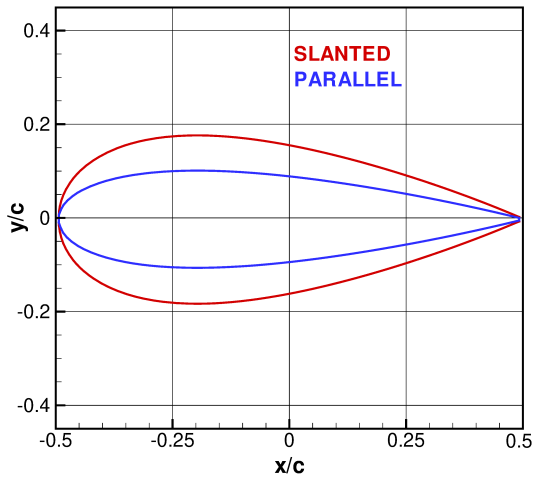

Figure 4.16: Airfoil section profile at Z/H* = 0.5 for the slanted and parallel design.

Figure 4.17 provides a comprehensive summary of the spanwise progression of the power coefficient (referred to as the 'local' coefficient) for both turbine configurations. Additionally, it presents the cumulative distributions of this parameter, wherein the cumulative value corresponds to the total power coefficient harnessed by the rotor when it reaches 100%. Exclusively reported the outcomes derived from the employment of the SA turbulence model, while it is noteworthy to mention that the LR model exhibits analogous patterns, albeit not explicitly displayed herein.

Within the left frame of Figure 4.17, the findings at TSR_{eq}=4.0 are presented, illustrating the superiority of the plane-blade design over the slanted-blade design within the range of 20% to 70% of the turbine half span. However, it is worth noting that a significant shift in trends becomes evident as one approaches the blade tip (over 70%). The observed behavior can be attributed to variations in the range of angles of attack and blade solidity encountered by the incoming relative flow.
As previously mentioned, the progression toward the rotor tip induces a reduction in the local

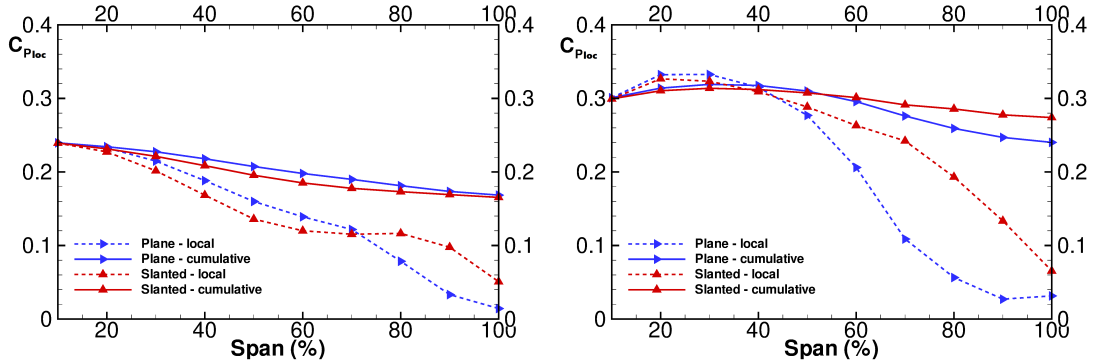

Figure 4.17: Local and cumulative C_P along the span for the slanted and plane configuration computed on the 10Ms grid (SA model) - TSR_{eq}=4.0 (left)/ TSR_{eq}=3.1 (right)

TSR, leading to significant variability of the angle of attack on the airfoil. This is complemented by a decrease in the Reynolds number and a rise in the blade solidity, further influencing the observed behavior. Consequently, the airfoil undergoes a cyclical deep-stall regime, accompanied by pronounced flow separations within the flow field. Under such circumstances, a thicker airfoil configuration holds the promise of exhibiting improved performance relative to a slender counterpart. As a result, this favors the slanted-blade turbine over the plane-blade turbine in the region near the tip. Conversely, under conditions where the dynamic stall of the airfoil does not occur, a contrasting scenario unfolds. It is a widely acknowledged phenomenon that, when operating at angle of attacks below the steady-state stall limit, a thinner airfoil configuration exhibits heightened lift and superior aerodynamic efficiency. However, within the dynamic stall range, the performance of the thinner airfoil will tend to deteriorate more significantly.
Nevertheless, when examining the global C_P, notable disparities between the two configurations are absent, revealing only a marginal advantage (less than 1% point) in favor of the plane-blade rotor. Consequently, these findings highlight a significant level of comparability or equivalence between the two machines in this flow condition.
Analogous observations are applicable to the computed C_P distributions at TSR_{eq}=3.1, as depicted in the right side of Figure 4.17. As the local TSR is uniformly diminished compared to the TSR_{eq}=4.0 condition, herein, beyond Z/H*= 0.4 the plane-blade rotor exhibits a clear decrement in its performance. However, it is noteworthy that the performance levels of the two configurations remain almost equivalent for lower spanwise positions (<40%).
In the region corresponding to the upper part of the troposkein profile, a clear and notable superiority of the slanted-blade design becomes apparent, resulting in a substantial 4% improvement in the global coefficient of power. This observation suggests that, for the particular rotor under investigation, the implementation of a slanted-blade turbine offers several advantages, including simplified manufacturing processes, improved structural robustness (thicker blades near the tip), and elevated aerodynamic performance during peak efficiency conditions. Nevertheless, it is necessary to acknowledge that at high TSR, both configurations exhibit identical performance.
In order to complement the analysis of the aforementioned quantitative outcomes, Figure 4.18 presents instantaneous snapshots of the flow field and vortical structures linked to the two rotor configurations. The visual representation encompasses distinct frames, wherein the left frames correspond to the slanted-blade, and the right frames pertain to the plane-blade counterpart.
The upper and central frames of Figure 4.18 showcase the streamwise velocity at X/R_{eq}= 0.

These visual representations serve to illustrate the significantly larger resistive cross-section associated with the slanted-blade configuration in comparison to the plane-blade design. Consequently, this observation relieves notable concerns on the structural integrity of the rotor in the case of the slanted-blade turbine. Nevertheless, when considering aerodynamics, the perspectives provided in the central part of Figure 4.18 emphasize the heightened efficacy of the slanted-blade configuration in adeptly handling the elevated angle of attack encountered in the tip region. In contrast, the plane-blade design displays discernible flow separation, an aspect absent in the slanted configuration. Such flow separation plays a key role in significantly influencing the generation and detachment of vortices within the wake of the turbine. In the lower section of Figure 4.18, flow velocity profiles are presented at planes situated at Z*= 87%. These visualizations clearly reveal wider regions of flow detachment and more pronounced vortical structures within the context of the plane-blade rotor. As a result, a more extensive wake velocity deficit is observed. It is crucial to highlight that this augmented wake velocity deficit cannot be attributed to an increase in work exchange but is primarily linked to the prevalence of intensified dissipative phenomena.
Similar characteristics are evident during another phase of the period, wherein the blades are rotated by 90 degrees in comparison to the previous azimuthal position, as visually depicted in Figure 4.19. This observation reinforces the consistent advantage of the slanted-blade rotor over the plane-blade counterpart throughout the entire rotational revolution process.

In order to gain deeper insights into the intricate flow field within and behind the rotor, Figure 4.20 presents the instantaneous helicity contours of calculations conducted at TSR_{eq}=3.1 for the examined designs. Two frames are depicted, each representing the helicity distributions on two orthogonal planes: an x-y plane at Z*= 50% to illustrate the two-dimensional vortical structures detached by the airfoils and an x-z plane at Y/R_{eq}=-0.3 to accentuate the three-dimensional nature of the flow. These visualizations unveil noteworthy disparities between the two designs. Due to the slender airfoil employed in the plane-blade rotor, the vortices detached by this configuration exhibit higher magnitudes and experience slower decay rates in comparison to those detached by the slanted-blade rotor. This difference is particularly discernible on the X-Z plane, which intersects the blade in the region where a more substantial flow separation occurs (as previously observed while discussing the central-right frame of Figure 4.18). Particularly, the employment of a plane blade engenders enhanced flow separation, giving rise to fully three-dimensional vortex structures that stem from the rotor and significantly contribute to augmenting the wake velocity deficit and retarding the recovery process of the wake.

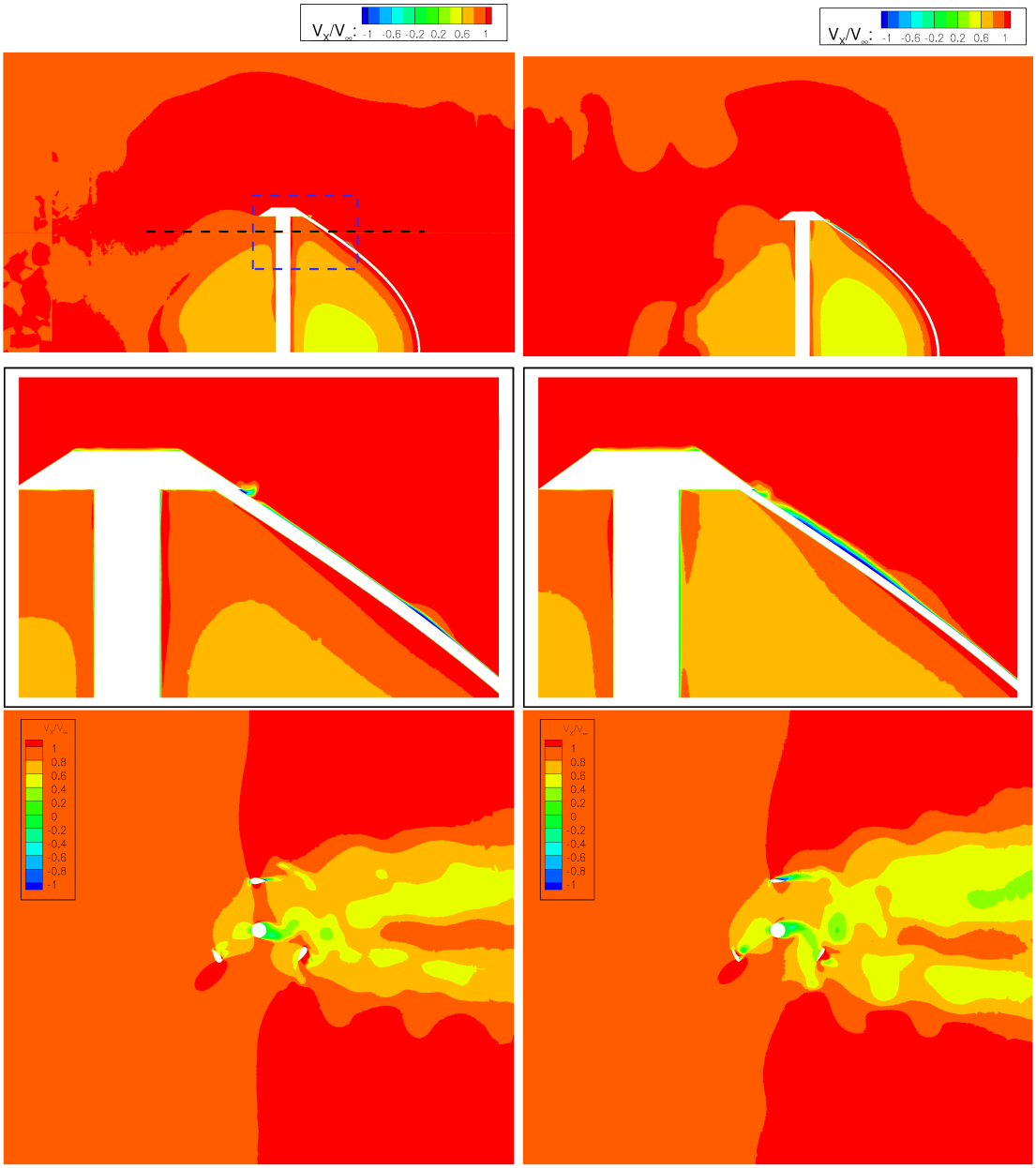

Figure 4.18: TSR_{eq}=3.1, non-dimensional streamwise velocity at azimuthal positions $\theta = 0°$ for the slanted/plane design (left/right): contours at $x/R_{eq} = 0$ in the top and bottom region of the figure and at selected spanwise position $Z^* = 87\%$ (indicated by black dashed line) at the bottom one.

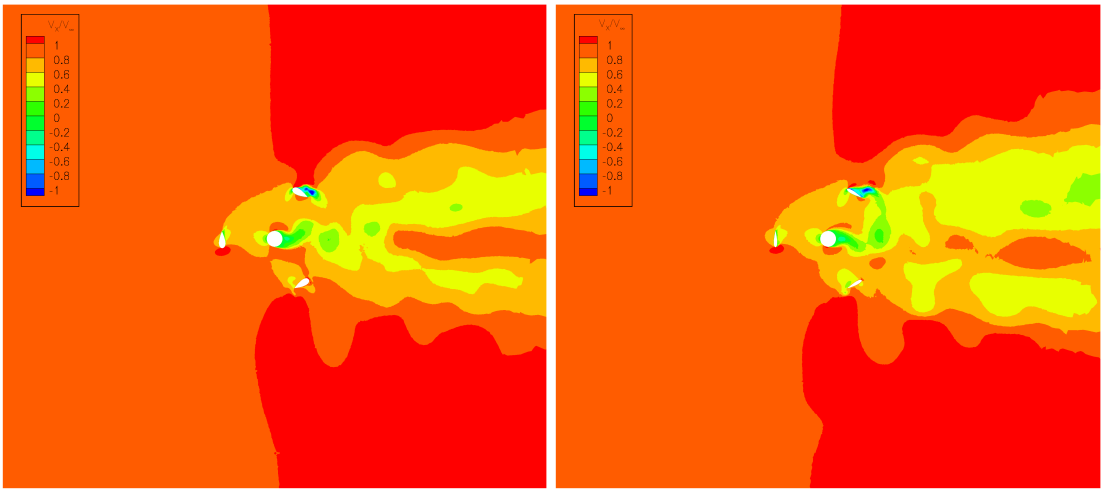

Figure 4.19: TSR_{eq}=3.1, non-dimensional streamwise velocity at azimuthal positions $\theta = 90°$ for the slanted/plane design (left/right): contours at $x/R_{eq} = 0$ in the top region of the figure and at selected spanwise position $Z^* = 87\%$ at the bottom one.

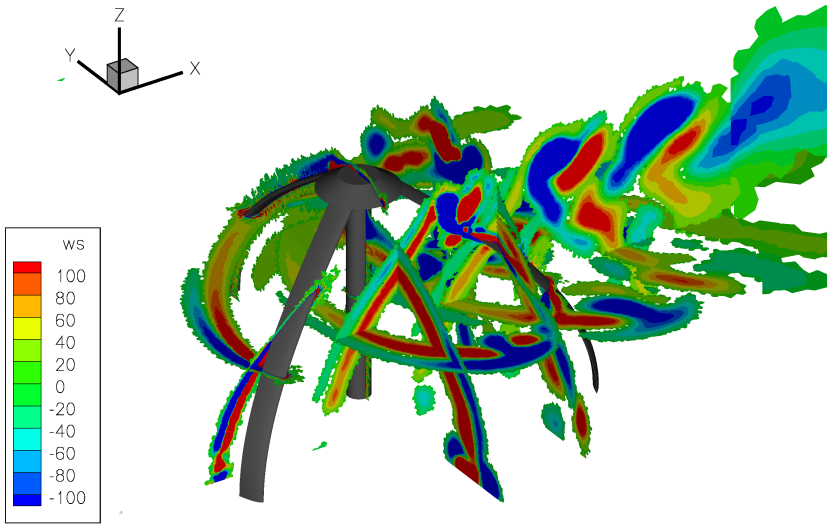

Figure 4.20: TSR_{eq}=3.1, helicity contours - 10Ms grid)

Chapter 5

Case 2: DeepWind demonstrator

5.1 Case of Study

During the advancement of the DeepWind project, a variety of comprehensive studies were conducted to evaluate the performance of the DeepWind VAWT concept and to establish whether it could be feasibly applied in floating offshore installations [17, 19, 20, 70]. Pertaining to this context, a 1 kW prototype of tree fiberglass blades was the subject of experimental investigations conducted in the Politecnico di Milano wind tunnel, with an open configuration, that allows real-scale measurements of micro wind turbines, see Figure 5.1. The experimental setup was carefully designed to accurately evaluate the aerodynamic performance of the DeepWind demonstrator in various scenarios. The covered changes in wind speeds, angular velocities of the rotor, and skewed flow operation. The primary geometric characteristics of the DeepWind demonstrator can be found in Table 5.1; Additional data, quoted drawings, and the cylindrical coordinates of the rotor are available in [17].

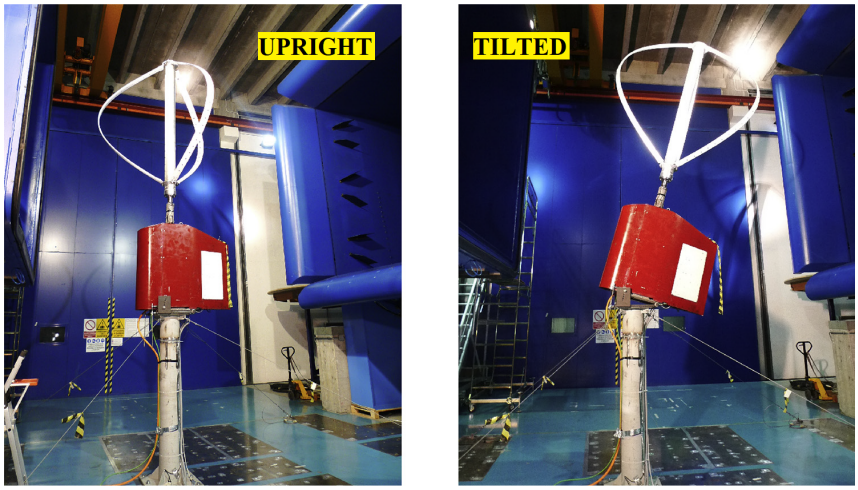

Figure 5.1: Side view of the Politecnico di Milano open chamber, showing both upright (left) and tilted (right) operating conditions [17].

Blade profile	DU-06-W200
R_{eq} [m]	1.1014
swept area [m^2]	2.63
chord [m]	0.101
rotational speed [rpm]	300

Table 5.1: Model VAWT test cases: main geometrical parameters

This chapter presents a thorough numerical investigation to gain insight into the performance of Deepwind concept with a comparison against available experimental data. The study is related both to the upright and tilted conditions. The adopted numerical settings are thoroughly described and the turbulence modeling is also preliminary considered. 2D and 3D computations are carried out in the upright state to allow reasoning on the capability prediction of the selected discretization schemes. The results' reliability is assessed by considering the integral power coefficient that allows performing an early quantification of the turbine performance. A more detailed evaluation of the energy harvesting level is obtained in a pointwise manner by computing the near wake field. The capability of the turbine to extract energy is also discussed as a function of the spanwise position to better capture the local flow field behavior. Furthermore, considerations on the near wake recovery, helpful to define a favorable installation of the wind farm, are also proposed. The study also provides some indications on the limitations of the scaled rotor model, not matching the Reynolds number of the full-scale model. A sensitivity investigation is presented, relying upon preliminary 2D computations, in order to discuss the numerical set-up adopted in terms of boundary extension, grid coarseness, and modeling approach. Afterward, a full 3D URANS set of computations is presented to investigate the performance and the vortical structure development of the tilted VAWT, in comparison to upright condition, also in view of future experimental data collected possibly at off-design for a full-scale mode.

5.1.1 Computational settings

The discretization and modeling settings adhere to the guidelines detailed in the prior case study, with the most relevant issues expounded upon within this section. A second-order accurate discretization approach is used for the URANS governing equations, assuming the ideal equation of state for perfect gases and incompressible flow. The momentum and pressure correction equations were solved using a pressure-based coupled algorithm, whilst the turbulence model equations were solved using a decoupled approach. An algebraic multigrid solver with relative residuals as low as 10^{-5} is used to solve the linear discrete system. An ad-hoc sensitivity analysis is used to determine the discrete space and temporal steps, after achieving periodicity, subsequent revolutions were examined. The objective of this analysis is to determine a discretization step size that is sufficiently small to ensure independence from the time step. An assessment of the relative error on the C_P coefficient, computed over consecutive revolutions, was carried out until a value below 1% was achieved. It has been demonstrated that a time step size of 0.5 degrees can be appropriate in terms of accuracy while remaining reasonable in terms of computational cost (in accordance with [37, 38]). The turbulent flow fields have been simulated by employing the Boussinesq approximation and utilizing both one-equation and two-equation models. The $k-\omega$ SST two-equations model, in its Low Reynolds version, has been adopted. This specific model integrates customized modifications suggested by Wilcox [92] to effectively address natural transition modeling. A comparison between this model and the one-equation Spalart-Allmaras model has been conducted to comprehensively evaluate the modeling influence across the entire TSR operating range (2D). Finally, it is essential to define suitable boundary conditions: ini-

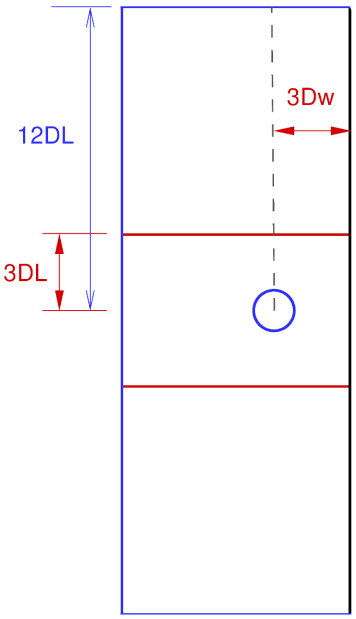

Figure 5.2: 2D and 3D domain extension at equatorial section domain extension (2D blue and 3D red);

tially, aligning them with the experimental configuration, and subsequently, establishing a proper extension of the computational domain. At the inlet boundary surfaces, conditions representing the free stream flow were applied, encompassing values for velocity, turbulence intensity, and the ratio of turbulent viscosity. These conditions were defined using the controlled parameters from the reference experiments and harmonized with the limitations set by the chosen turbulence models. At the outlet and lateral boundaries, a pressure outlet condition was implemented. In situations involving reverse flow, a low-turbulence atmospheric uniform flow was employed. Solid walls were subject to a no-slip condition. For the upright rotor, the symmetry condition was applied to the equatorial plane, whereas the no-slip wall condition was chosen to replicate the ground effect during tilted operation.

5.1.2 Mesh Sensitivity analysis

A sensitivity analysis was conducted to select the appropriate discrete domain approximation for both the 2D and 3D scenarios. The different blockage effects, as discussed in the previous case, see also [38], result in different domain extensions for the approximations in two and three dimensions. The final 2D domain encompassed a lateral span equivalent to twelve diameters, coupled with a downstream extension of three diameters, as illustrated in Figure 5.2. Conversely, in the case of the three-dimensional simulations, an identical domain was utilized, albeit with the modification that the lateral boundaries were positioned at a distance of three diameters from the central axis. This configuration is illustrated by the red lines in Figure 5.2. These outcomes have been yielded through a series of simulations that utilized progressively larger domains.

Figure 5.3 presents, on the left-hand side, the 2D torque coefficient which was performed using a lateral extension domain that spans up to 15 rotor diameters away from the central

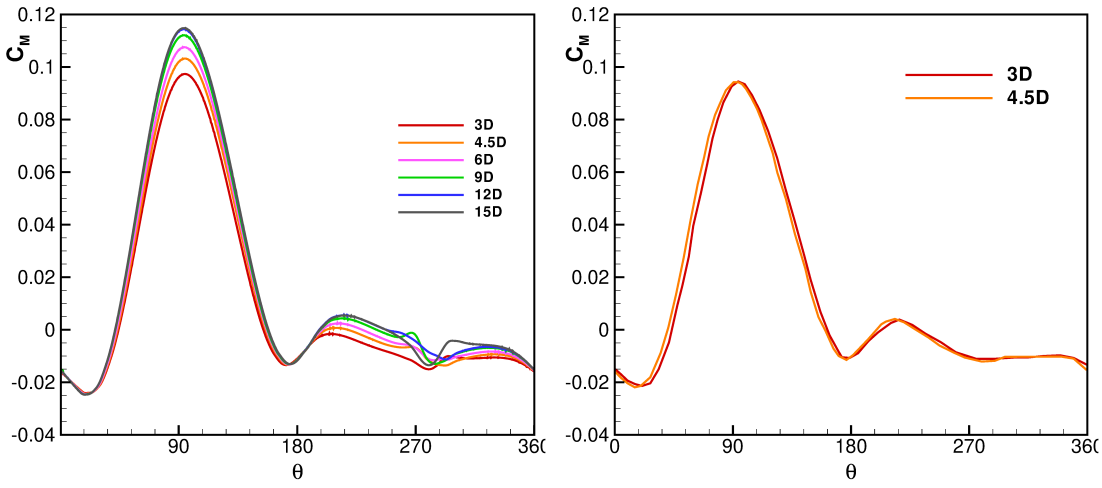

Figure 5.3: 2D/3D moment coefficient at $\mathrm{TSR}_{eq} = 4.55$ using the LR model, for varying lateral domain extension from 3D up to 15D (2D) and 3D, 4.5D (3D).

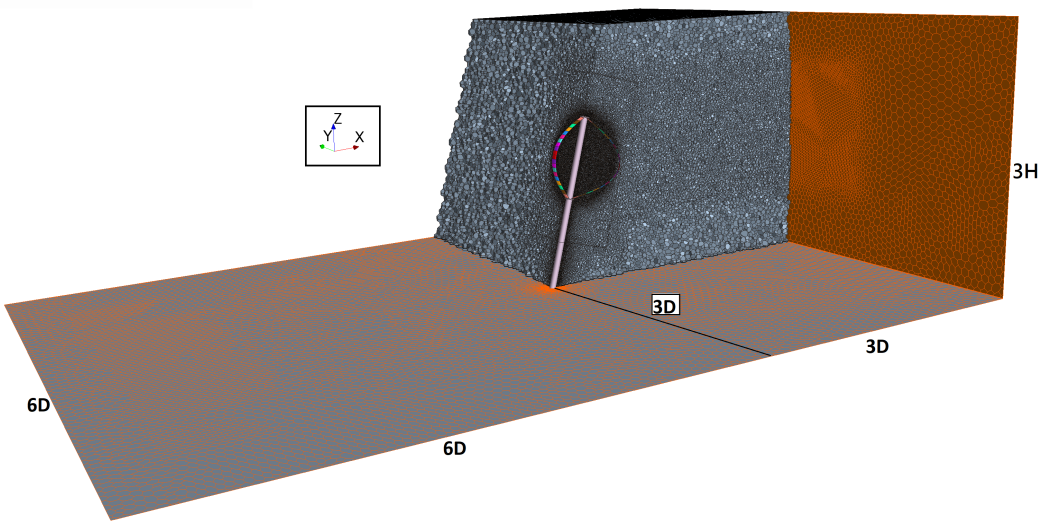

Figure 5.4: 3D computational domain extension.

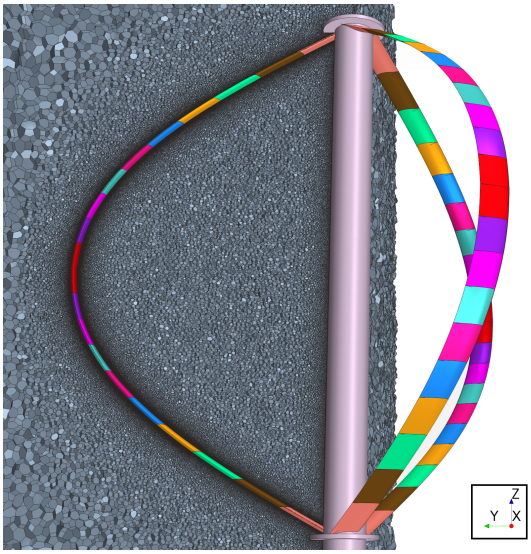

Figure 5.5: 3D computational grid details and spanwise slices along the turbine blades.

shaft. Instead, the right part of the same figure illustrates the discrepancy in the aforementioned parameter when employing lateral extensions of 3D or 4.5D in the context of the 3D computations. Hence, the lateral domain extensions of 12 diameters and 3 diameters are chosen as the definitive configurations for the 2D and 3D scenarios, respectively. As already reported the difference between these two selections is closely tied to the distinct blockage effects that take place.

Following the guidelines aforementioned (reported also in [38]), in the case of the upright operational scenario, the extent across the spanwise direction is two times the height of the half turbine model, while applying a symmetry boundary condition at the equatorial section. This selection is feasible due to the symmetry in the geometry and inflow conditions surrounding the equatorial section. This choice could be impeded solely by pronounced aerodynamic instability, which could arise in situations where the rotor is completely stalled (potentially at extremely low TSR values). Instead, for the 15-degree tilted configuration, due to the absence of symmetry, the complete model is taken into account, spanning a distance equivalent to one height of the VAWT ($\approx$ 10 chords) both over and under the turbine, see Figure 5.4.
Subsequent to that, an analysis of grid coarseness was conducted for the 2D equatorial mesh. The aim was to determine a suitable trade-off between the desired level of accuracy and the computational CPU cost. The characteristic spacing of the first cells adjacent to solid walls was established to ensure a y^+ value of approximately one, along with appropriate clustering in proximity to the wall. In accordance with the previous case, a 2D computational grid comprising approximately 125k polyhedral elements was constructed. Moreover, a sensitivity analysis of the mesh was performed on the 3D half-model case. The purpose was to address any potential concerns regarding the level of grid coarseness in the three-dimensional domain and to ensure the attainment of grid independence. Initially, a mesh containing 17 million elements was utilized, and subsequently, a comparison was made with a second mesh featuring 34 million elements (a detailed view is illustrated in Figure 5.5). For the peak power condition, the C_P value experienced a very small variation, rising from 0.280 to 0.284, indicating a negligible increase of less than

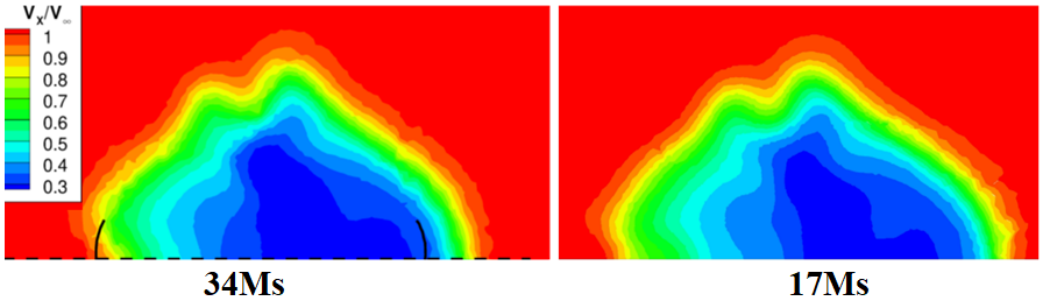

Figure 5.6: TSR_{eq}=3.54: Averaged non-dimensional streamwise velocity at $X/R = 1.5$.

2%. Furthermore, the comparison between non-dimensional streamwise velocity profiles in the near wake ($X/R = 1.5$) for the aforementioned two meshes, as illustrated in Figure 5.6, closely resembles one another. As a result, for the complete model operating under tilted conditions, a grid comprising 34 million elements was chosen.

5.1.3 Early performance prediction

In this section, a collection of results for both two- and three-dimensional cases is provided. These results enhance the understanding of the equatorial flow field, spanning the complete operational range of the TSR_{eq}. Figure 5.7 illustrates the 2D computed power coefficient spanning the considered tip speed ratio range, in comparison with selected 3D results, at peak power condition (TSR_{eq}=3.54) and at high load (TSR_{eq}=4.55).

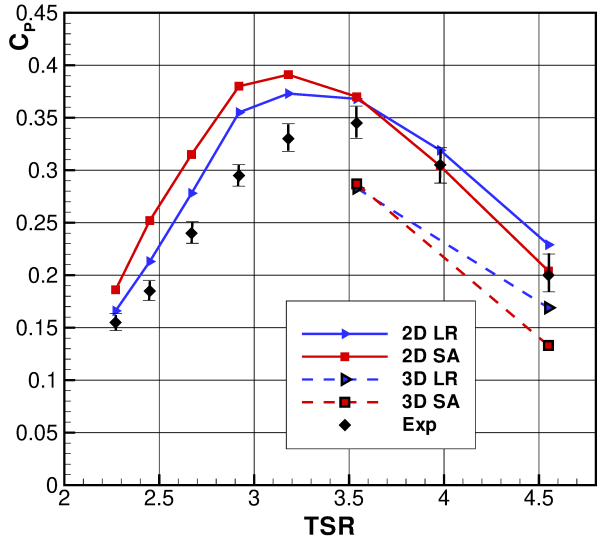

Figure 5.7: 2D and 3D power coefficient as a function of the TSR_{eq}: computed on 2D and 3D grids using LR and SA models in comparison with measurements.

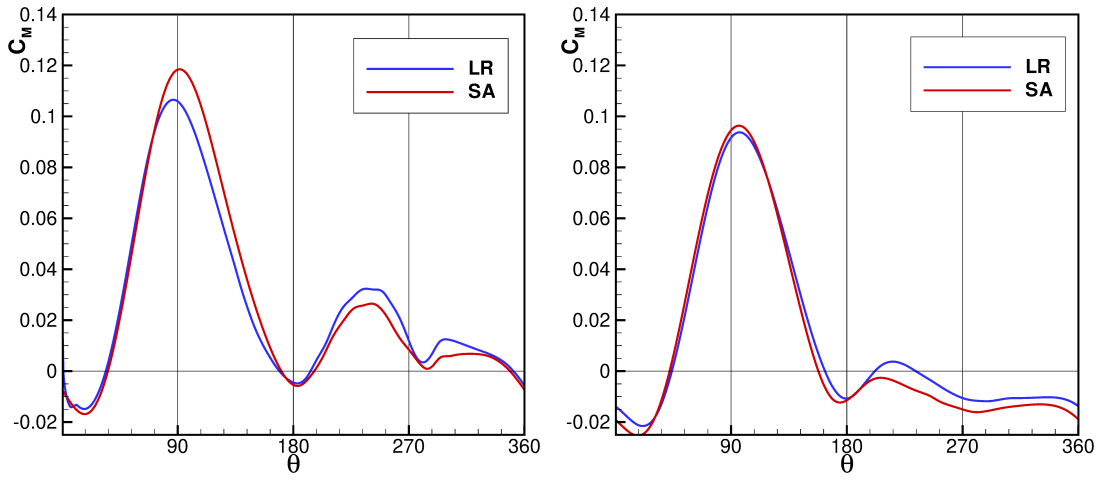

Figure 5.8: 3D moment coefficient as a function of the azimuthal angle for one blade, computed at $\mathrm{TSR}_{eq} = 3.54/4.55$ using the LR and SA models (left/right)

The obtained numerical results can be readily compared with available experimental values. The trends observed are in good agreement with the outcomes already presented in the previous chapter. For high TSR operating conditions, the LR version of the $k-\omega$ SST model demonstrates enhanced capabilities in handling aerodynamic characteristics influenced by transitional regime flows, thereby, establishing its major suitability for modeling turbine behavior compared to the SA model. The LR model consistently yields higher C_P values across the range from peak power to maximum TSR values than the SA model. Instead, the SA model demonstrates better behavior from low TSR value to peak condition, mainly owing to its capacity to slightly delay the onset of stall. Further comparison between LR and SA results when performing 3D computations is provided in Figure 5.8. From peak power point towards higher TSR values, upwind and downwind regions highlight slightly different sensitivity to the model, probably related to the blade aerodynamics, increasingly less affected by large-scale separations. In the presence of attached flow conditions, the transition might play a major role in turbine aerodynamics.
Additionally, relative to the preceding case, it is discerned that the Reynolds number within this context experiences a slight increase (180k vs. 120k for the Troposkein). This disparity undoubtedly exerts an influence on the dynamics of the turbulence model.
Based on these results, subsequent calculations aimed at investigating the behavior of the laboratory DeepWind model, both in the upright and tilted configuration, will be exclusively based on the LR $k-\omega$ SST model.

5.2 3D computations of the DeepWind demonstrator

This section delves into an investigation of the upright and tilted operational condition of the Deepwind laboratory model, employing the 3D simulations, and examining the results in correspondence with existing experimental data. Initially, the focus is directed towards the upright configuration. The 3D analysis encompasses two distinct operational points. The first pertains to the peak power point, characterized by a TSR_{eq} of 3.54 and a free-stream velocity, $v\infty$, of 9 m/s. The second operational point involves an off-design scenario with a high TSR value of 4.55, corresponding to a free-stream velocity of 7 m/s. Subsequently, the peak power condition has been also selected to discuss the tilt effect, considering an inclination angle of 15 degrees. Notably, the evolution of vortical structures exhibits distinct behavior both within the rotor and within its wake, generating intricate interactions between flow eddies and solid walls. Given the foremost significance of the peak power operation, a thorough analysis is undertaken, encompassing comprehensive evaluation through global integral coefficients as well as close inspection of localized flow attributes.
Figure 5.9 presents the experimental power coefficients [17], in comparison with the results obtained through CFD computations. It indicates two significant trends: i) an underestimation of integral parameters by the simulations in comparison to the experimental data, and ii) a noticeable decline in performance when dealing with the skewed configuration.

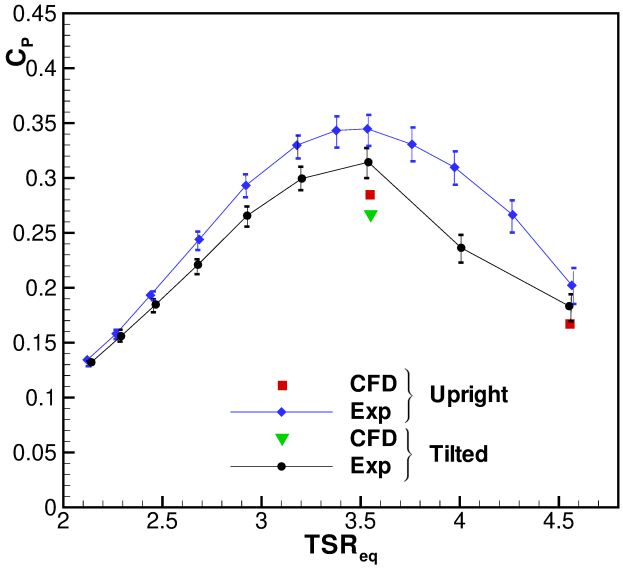

Figure 5.9: Upright and 15deg tilted power coefficient: Experimental [17] vs 3D CFD results.

To further evaluate the agreement between numerical simulations and experimental results, the computed near-wake field in the upright position is illustrated in Figure 5.10 (left-hand side), compared with the corresponding velocity distribution observed in experiments. A close alignment is evident between the two non-dimensional streamwise velocity mappings, both in terms of their shape and the magnitude of velocity deficit. It is noteworthy to mention that the available experimental results pertain to the lower half of the VAWT, whereas the numerical results correspond to the upper half.

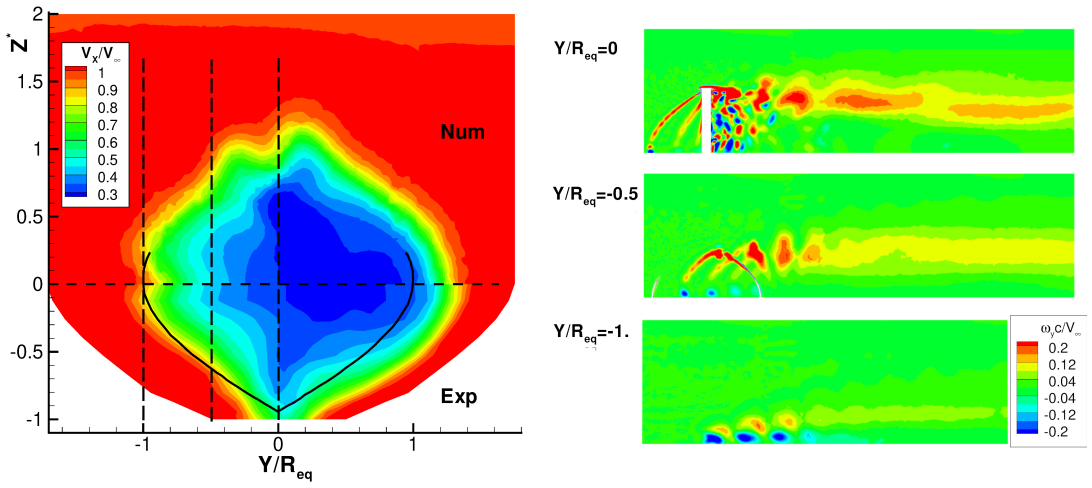

Figure 5.10: 3D computations at TSR$_{eq}$=3.54: Time-mean non-dimensional streamwise velocity on the near wake at X/R$_{eq}$= 1.5: CFD vs experiments (top left) – non dimensional vorticity on the RHS, from top for the shaft section Y/R$_{eq}$=0, till Y/R$_{eq}$=0 at the bottom

Analyzing the numerical outcome, it becomes evident that a distinctive decrease in velocity is observed at the upper section, specifically on the leeward side, which is attributed to counter-rotating vortices formed at the tip, resulting in an augmentation of the velocity ($Z^* \approx 1$ and $Y/R_{eq} \approx 0$). This feature is notably absent from the experimental map, as the map pertains to the lower half of the turbine, which is also influenced by the supporting post. Despite the presence of this feature, the calculated velocity field is in good agreement with the reference experimental field. Noteworthy is the occurrence of iso-lines wrinkling near the midspan of the turbine, specifically within the leeward zone situated between the juncture of the upwind and downwind regions ($Y/R_{eq} = -1$). In fact, within this area, there is a notable rise in local velocity primarily attributed to the formation of vortical structures. These structures are clearly illustrated in the pictures on the RHS of Figure 5.10. This representation displays the dimensionless lateral vorticity across the XZ cross-section that intersects both the shaft ($Y/R_{eq} = 0$) and the rotor within the leeward region. The downwind part of the flow field is distinguished by diminished energy content and numerous vortical structures, which interact with the rotor blades and give rise to spanwise flow variations as shown by the vorticity contours.

Additional insights into the velocity deficit within the near wake, across various spanwise positions, are provided by Figure 5.11. This figure illustrates the near wake at different spanwise positions. Satisfactory agreement is observed near the midspan, with a notable increase in wake size and enhanced energy harvesting projected for locations above $Z^* > 0.5$ where the machine sections are experiencing more complex aerodynamic configurations. However, at high load condition (TSR$_{eq}$=4.55), increased blockage effects are expected as displayed in Figure 5.12, where the near wake contours and velocity profile at midspan present the larger and steep velocity defect affecting this operating condition. Moving from midspan to the top region, alterations in the spanwise flow field, reduced TSR, and intricate vortical structures notably determine a different energy harvesting capability. Examining Figure 5.13, illustrating the specific C_P values for the slices indicated in Figure 5.5 from midspan to top, reveals that under peak power condition (TSR$_{eq}$=3.54), a monotonically variation in local C_P values is evident. Conversely,

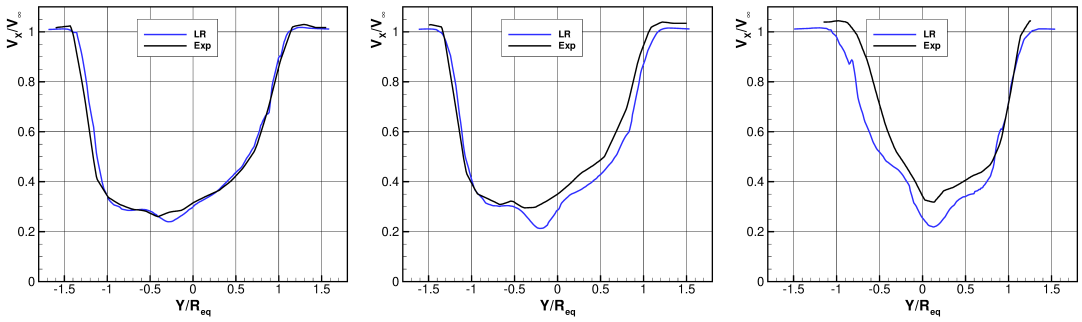

Figure 5.11: 3D computations at TSR_{eq}=3.54: Time-mean non-dimensional streamwise velocity at Z^*=0.13, 0.27, 0.50 (left, middle, right)

for off-design condition (TSR_{eq}=4.55), the local C_P exhibits an unusual trend with a minimum near the 60% span position relative to the midspan. Such a reduction, observed between 40 – 60% (see Figure 5.13 - left) is related to different aerodynamic behavior as suggested by the velocity maps reported in Figure 5.14, showing the lower energy content at high TSR (more braking effect). However, the performance decrease in the off-design condition can be attributed to reduced energy harvesting not only in the favorable upwind region but also in the downwind portion, as illustrated in the depicted Figure 5.14.

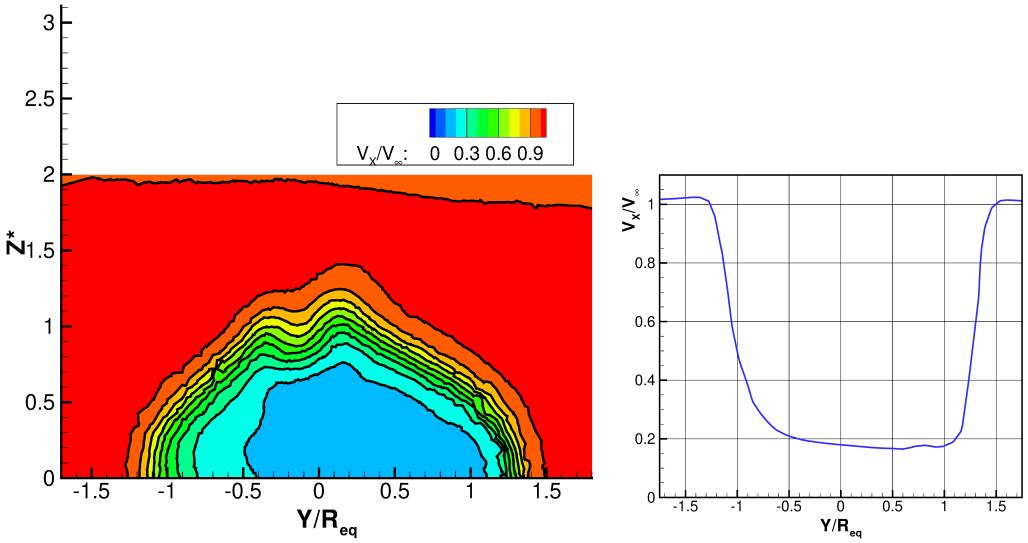

Figure 5.12: 3D computations at TSR_{eq}=4.55: Time-mean wake profiles, CFD wake prediction over section $X/R_{eq=1.5}$ (left) and on the symmetry plane (right)

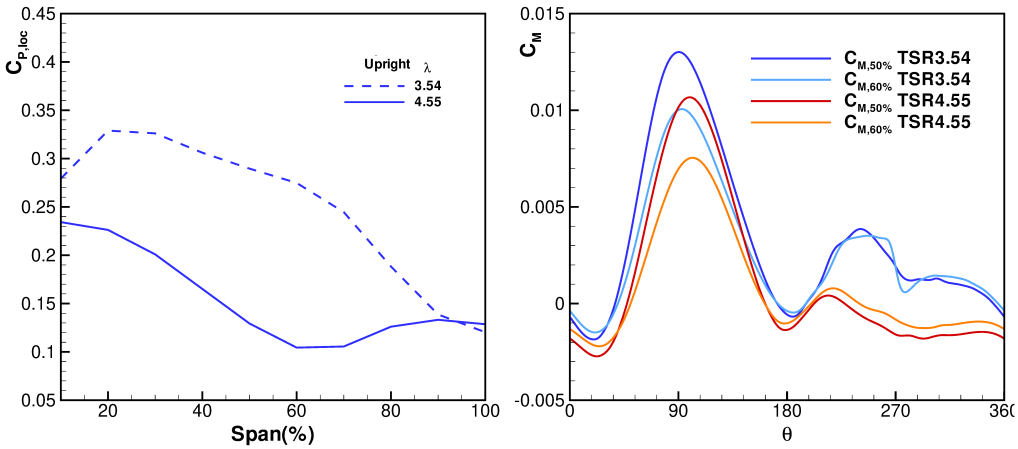

Figure 5.13: 3D computations at TSR_{eq}=3.54 and 4.55: local and cumulative (left) C_P distribution for the upright configuration; 3D computations at TSR_{eq}=3.54, 4.55 moment coefficient at Z^*=50, 60 %

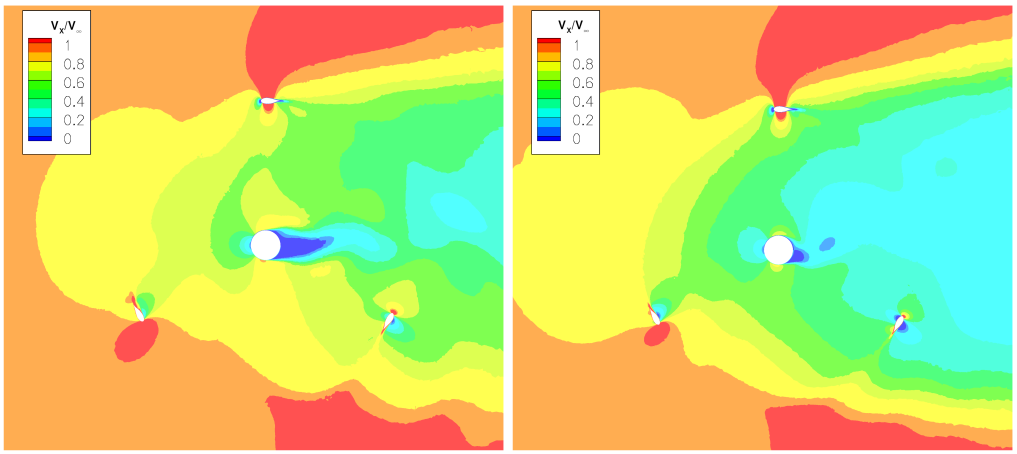

Figure 5.14: 3D computations: non-dimensional streamwise velocity at $Z^* = 0.5$, TSR_{eq}=3.54 and 4.55 (left/right).

5.2.1 Peak power condition: Upright vs Tilted

In this section, the computed 3D outcomes for a 15-degree tilted configuration, operating at the peak power condition, are discussed alongside the available experimental data. Integral power coefficient values, which serve as a comprehensive measure of machine performance, are detailed in Table 5.2. With respect to the experimental data, the numerical results indicate an underestimation of the predictions by approximately 15% in both upright and tilted conditions. However, the overall C_P coefficient experiences the same reduction of approximately 6% with the transition from the upright to the tilted configurations in both experiment and simulation.

C_P	Num	Exp
Upright	0.28	0.34
Tilted	0.264	0.32

Table 5.2: Power coefficient at peak power: 3D CFD against experiments

Additional investigation is required to enhance comprehension of the disparities between predictions and measurements, as well as to gain a more profound insight into the fundamental physical phenomena. Figure 5.15 presents a localized comparison between the computed and measured velocity field at a near wake position ($X/R_{eq} = 1.5$). Enhanced energy extraction is effectively represented in the windward region along the span, and the predicted shape of the velocity deficit closely aligns with the measured profiles. A general overall concordance between the computed flow field and the measurements is observed.

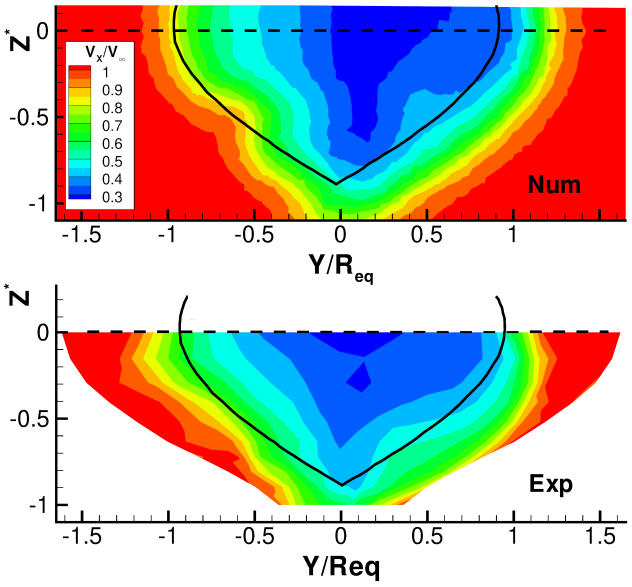

Figure 5.15: 3D computations at TSR_{eq}=3.54, 15deg tilt: non dimensional streamwise velocity at X/R_{eq}=1.5, experimental measurement in comparison with numerical prediction

The subsequent discussion concerns the distinct operational behaviors exhibited by the machine in both the upright and tilted configurations. The reduction in performance observed in

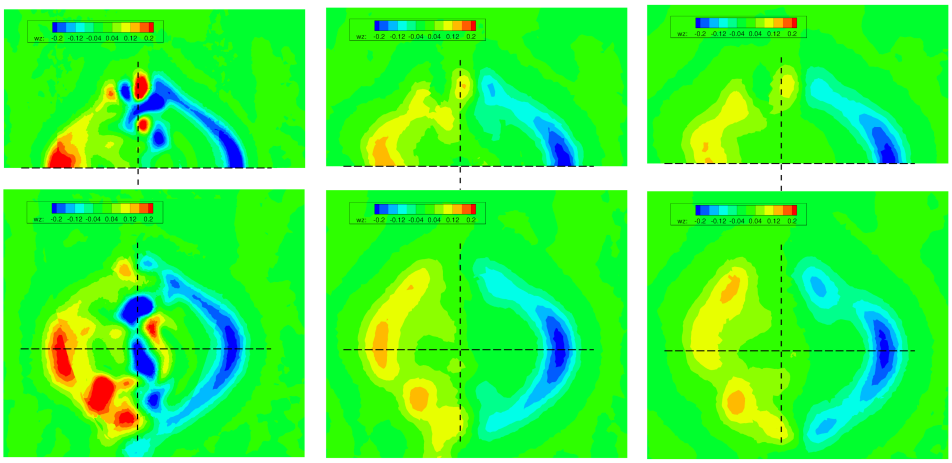

Figure 5.16: 3D computations at TSR$_{eq}$=3.54: non dimensional spanwise vorticity at X/R_{eq}=1,2,3 - upright/15deg tilt at top/bottom

the latter scenario can be attributed to the heightened complexity in the evolution of flow structures within and in the wake of the rotor. The presence of yawed and skewed flow conditions could facilitate the detachment of vortical structures transitioning from bottom to top regions. Figure 5.16 illustrates the non-dimensional spanwise vorticity for the upright configuration in comparison with that corresponding to the tilted condition, observed at three distinct near-wake cross-sections X/R_{eq}.
At the first cross-section $X/R_{eq} = 1$, the flow is in the process of departing from the wind rotor, whereby the vertical vortices manifesting within the lower portion of the tilted machine exhibit greater strength and a more extensive spatial distribution compared to their counterparts in the upper part, this indicates that the lower part exchanges work in a more pronounced manner compared to the upper part. As one progresses downstream, the discernible distinction in vorticity between the two regions persists, albeit diminishing as expected.

In order to enhance comprehension of the distinct operational behaviors across various parts of the machine, Figure 5.17 presents the local power coefficient calculated at diverse spanwise locations (as indicated by the colored sections in Figure 5.5), traversing from the bottom (-100%) to the top (100%). Nevertheless, it is noteworthy that the distinct sections exhibit different behaviors, as evidenced by the trends delineated in Figure 5.17. The ultimate rationale for this outcome arises from the aerodynamic characteristics, where the unsteady detachment of vortical structures, in conjunction with their interaction with the solid blades, governs the performance of the VAWT.

In Figure 5.18, the left-hand side illustrates a comparison between the C_M (moment coefficient) of two halves of the turbine. The positive half of the turbine (from midspan to top) and the negative half (from bottom to midspan) are considered in a tilted condition. This comparison also includes the torque gathered when the turbine is in its upright state.
In a tilted operational configuration, the lower half of the turbine accumulates a greater share of energy compared to the upright condition, accounting for 60% of the total power extracted

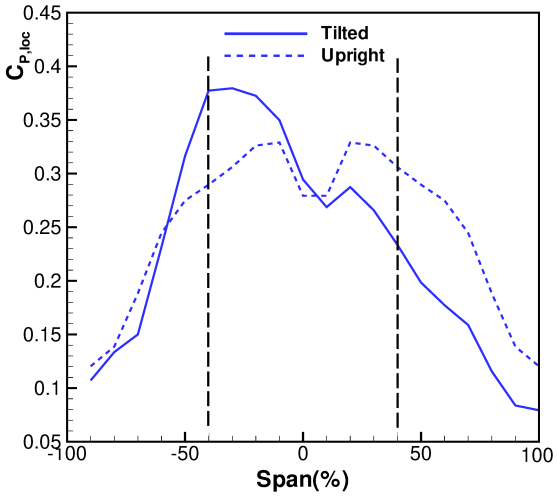

Figure 5.17: 3D computations at TSR_{eq}=3.54: local C_P distribution for the upright and tilted configurations

by this section of the apparatus. The majority of the performance discrepancy becomes evident on the leeward side of the upwind region (as seen when comparing the black dashed dot line to the green solid line). Further assessment can be conducted by examining how the various components of the machine contribute to the torque transmitted to the shaft. The right-hand side of Figure 5.18 showcases the moment coefficients as a function of the azimuthal angle, computed for selected VAWT sections ± 40, 50, and 60%. As a general observation, the lower part exhibits a maximum C_M value that is twice as high as the value obtained for the counterpart positive regions. As anticipated, the tilted condition reduces the effects of turbine curvature (egg-beater-shaped VAWT) for the lower half, especially in the upwind region (tends to become vertical), and increases them for the upper half (tends to become horizontal). Conversely, in the downwind region the opposite takes place, which explains the slightly improved performance observed for the upper part.

The aerodynamic performance comparison between the tilted and upright configurations, as illustrated in Figure 5.18, necessitates a simultaneous evaluation of the energy extraction and the evolution of the near wake. In instances of tilted operational conditions, this process becomes intricate and can not be addressed in a straightforward manner, as the turbine slices experience continuous variations in their vertical positioning throughout the revolution, passing from a maximum at $\vartheta = 90°$ to the minimum at $\vartheta = 270°$.Figure 5.19 illustrates the sketch of the $Z^* = -0.39$ slice, in both the global upright and the local tilted reference frames, which helps to appreciate the different locations of the two highlighted monitoring surfaces. Furthermore, the figure provides a representation of the actual streamlines originating from an upwind location. This evolution of the wake is comprehensively depicted in Figure 5.20 and Figure 5.21 which presents non-dimensional streamwise velocity contours for selected slices at 30 and 90 degrees of azimuthal position, by considering the local tilted reference system (15deg) and global upright reference system. The first reference frame serves to depict the actual flow field that the profile encounters during its revolution around the shaft. On the other hand, the second reference frame is employed to monitor the evolution of the wake at approximately the same height from the ground. Indeed, focusing on the lower part of Figure 5.20, the wake being observed corresponds

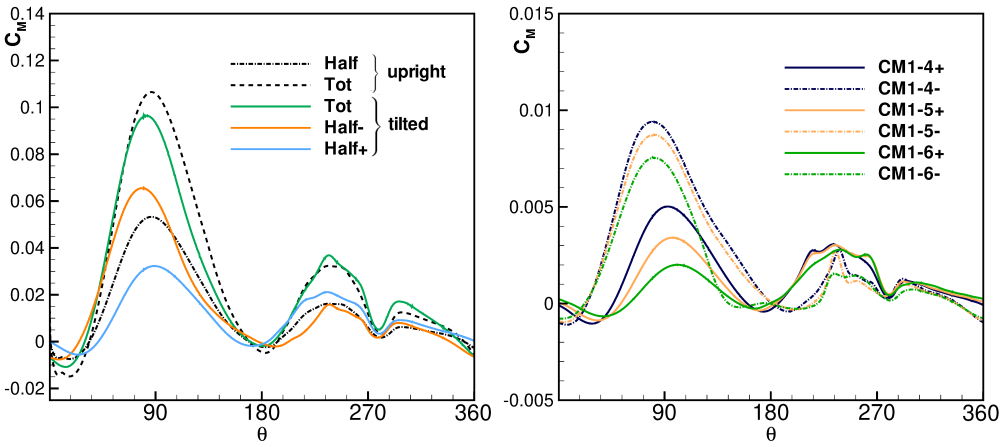

Figure 5.18: 3D computations at TSR_{eq}=3.54: moment coefficient of one blade for the upright configuration in comparison with 15 deg tilted operating case (half± indicate the upper and lower half contributions) LHS; moment coefficient blade 1 for the 15deg tilted configuration at lower and upper 4,5,6 "slices", RHS

to the region still below -39% (that is, between -70% and -100%, see the streamline in figure 5.19). Given the turbine's shape in that area and the inclination of the local reference system, the wake is decreasing. If instead considering the global reference frame, see Figure 5.21, the wake shape is completely different. By comparing the two figures, the spanwise development of the near wake can be observed. This entails noticing that the wake becomes non-symmetric and narrower, which emphasizes the reduced energy harvesting on the leeward side as it moves downward. This is due to the local decrease in TSR value in that region.

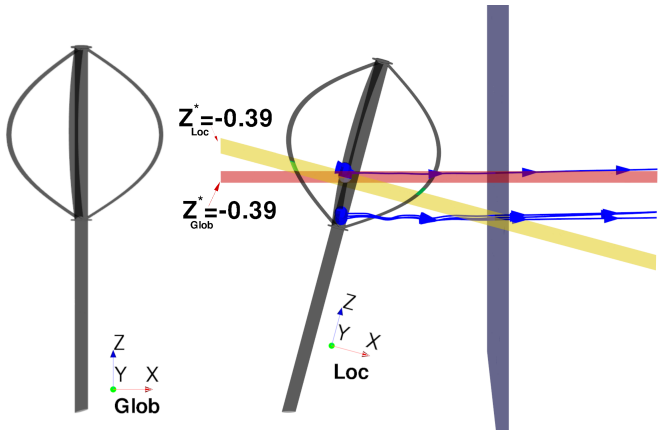

Figure 5.19: Global and local reference system: upright and tilted slices at $Z^* = -0.39$

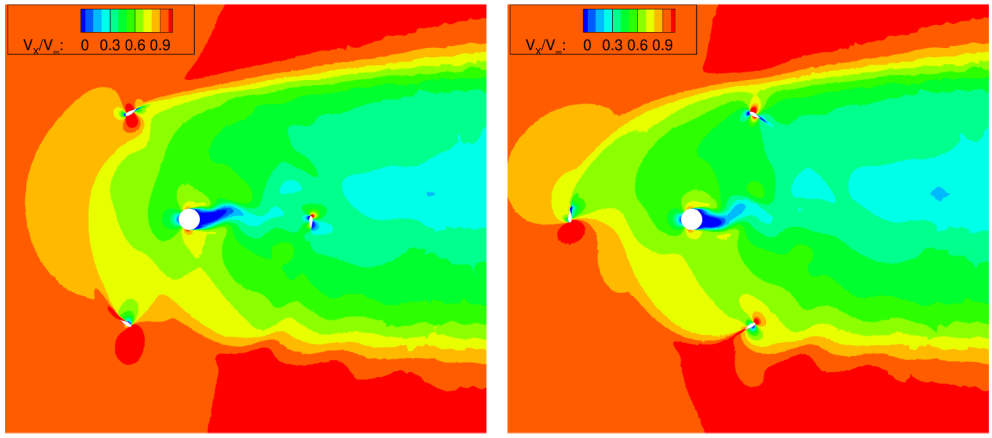

Up, $\vartheta = 30°$ Up, $\vartheta = 90°$

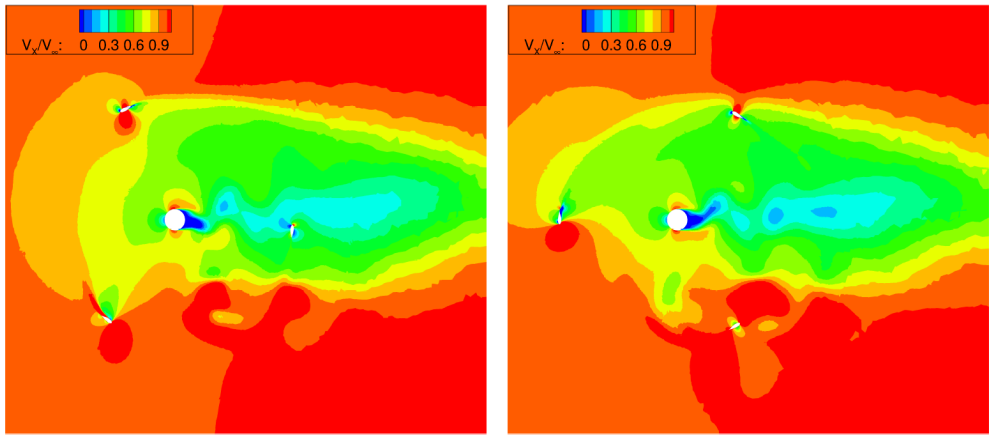

TiltH-, $\vartheta = 30°$ TiltH-, $\vartheta = 90°$

Figure 5.20: 3D computations at TSR_{eq}=3.54 with **Local Tilted reference system**: non-dimensional streamwise velocity for the upright case (top) $Z^* = 0.39$ and tilted (bottom) at $Z^* = -0.39$

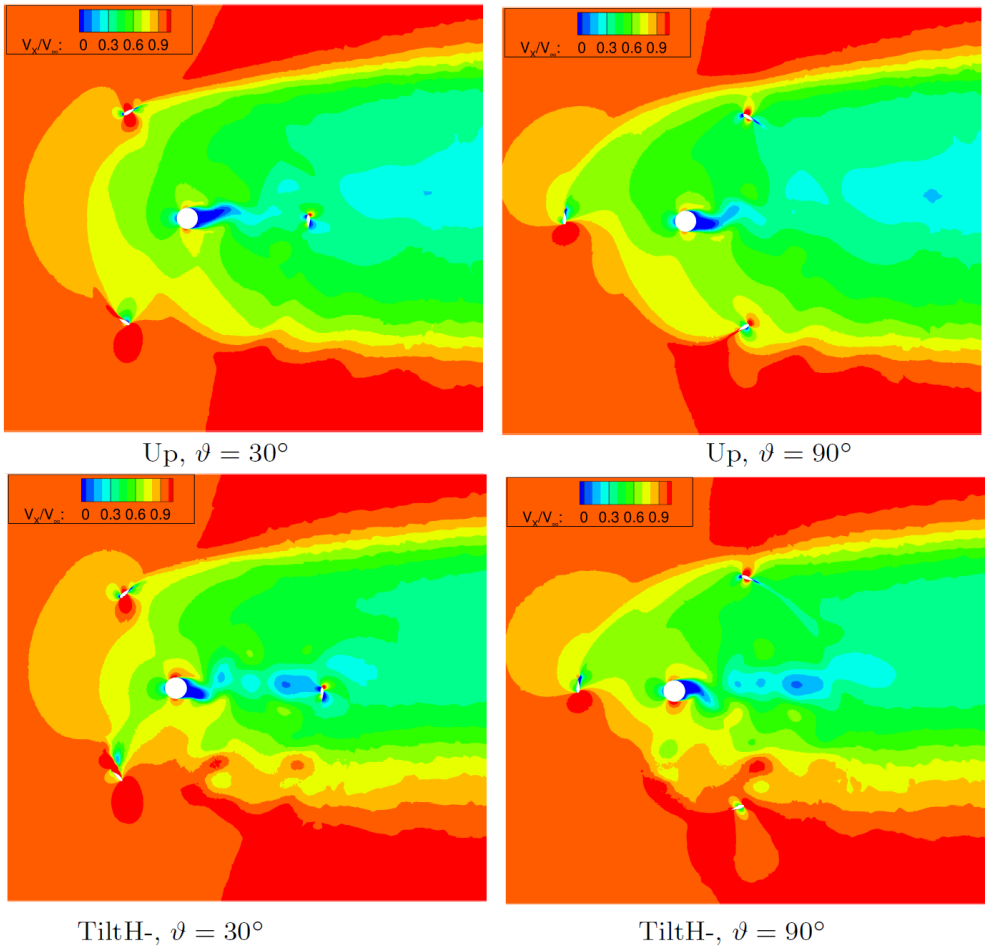

Figure 5.21: 3D computations at TSR_{eq}=3.54 with **Global Upright reference system**: non-dimensional streamwise velocity for the upright case (top) $Z^* = 0.39$ and tilted (bottom) at $Z^* = -0.39$

5.3 Large scale model: upright configuration

Offshore Vertical Axis Wind Turbine (VAWT) installations necessitate the use of multi-megawatt turbines to meet the challenging green energy demands while maintaining favorable economic parameters. Consequently, addressing the scaling of the machine is of dual significance: i) evaluating its performance under real flow conditions, accounting for Reynolds number influences, and ii) guaranteeing structural stability, particularly when dealing with large-scale machines where considerations related to the center of gravitational forces and gravity become paramount. In this context, this discussion primarily focuses on the former aspect, entailing an examination of machine performance from the perspective of fluid machinery.

As is commonly recognized, when working with scaled models compared to their full-scale counterparts, it is imperative to account for non-similarity effects, with a primary focus on investigating the Reynolds number effect. Additionally, in the case of large-scale machines, aeroelastic instabilities may also be affected due to heightened tip speed ratios and the system's low natural frequency [67]. However, this section undertakes a comparison between a full-scale wind turbine and a small-scale laboratory model in their upright positions. The aim is to assess their respective abilities in power generation and wake formation, providing insights into how the turbine's performance may be impacted by the scaling factor of the machine. The full-scale model examined in this context possesses a scaling factor of 60 in relation to the small laboratory model, resulting in a Reynolds number of approximately 10 million.The calculations were conducted using the same numerical settings and discretization guidelines as previously outlined for the small-scale laboratory model. Exception made for the turbulence modeling, where the standard $k-\omega$ SST model has been adopted.

Figure 5.22 illustrates the moment coefficient comparison between the large-scale and small-scale models. A distinct advantage of the full-scale machine is noticeable in the upwind section, exhibiting an approximate 25% increase. This results in an overall C_P value rise from 0.28 (for the small lab model) to 0.35 (for the large model).

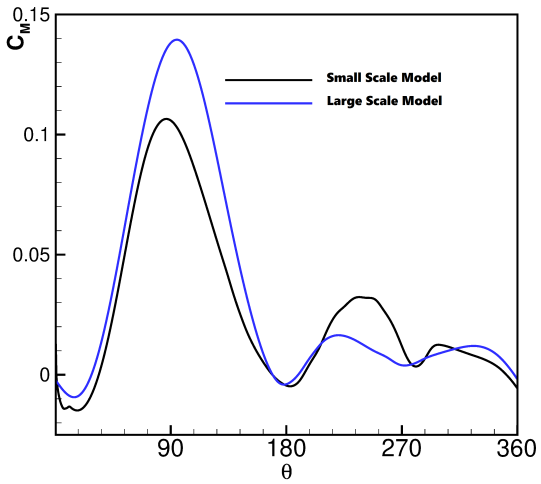

Figure 5.22: 3D computations at TSR$_{eq}$=3.54: moment coefficient of upright configuration - small scale lab vs large scale model

Figure 5.23 illustrates the local power and the cumulative power coefficients, left and right

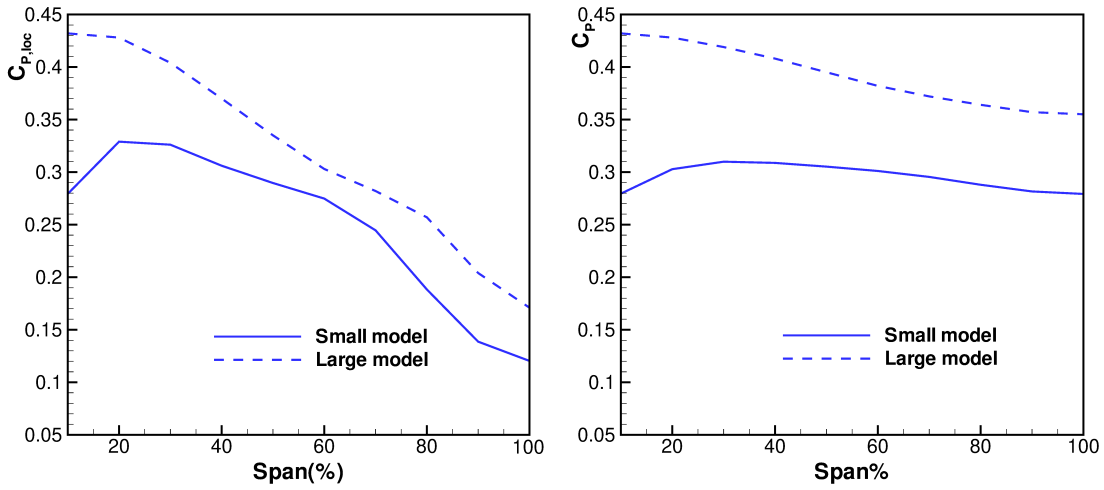

Figure 5.23: 3D computations at TSR_{eq}=3.54: local and cumulative power coefficient of upright configuration (left/right) - small scale lab vs large scale model

respectively, of the chosen rotors as moving spanwise. The reported results suggest how the Reynolds number effect is having an impact. A monotonically decreasing trend is provided by the large-scale model. Worth noting the trend near midspan, where the local behavior registered by the small scale rotor is thus observed to be a result of the low Reynolds number flow promoting the vortices already commented in Figure 5.10 using the lateral vortices arising in the leeward side, close to the midspan region (displayed both by numerics and experiments).

The velocity field behind the rotors allows to describe how the energy harvesting process takes place while the vortices are developing; the higher velocity defect that explains the enhanced performance of the large scale can be readily observed from Figure 5.24. Additionally, Figure 5.25 offers further visualization, emphasizing the impact of a fully turbulent regime on a blade at $\vartheta = 120°$. Finally, Figure 5.26 provides the companion representation, featuring near wake profiles at two subsequent downstream cross-section positions for both rotor sizes. The leeward side once again demonstrates the positive effect of a "re-energized" flow field, displaying reduced susceptibility to transitional instabilities owing to the substantial Reynolds number of the full-scale model. A similar evolution of the wake is instead observed for the machines, as they transition from X/R_{eq} equal to 1.5 to 2.5. This transition leads to a comparable decrease in velocity, though at different locations.

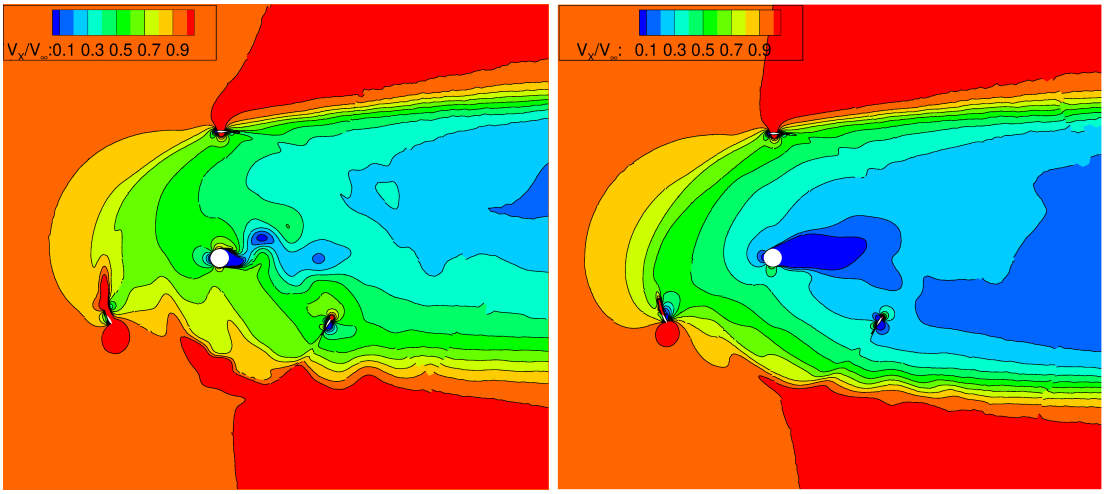

Figure 5.24: 3D computations at TSR_{eq}=3.54: non dimensional streamwise velocity at midspan - small scale lab vs large scale model

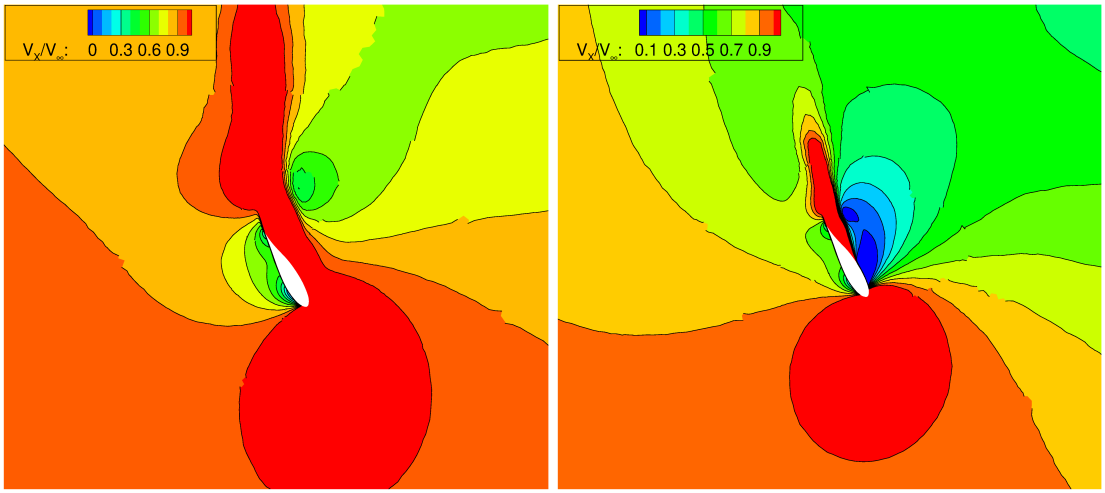

Figure 5.25: 3D computations at TSR_{eq}=3.54: non dimensional streamwise velocity at midspan - small scale lab 8left) vs large scale model (right) - enlargement $\vartheta = 120°$

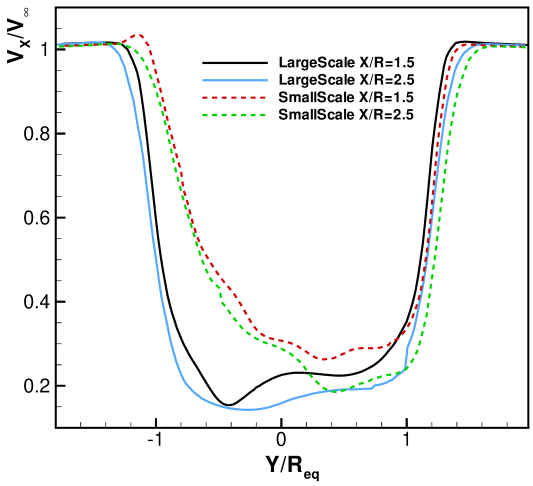

Figure 5.26: 3D computations at TSR_{eq}=3.54: near wake velocity profile on the midspan plane, at $X/R_{eq} = 1.5, 2.5$

Chapter 6

Case 3: H-shaped VAWT

6.1 Case of Study

In this chapter, the model under investigation is a small-scale, H-shaped VAWT, which comprises three unstaggered blades, affixed to the shaft via two supporting streamlined struts. The blades exhibit a NACA0021 airfoil with a chord length of 0.101 meters. The aspect ratio, defined as the ratio of the blade height to the rotor diameter, is set at 1. Moreover, the rotational speed of the turbine remains constant at 300 revolutions per minute (rpm). With a radius measuring 1.01 meters, this machine can be considered a small-scale laboratory model, suitable for simulating utility-scale devices while simultaneously serving as a real-scale rotor for distributed micro-generation applications. The dimensions of the turbine have been established based on design guidelines that were previously employed in a laboratory model investigated [37]. The aerodynamic characteristics of the turbine are subject to considerable influence from several factors, including the geometric aspect ratio, the Reynolds number effect, the airfoil shape, and other pertinent considerations. Previous works documented in the open literature have extensively addressed these topics. For instance, in the work by [81], a comprehensive investigation into the Reynolds number effect, the implications of viscous losses, and their correlation with the geometric design of VAWTs were presented. Undoubtedly, achieving a singular optimum design for the turbine is not possible, primarily due to the fact that pertinent factors merge in distinctive ways under varying operational conditions. However, a widely adopted choice entails selecting an aspect ratio that closely approximates unity, also with laboratory scale turbines [68]. Therefore, for the purpose of carrying out a reliable numerical study on the effect of skewness applied to VAWTs, the described configuration was chosen. Notably, this choice was motivated by the inherent structural advantages associated with the selected configuration.
Table 6.1 presents a comprehensive summary of the chosen test cases, detailing the free-stream velocities and TSR values. Also in this case, throughout the simulations, the rotational speed remained constant, while the free-stream velocities varied correspondingly. These specific operating conditions were purposely selected to represent distinct scenarios: the peak power point and two off-design conditions characterized by high and low loads.

Table 6.1: Test cases: operating conditions

	Case A	Case B	Case C
Wind speed[m/s]	10.0	9.0	8.2
TSR	3.18	3.54	3.90

6.1.1 Computational model

Comprehensive simulations employing a high-fidelity CFD tool were conducted to investigate the aerodynamic characteristics of an H-shaped VAWT under both upright and tilted configurations. In congruence with the preceding cases of study, the numerical discretization methodology adopted entailed the assumption of the fluid's behavior as that of an ideal and incompressible gas, characterized by unvarying thermophysical properties. The discretization process of the governing equations was conducted by applying URANS modeling, incorporating a turbulence model focused on resolving near-wall flows. The $k-\omega$ SST turbulence model, developed by Menter [61] was selected since it has been demonstrated to offer accurate predictions of intricate vortical structures. see *e.g.* [6]. Both spatial and temporal discretization were executed using second-order accurate schemes.

The definition of domain boundary locations is imperative to circumvent contrived blockage effects. Additionally, these boundary positions should be set in order to minimize the domain and the excessive computational expenses (as reported in [38]). In accordance with the guidelines outlined in [38], the 3D domain exhibits distinct features, comprising an inlet boundary positioned at a distance of 4.5 diameters upstream from the shaft, an outlet surface situated 3.0 diameters downstream, and lateral ones situated at 3.0 diameters from the central shaft.

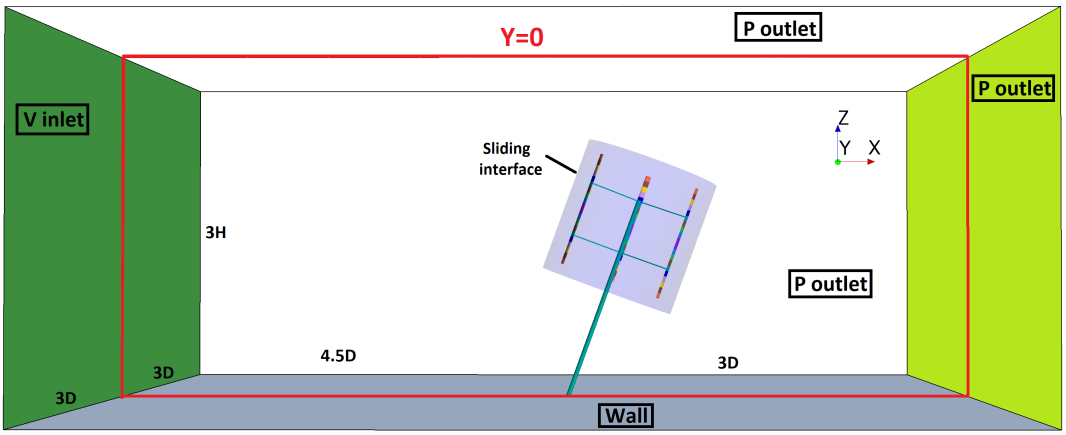

Figure 6.1: 3D computational domain and boundary conditions

The construction of the grids has been executed in accordance with the clustering outlined in [37, 38]. The creation of these grids, which include a total of approximately 24 million polygonal cells, has been carefully defined using a sensitivity analysis approach. Additionally, in pursuit of attaining enhanced precision, a minimum spacing of $2 \cdot 10^{-5}$ m from the solid wall was employed in order to satisfy the constraint of $y^+ \approx 1$ and so achieving a proper simulation of the near-wall region. Furthermore, a local growth factor of 1.1 was applied to refine the boundary layer. An expanded depiction of a refined area, notably the intersection between the strut and

blade, is presented in the left segment of Figure 6.2. Within the same visual representation, the evolution of the refinement along the spanwise orientation is exhibited on the right-hand side. Additionally, a comprehensive description of the sections, sequentially labeled from the lowermost to the uppermost, is presented. The utilization of negative labels ranging from -10 to -1 signifies the zones situated within the lower half of the turbine, whereas the positive labels correspond to regions located in the upper half. These delineated regions were employed to conduct a more precise and localized assessment of flow field developments. Consequently, they were used for the computation of localized power harvesting.

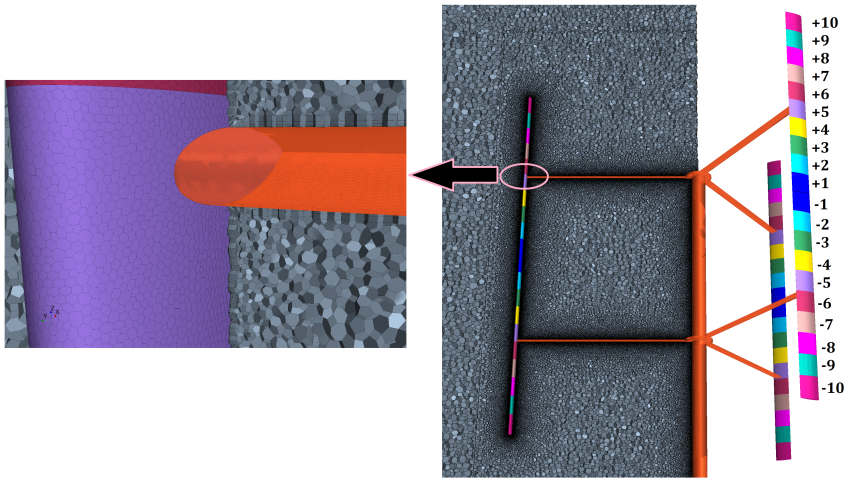

Figure 6.2: Computational domain: Detailed view of the junction between the aerodynamic struts and a turbine blade on the left, with a cross-section of the grid superimposed to the VAWT geometry. The spanwise regions labeled slice $\pm j$

The selection of the time step value, a factor pivotal to the accuracy of the solution, was made in such a way as to partition the entire revolution into 720 instants. This decision is substantiated by the recommendations expounded in other works, *e.g.* [12] and is predicated upon widely applied sensitivity analysis principles.
An algebraic multigrid solver was employed to resolve the system of governing equations at each time step, iteratively advancing the solution until the prescribed accuracy threshold of 10^{-5} was satisfied. For every operational scenario, computations were executed until the achievement of a periodic solution, attaining a stable flow field across all examined conditions between the 15th to the 20th revolutions of the turbine. Nevertheless, in order to verify the periodicity, the average torque value gathered at the shaft, computed over a single revolution, was recorded. Subsequently, the most recent five mean values were subjected to continuous monitoring until the relative error reached a level below 1%, thereby serving as the established convergence criterion. The employed boundary conditions are detailed in Figure 6.1. Specifically, at the inlet surface, the conditions entailed a freestream velocity maintained at a fixed value, accompanied by a turbulence intensity of 1%, and a turbulent viscosity ratio set to 1. These specifications align both with conventional experimental data and the chosen turbulence model. The lateral, downstream, and upper boundaries were assigned prescribed static pressure conditions. Meanwhile, the no-slip wall condition was enforced along solid (rotating) surfaces, as well as to the ground surface.

6.2 VAWT upright condition

In this particular section, a comprehensive study of the considered VAWT's performance in its upright configuration is presented. The principal objective encompasses the establishment of a foundational rationale, proving a link between the machinery's capability for harnessing energy and the intricate factors wielding influence on its overall performance. These factors encompass: i) the perturbative impacts arising due to blockage phenomena, ii) the 3D viscous losses, and iii) the unsteady vortical structures manifesting within and trailing the rotor, thereby directly affecting the wake's evolution and subsequent recovery. It is common knowledge that the blades of a turbine have the potential to experience deep, dynamic stalls at various points during its rotation. Accordingly, the aerodynamic performance prediction must be able to appropriately handle all such aspects.

6.2.1 Symmetry Assessment

Before delving into the main topic, the evaluation of the symmetry condition at midspan is conducted. In fact, assuming the validity of the symmetry condition proves highly advantageous, as it effectively lowers the computational expenses. Generally, in cases where tilting movements are not considered, the discrete domain may fully exploit the rotor design with geometric symmetry around the equatorial section. Moreover, in the absence of considerations pertaining to the atmospheric boundary layer, the inflow also adheres to the condition of symmetry. Nonetheless, a significant aerodynamic instability can emerge when dealing with a stalled rotor, particularly in situations where the TSR is low. This instability can lead to an asymmetric flow field. To demonstrate the symmetry of the flow, comprehensive simulations of the complete turbine at a TSR of 3.54 (which corresponds to the peak power condition) were conducted and examined. The computational mesh used in this analysis is composed of 24 million elements and follows the criteria mentioned earlier. The initial focus is on comparing sections of the flow that are symmetrically positioned relative to the midspan of the turbine.

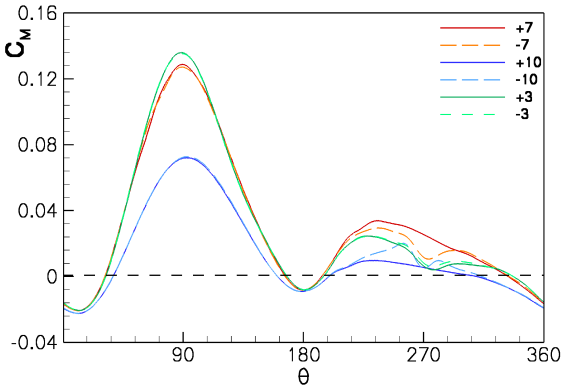

Figure 6.3: 3D moment coefficient at TSR=3.54, upright: torque computed on slices number $\pm 3, 7, 10$ as function of θ

Figure 6.3 displays the moment coefficient that has been calculated for specific cross-sectional slices along a single blade. These slices are situated at positions denoted as $\pm 3, 7, 10$ as indicated in Figure 6.2. This comparison is conducted to assess the symmetry between the upper and lower sections of the turbine. The torque values projected at the ± 3 slices exhibit a notable

resemblance to each other. Upon comparing slices at positions ±7 and ±10, it becomes evident that the variation between the upper and lower sections of the rotor is confined to a narrow area during the downwind phase of the rotation. This discrepancy is closely tied to the presence of the pole, which concludes at the +5 slice. The resulting impact on the overall C_p value for the half model, when contrasted with that of the entire rotor, remains under 1%. As expected from this initial analysis, the simulation results that leverage the symmetry boundary condition closely align with those obtained for the upper half of the rotor when considering the complete rotor configuration. This observation strongly indicates that, in the vertical arrangement, the aerodynamics of the rotor can be effectively represented using the symmetry boundary condition.

6.2.2 Flow field at midspan

The study focused also on assessing the aerodynamics of the rotor by analyzing the predicted moment coefficient in relation to the azimuthal angle within the middle or equatorial part of the machine. To achieve this, only the forces contributing to the moment coefficient (C_M) from a thin section located at the midspan of the rotor (referred to as "slice 1" in Figure 6.2) were taken into account, excluding the three-dimensional effects derived from the full 3D computation. The comparison of 3D C_M profiles was conducted at three different TSR values: the condition of peak power ($TSR = 3.54$), as well as off-design scenarios at higher ($TSR = 3.18$) and lower ($TSR = 3.90$) freestream velocities, as depicted in the left segment of Figure 6.4. The findings indicate that as the TSR value increases, the downwind region experiences a reduction in available torque. Consequently, as the TSR increases, a substantial proportion of the harnessed torque originates at the zone within fresh airflow. Moreover, the maximum C_M value occurs at greater azimuthal angles. Particularly at low TSR values, the aerodynamic performance is significantly affected by dynamic stall, where vortices develop more rapidly in the downwind.

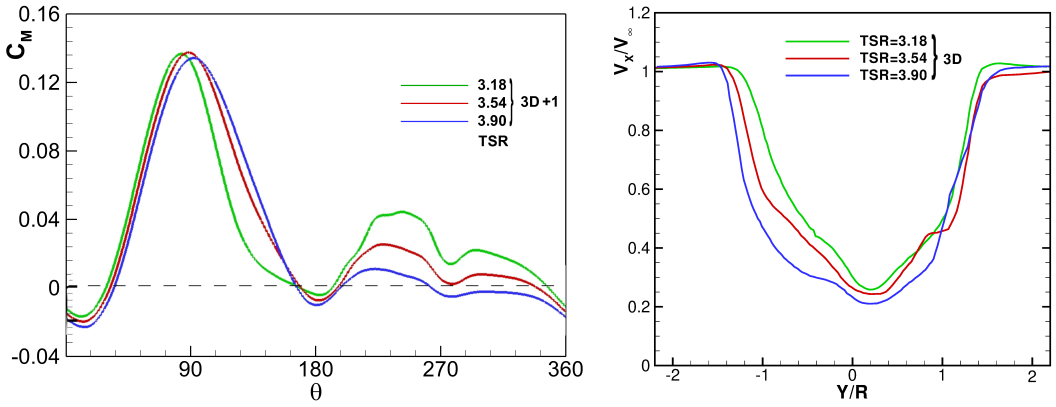

Figure 6.4: Left: Moment coefficient: 3D computed on slice number 1 as function of θ. Right: Near wake velocity defect: 3D midspan non dimensional streamwise velocity at $X/R = 1.5$

The right segment of Figure 6.4 illustrates the characteristic expansion of the wake region and major velocity defect observed within the increase of TSR values. This observation substantiates that the wake exhibits a quicker recovery in instances characterized by lower TSR values.

6.2.3 3D Effects

This section examines the effects exerted by both struts and blade tips on the turbine's overall performance and on the flow structure development at different TSR values. This exposition aims to establish a foundational reference for subsequent comparison with the tilted configuration. Moreover, given the turbine's previously stated symmetry, the following analysis is restricted to the upper half of the turbine.
To assess the viscous losses attributed to the friction acting on the struts, as well as the effects of the blade tips, the torque distribution throughout a complete revolution is analyzed at specific spanwise locations. Figure 6.5 represents the predicted moment coefficient across the investigated TSR values, delineated for three distinct slices, namely the midspan (label 1), the location of the strut attachment (label 5), and the slice at the blade tip (label 10).
Numerous observations can be deduced:
i) A coherent behavior is evident, whereby an increase in the TSR value leads to a corresponding amplification in the influence of losses, primarily attributable to heightened frictional resistance induced by the presence of supporting struts; ii) The machine portion aligned with the location of slice 5 manifests an almost counterproductive impact on power extraction, exhibiting a clearly "braking" effect that assumes greater significance with the increase of the TSR value; iii) By examining the distributions of moment coefficient (C_M) presented for slice number 10, the losses occurring at the blade tip due to the finite blade length effect can be better understood by comparing them with the torque obtained at midspan reported in the figure.

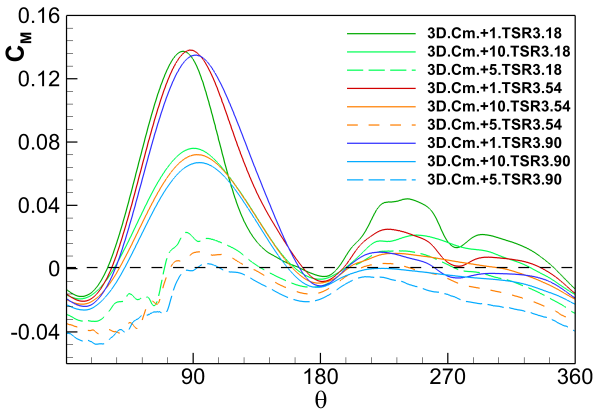

Figure 6.5: 3D moment coefficient at TSR=3.18, 3.54, 3.90: torque computed on slices number 1, 5, 10 as a function of θ

For a more precise quantification of the performance decrement attributed to 3D losses, the local coefficient of power (C_P), calculated across the spanwise, is depicted in Figure 6.6. It elucidates the correlation between effective power and each position, as discussed earlier. Notably, a conspicuous loss peak emerges around the 50% span position.
The findings discussed in this section, introduce the main issues that play an important role in the VAWT performance evaluation, and finally, they prompt the reasoning lines useful to understand the turbine behavior when operating in the upright condition. In the next sections, the VAWT behavior is instead investigated when different tilting angles are considered.

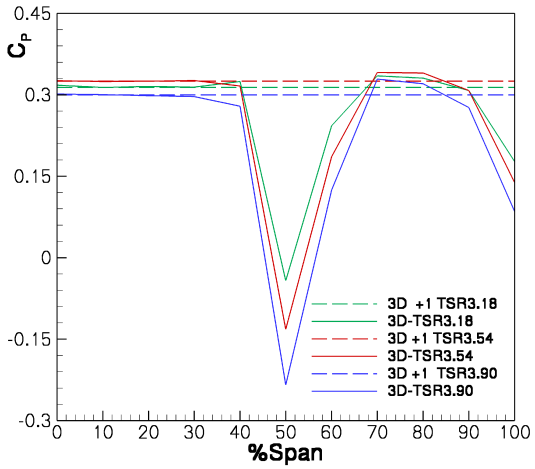

Figure 6.6: 3D local power coefficient at TSR=3.18, 3.54, 3.90: power computed spanwise over each slice from midspan (0%) to top (100%)

6.3 VAWT tilted condition

The prediction of performance in a tilted configuration holds evident significance for practical applications, wherein factors like freestream distortion, turbulent onset, and external forces commonly lead to deviations in the operational flow field from the upright reference state. As such, it becomes doubly imperative to adequately quantify the impact of skewed flows on VAWT operations. This serves two key purposes: i) Gaining insights into the development of vortical structures based on this understanding. ii) Attaining reliable

predictions of performance.

Dealing with inclined rotors introduces several considerations. Among these, there is the reduction of the normal wind velocity component, which in turn slightly decreases the angle of attack. This effect is anticipated to be particularly pronounced during low wind speeds. Additionally, alterations in the swept area occur as the turbine tilts, as well as the flow encounters a thicker airfoil section.

6.3.1 Swept area variation

While operating in a tilted configuration, the frontal area of the turbine undergoes changes as dictated by the formula depicted in Figure 6.7. This formula is a function of the VAWT's aspect ratio (H/D), as illustrated therein. As per this formula, the swept area experiences an increase, reaching a peak value that is contingent on its aspect ratio. Subsequently, it begins to diminish until it equates to the area of a circle when the inclination angle attains 90 degrees. The maximum of the swept area occurs at a lower tilting angle as the H/D parameter increases. In a consistent operational position, larger swept areas manifest at lower H/D values. This geometric characterization profoundly impacts the turbine's energy harvesting capacity. The present section of the study additionally attempts to gain deeper insights into the evolution of the vortical structures occurring both within and beyond the rotor. Furthermore, when transitioning from upright to tilted operations, considerations must encompass aspects such as viscous losses, blockage effects, and aerodynamic phenomena to facilitate a more comprehensive discourse on

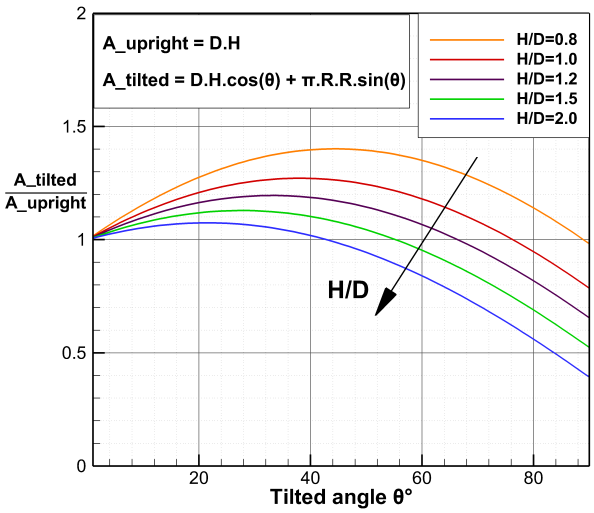

Figure 6.7: Rotor turbine swept area as a function of H/D: upright vs tilted operating condition

the machinery's behavior. Concluding this, it's worth noting that operating in tilted conditions with an H-shaped design turbine like the one under examination in this study, the streamlines only partially intersect with the rotor, particularly in specific lower spanwise regions located within the downwind zone. This is predicted to lead to an overall increase in performance.
In the subsequent sections, an analysis is conducted on the influence of the tilting angle on various factors. These factors encompass the freestream wind conditions, the magnitude of viscous losses, the swept area, and the evolution of the near wake.

6.3.2 Tilted vs Upright: different TSR values

To begin, the results presented herein, demonstrate how the presence of a tilt angle modifies the effects of viscous losses at different TSR values. For this section, a tilt angle of 20 degrees is considered as the reference parameter. Figure 6.8 depicts the variation of the local power coefficient concerning the spanwise position within the reference slices group. This computation is conducted across three different TSR values. Clearly, upon the introduction of a tilt angle, a noticeable divergence in power harvesting capability becomes evident between the lower and upper sections of the turbine, irrespective of the TSR condition. In fact, when operating in a tilted configuration, an augmentation in the value of C_P becomes discernible in the lower half, whereas conversely, a contrasting pattern is observable in the upper half of the turbine.
The impact of inclination becomes more noticeable as the TSR value rises since a portion of the lower half of the turbine meets fresh air both in the upwind and downwind zone and as observed in figure 6.4, more pronounced energy can be recovered when dealing with high TSR. Moreover, significant friction-related effects manifest in the upper half of the turbine owing to the adverse influence of the machine's inclination. In contrast, the converse outcome is observable in the lower portion, where a diminished loss of power coefficient is evident. This is also a result of encountering fresh air in both upwind and downwind zone for the lower half (less braking effect).

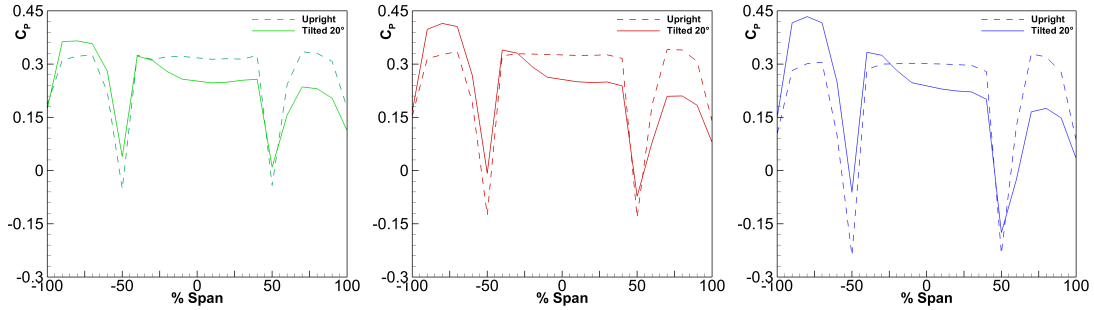

Figure 6.8: 3D local power coefficient at TSR=3.18, 3.54, 3.90 (left/middle/right): upright in comparison to 20deg inclined operation

The amplified power/torque potential in the lower segment of the rotor under inclination is evident in Figure 6.9. This heightened capacity for power conversion primarily depends on the increased torque harnessed by the blades within the downwind region of the turbine's revolution. Notably, the torque derived from a slice positioned in the lower region of the turbine (-8) surpasses that of a corresponding slice situated in the upper portion of the rotor (+8).

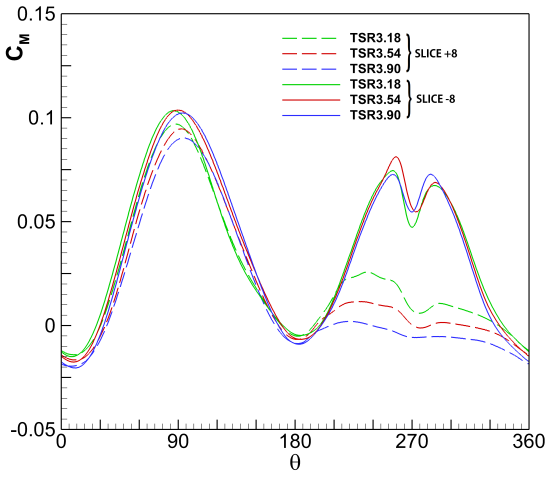

Figure 6.9: 3D local moment coefficient in 20deg inclined operation at TSR=3.18, 3.54, 3.90

Advancing towards the upper and lower segments of the rotor, larger differences in the flow field and local performance are expected. Figure 6.10 presents a comparison between the upright and 20-degree tilted rotor configurations at TSR=3.54, illustrating the C_M distribution over one turbine's revolution, for the slices ± 3 and ± 8 in both the upright and tilted positions. It is apparent that the upwind portion experiences a slight reduction in its capacity to extract active torque in the upwind zone, attributable to the adverse impact of flow inclination. Nevertheless, the tilt notably enhances energy harvesting in the downwind section of the revolution. As expected, the effect of the tilt becomes more pronounced as one moves away from the equatorial section of the rotor.

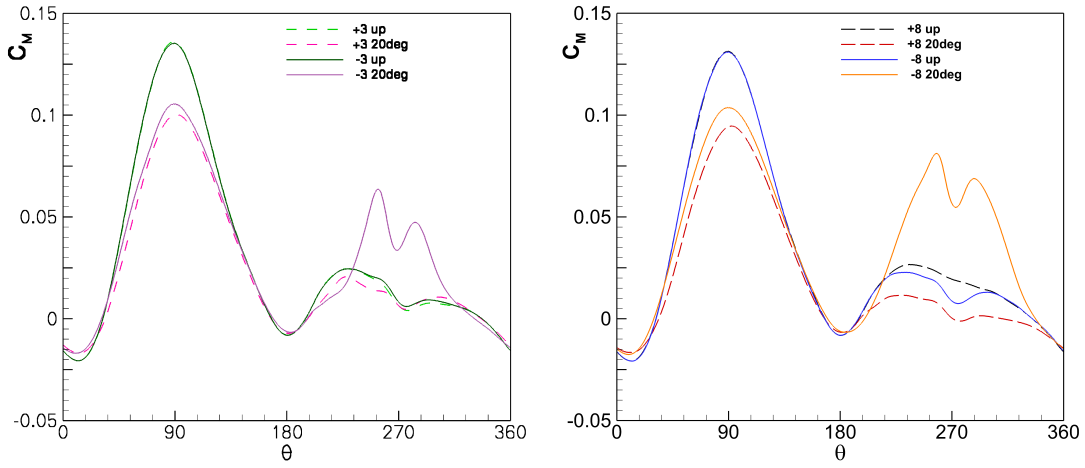

Figure 6.10: 3D moment coefficient at TSR=3.54: upright in comparison to 20deg inclined operation, slice±3 on right and slice±8 on left

6.3.3 Peak power condition: different tilt angles

In situations of skewed flow, an augmented torque becomes conveniently accessible, owing to the fact that the streamlines intersect the rotor only once within the downwind region along a specific span segment. As the flow skewness intensifies, the turbine's lower and upper parts contribute differently. Additionally, the swept area varies as indicated in the previous section. As a result, a detailed examination is required to determine the turbine's performance in harvesting energy across various operational conditions.
In this section, the performance of the VAWT is evaluated across different tilt angles while the rotor operates under the reference peak power condition (TSR=3.54, assessed in the upright condition). Figure 6.11 illustrates the distribution of C_M throughout a complete revolution for both the upper and lower segments of the VAWT, considering tilt angles of 10, 20, and 30 degrees. In the upwind region, these two segments exhibit comparable behavior; however, a decreased torque output becomes evident as the tilt angle increases due to the expansion of the swept area and the subsequent decrease in the relative freestream velocity. On the contrary, within the downwind segment, a distinctive feature emerges between the upper and lower halves of the turbine. While the tilting effect on the upper portion remains negligible (see the right figure), the lower half capitalizes on the opportunity to interact with undisturbed "fresh" air, which exclusively interacts with the rotor's downwind region.

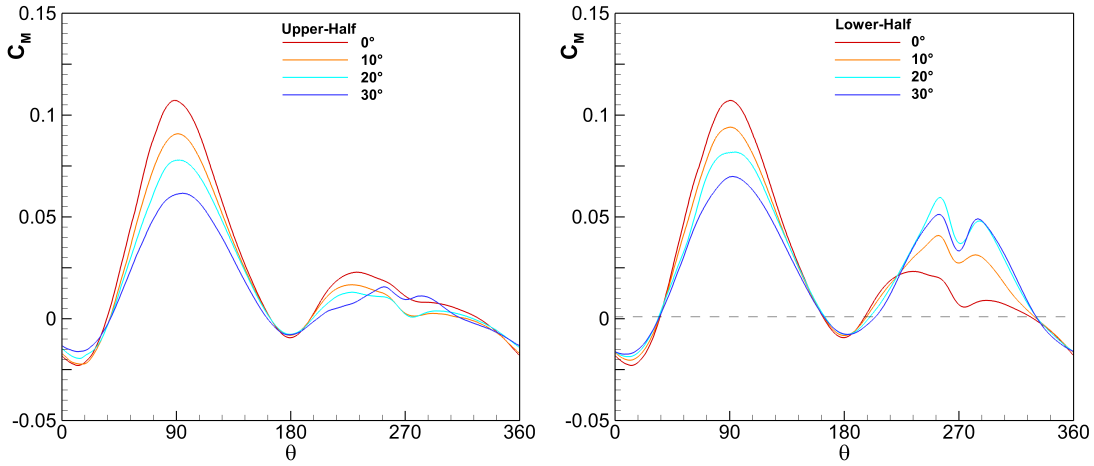

Figure 6.11: 3D torque coefficient at TSR=3.54 of the upper/lower part of the turbine (left/right): inclined operation at 10, 20, 30 deg

Therefore, the escalating availability of energy in the downwind portion becomes notably pronounced when progressing towards the blade tip, as depicted by the designated region Slice ±8 in Figure 6.12.

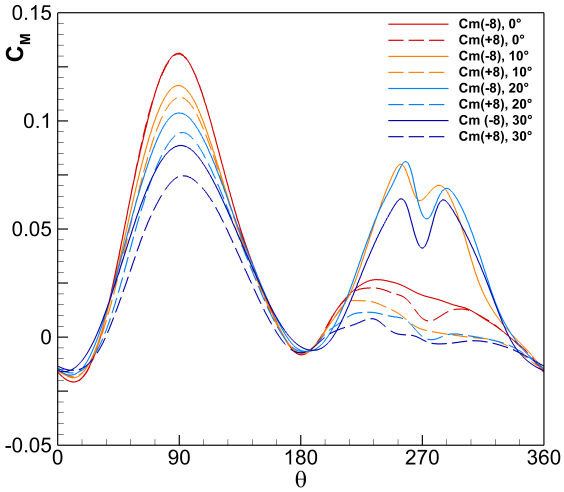

Figure 6.12: 3D torque coefficient at TSR=3.54 of slices ±8: inclined operation at 10, 20, 30 deg

Concerning the power harvesting capacity of the VAWT at varying tilt angles, Figure 6.13 contrasts the power extraction between the upright configuration and the tilted orientations.

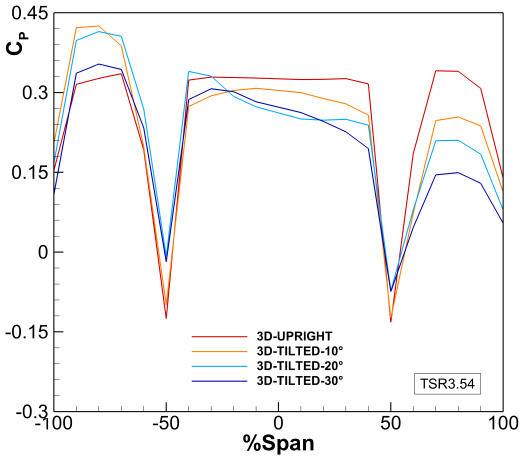

Figure 6.13: 3D power coefficient at TSR=3.54 at inclined operation at 10, 20, 30 deg

In Table 6.2, the computed power coefficient is reported along with the collected power data, swept area, and the relative percentage variations of these parameters in comparison to the upright condition. For TSR=3.54, It is evident that the rotor power output increases by 11% for inclinations of up to 20 degrees, due to the increased swept area (+20%) in combination with the low reduction in power coefficient (small effect of the tilting + the lower half of the turbine generates torque in the downwind region). At a 30-degree inclined rotor position, the aforementioned positive effects are offset by adverse aerodynamics, particularly during the upwind phase of the revolution. This results in a significant reduction of the C_p, and despite the increase in swept area, the collected power becomes lower than that in the upright configuration. In addition,

Angle	C_P	$C_P(\%)$	A_{sw}	$A_{sw}(\%)$	Power	Δ(P)%
0^o	0.25	-	4.04	-	450	-
10^o	0.24	-4.0	4.52	+11.9	464	+3.1
20^o	0.23	-7.6	4.88	+20.8	501	+11.3
30^o	0.19	-24.0	5.08	+25.7	444	-1.3

Table 6.2: TSR=3.54: power coefficient, swept area and gathered power at varying tilting angle

Table 6.3 illustrates the comparison between percentages obtained in terms of power while keeping the angle of inclination constant (20^o) for the three considered TSRs. Significantly notable increments are observed for the highest TSR (low wind speed), as under such circumstances, greater torque is recuperated in the downwind region, as depicted in Figure 6.9.

TSR	Cp_{up}	Cp_{tilted}	$Power_{up}$	$Power_{tilted}$	Δ(P)%
3.18	0.26	0.235	643	702	+3.1
3.54	0.25	0.230	450	501	+11.3
3.9	0.20	0.199	277	331	+19.1

Table 6.3: 20^o: power coefficient, gathered power at varying TSR

6.4 Flow Field: The tilt angle effect

The occurrence of a complex vortical structure resulting from the three-dimensional flow field within a VAWT has significant implications for both the energy harvesting process and wake recovery. In this section, the generation of the wake and its recovery process are delineated, considering a tilting angle ranging from zero to 30 degrees, while the machine operates under peak power conditions. The objective is to reach a deeper understanding of wake evolution and to identify factors influencing the performance establishment. These observations hold particular significance in the context of wind farm design, aiding in the optimization of energy density.
The flow topology of VAWTs operating within field conditions, functioning with helical blades at elevated Reynolds numbers, is detailed in [91]. Considerable importance is attributed to the three-dimensional dynamics and its importance on the evolution of the wake. Theoretical and experimental investigations have indicated a robust interrelation between the object geometry and the dynamics of vortices.

A set of 2D PIV experiments was introduced in [87], conducted within an open-jet wind tunnel using an H-shaped rotor. These experiments demonstrated the potential for the wake profile to exhibit asymmetric behavior, marked by an inclined velocity profile and pronounced expansion, particularly in the windward region. Enhanced momentum replenishment downstream of the turbine is assisted by greater solidity values of the blades, leading to increased cross-stream gradients, as evidenced in the findings of [74]. Thus, a faster recovery appears to result from inducing a destabilization of the wake beforehand. However, the study did not emphasize spanwise effects, such as the activation of vertical transport phenomena.
When analyzing the near wake topology and its evolution in the context of skewed flow conditions, it is essential to account for a confluence of factors, including augmented swept area, the induction effect, and the re-energization of flow derived from the lower half of the turbine. An initial qualitative depiction of the wake evolution is presented in Figure 6.14, illustrating the computed velocity deficit alongside lateral vorticity contours across the plane of $Y/R = 0$. Upon initial observation, it becomes evident that the wake ascends and exhibits augmented energy content, particularly under conditions of greater flow skewness. The positive vorticity observed at the top of the rotor is symmetrically counterbalanced by negative vorticity at the lower part of the rotor when operating under 0 degrees of flow inclination. However, as the turbine tilts, vertical flow components are stimulated, as depicted in Figure 6.15, showcasing the non-dimensional spanwise velocity at $X/R = 1.5$. With increasing inclination angles, the near wake experiences a progressively intensified vertical motion, thereby expediting the recovery of the wake.

Figure 6.16 displays the development of flow patterns at a fixed x/R cross-section downstream from the turbine rotor, while the tilt angle is increased. The wake exhibits an expansion in both the crosswise and spanwise directions. Notably, the windward section of the upper half of the turbine demonstrates the lowest minimum velocity values. However, at higher tilt angles, diminished expansion and reduced magnitude are observed, indicating that the higher kinetic energy content of the 'fresh' air aids in the recovery of the wake. A downstream-propagating low-pressure core becomes evident, maintaining near-symmetry in the spanwise direction when the turbine is in an upright configuration. However, upon tilting the rotor, the depressurized core expands primarily in the upper portion of the rotor. This expansion could be attributed to the unsymmetrical thrust exerted by the rotor on the flow at its lower and upper sections, see in Figure 6.17. This Figure reveals that the fundamental physical origin of flow entrainment within the wake, facilitating its upward motion and significantly enhancing wake recovery, is rooted in the spanwise asymmetry of the pressure field due to the tilted operation condition.

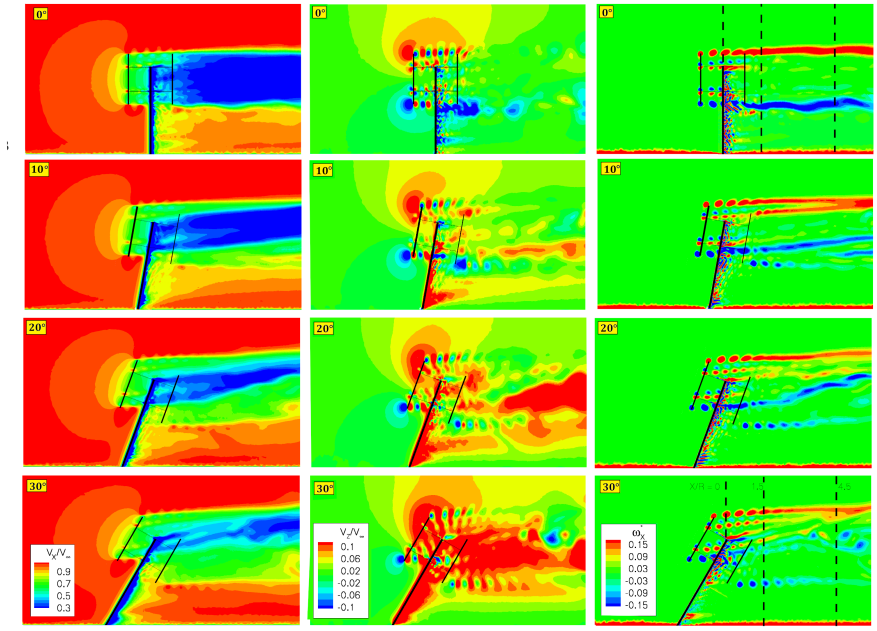

Figure 6.14: TSR=3.54: non-dimensional streamwise and spanwise velocity (left, middle) and lateral vorticity (right) at $Y/R = 0$ plane; tilting angle 0-30 degrees (top-bottom)

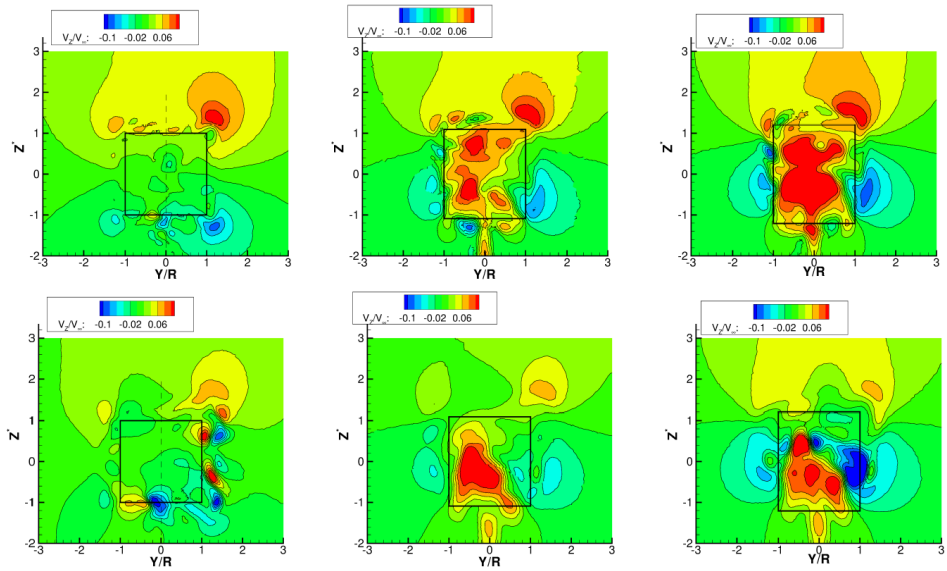

(a) 0° (b) 20° (c) 30°

Figure 6.15: TSR=3.54: non-dimensional, spanwise velocity at $X/R = 1.5, 4.5$ (top,bottom) downstream the rotor at varying tilting angles

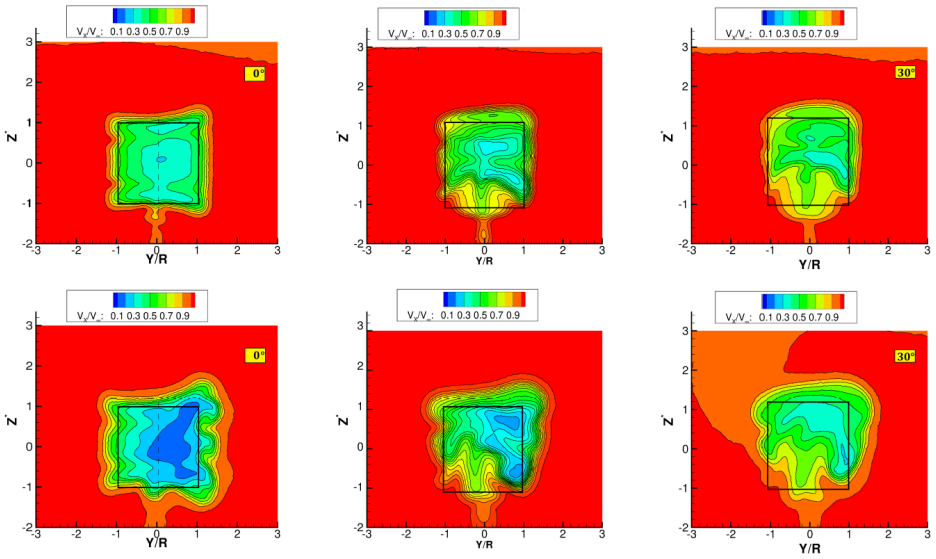

(a) 0° (b) 20° (c) 30°

Figure 6.16: TSR=3.54: non-dimensional, time-averaged streamwise velocity for 0,20, 30 degrees of tilt angle (top,bottom), at three near wake YZ cross-sections, $X/R = 1.5, 4.5$ (top,bottom)

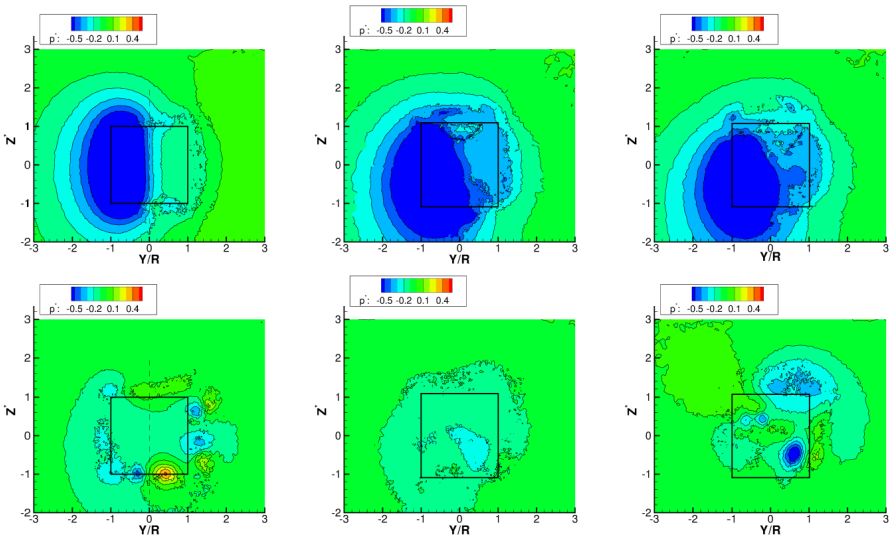

(a) 0° (b) 20° (c) 30°

Figure 6.17: TSR=3.54: non-dimensional, time-averaged gauge pressure for 0, 20 and 30 degrees of tilt angle, at two near wake YZ cross-sections, $X/R = 1.5, 4.5$ (top,bottom))

To provide a more comprehensive description of the wake's physics, Figure 6.18 presents a comparison between the wake generated by the rotor in an upright configuration and the wake at tilt angles of 10 and 30 degrees. The time-averaged velocity profiles captured at midspan reveal alterations in the wake's shape, width, and depth. At $X/R = 1.5$, the upright and both inclined solutions exhibit a close resemblance, particularly at a 10-degree tilt, with the latter showing a diminished velocity deficit. However, as we progress downstream to $X/R = 4.5$, the disparity becomes more pronounced, primarily concentrated on the wake side due to the windward blade's movement. The alteration in the wake could be attributed to the vertical motion originating from the lower half of the turbine. This flow movement is interconnected with the recovery and asymmetry of the wake, contributing to the torque trends depicted in Figure 6.11.
The study of near-wake progression must encompass the impacts of unsteady vortical structures generated by the blades, as well as their evolution and interaction within and behind the rotor. Tescione *et.al* [87] delved into the analysis of asymmetric induction fields within the wake, along with the intricate dynamics of tip and strut-induced vortices. Their study highlighted a heightened expansion on the windward side and the occurrence of vertical stretching and diffusion of flow structures. Furthermore, when examining higher degrees of flow skewness, the velocity defect profiles exhibit asymmetry, with a discernible decrease in defect on the windward side.

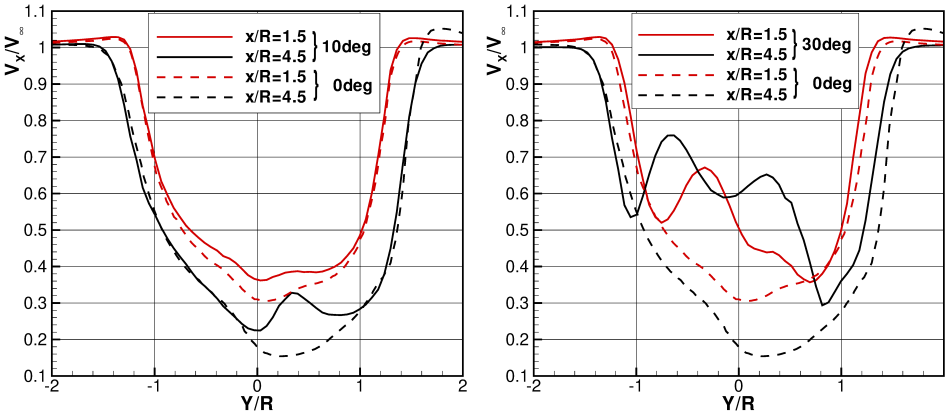

Figure 6.18: TSR=3.54: velocity defect at $X/R = 1.5$ in upright and tilted configuration

Figure 6.19 presents a sequence of streamwise velocity profiles computed at midspan for turbine inclinations of 10, 20, and 30 degrees. These profiles were captured at specific YZ cross-sections downstream of the turbine rotor. At a 10-degree tilt, an off-centered velocity deficit emerges, which grows in significance as we move downstream. Despite this, the various streamwise velocity plots exhibit a nearly consistent degree of skewness and a nearly identical replenishment gradient. The overall trend of the velocity deficit across the planes of constant X/R at midspan, observed in the case of a 10-degree inclination, closely mirrors the distribution highlighted under upright conditions. As the tilt angle increases, a more pronounced asymmetry in the velocity distribution becomes evident: the 'leeward' side of the wake displays an accelerated wake recovery, which may also partially influence the windward region (at a 30-degree tilt angle).

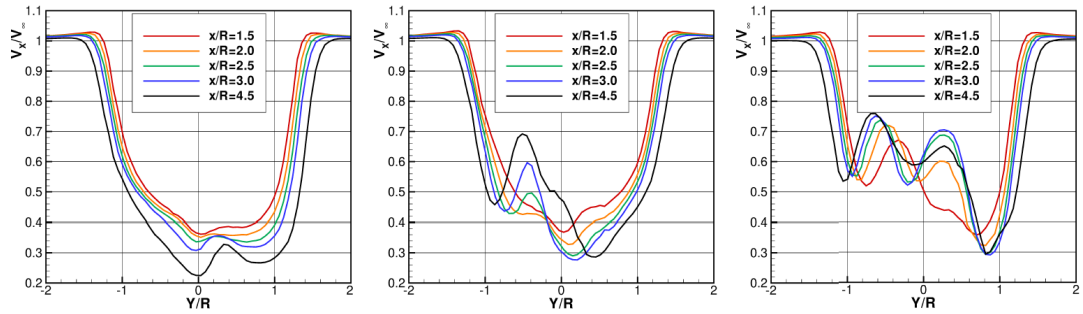

(a) 10° (b) 20° (c) 30°

Figure 6.19: TSR=3.54: non-dimensional, time-averaged streamwise velocity at midspan as a function of the tilt angle at four near wake YZ cross-sections

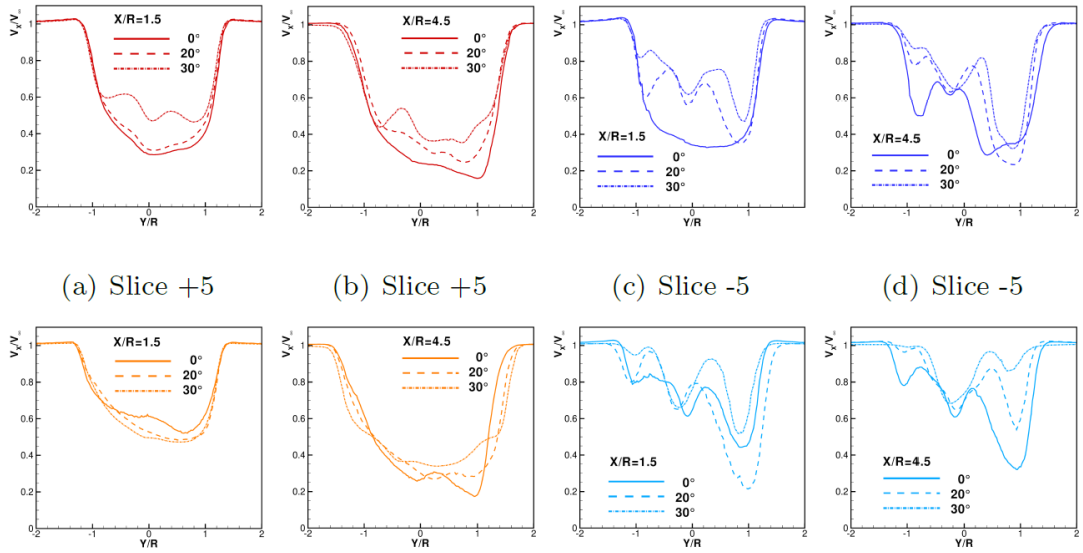

(a) Slice +5 (b) Slice +5 (c) Slice -5 (d) Slice -5

(e) Slice +9 (f) Slice +9 (g) Slice -9 (h) Slice -9

Figure 6.20: TSR=3.54: non-dimensional, time-averaged streamwise velocity at slice $\pm 5, \pm 9$ as a function of the tilt angle at two near wake cross-sections $X/R = 1.5, 4.5$

The described phenomena characterize the distribution of the rotor wake along its span. The impact of flow skewness becomes more evident in Figure 6.20, which presents the streamwise velocity for selected positive and negative slices, specifically ± 5 and ± 9, at two downstream positions: $X/R = 1.5$ and $X/R = 4.5$. By comparing the behavior observed in the near-wake section with that in the farthest one, a quicker recovery of the wake in the lower half of the turbine can be noticed. Additionally, this characteristic is associated with a more pronounced asymmetry in the leeward region and within the negative slices. The profiles of local velocity deficits evolve in a complex manner due to the interaction of vortical structures that form at the solid walls of the blades and interact with one another as they pass through the rotor.

To assess the downstream evolution of the wake, the streamwise velocity deficit was quantified as a function of both tilt angle and downstream position, while keeping the X/R sections fixed. Displayed in Figure 6.21 is the trajectory of the minimum velocity point along the span at $X/R = 1.5, 2.0, 3.0, 4.0$ for the three considered tilt angles. In the case of a 10-degree incline, the positive and negative span positions exhibit an almost symmetrical behavior in relation to the midspan. However, for the 20-degree and 30-degree cases, a reduced velocity deficit becomes evident. Remarkably, when looking at -75% of the semi-span, the largest skew angle predicts around 60% of the freestream velocity, while the medium skew angle predicts only about 20% of the freestream velocity. Through the utilization of a linear least squares interpolation technique, the approximate slope of the velocity profile can be computed.

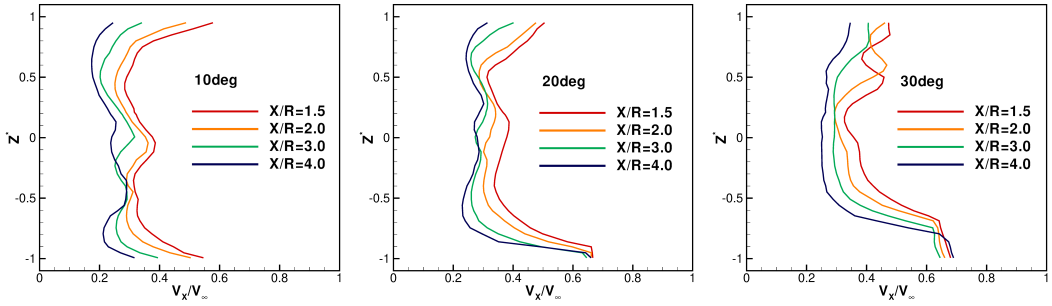

Figure 6.21: Near wake: minimum streamwise velocity loci at $X/R = const$ planes

The graph presented in Figure 6.22 illustrates the collection of these values. The average inclination angle of the wake at each X/R position, derived from the approximate interpolation, offers insights into the wake's orientation.

In the case of the minimum skew condition, the average wake orientation remains approximately within the 10-15 % range. In contrast, for the 20-degree and 30-degree cases, the computed angle surpasses the angle imposed by the skewness.

The predicted average angle demonstrates an ascending trend, with a greater deviation angle corresponding to higher skew angles. This observation implies a progression in the "average" wake angle downstream under the selected conditions. Moreover, this suggests that the faster velocity recovery is promted by the vertical velocity components that transport the vortical structures towards the upper part of the turbine rotor.

To provide further support for the interpretation outlined earlier, Figure 6.23 illustrates the alterations in vortical structures within the rotor due to the presence of skewness. The distribution of streamwise vorticity indicates that the trailing vortex system, originating at the lower portion of the swept cylinder, along with the vortices generated by the lower strut, tend to shift upward with increased flow skewness. In contrast, the upper section of the rotor displays less pronounced vortex pairs. When lower flow skew angles are present, the spanwise vortical structures exhibit a more symmetric arrangement. However, these structures adopt an asymmetric configuration as higher skew angles come into play.

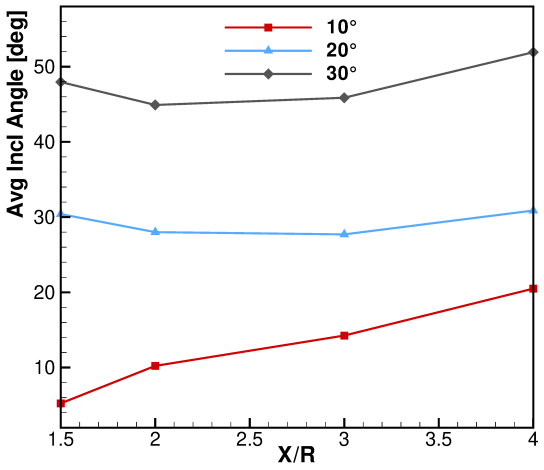

Figure 6.22: Near wake trend: average wake orientation angle from linear minimum least square approx of minimum velocity locus at $X/R = const$ planes

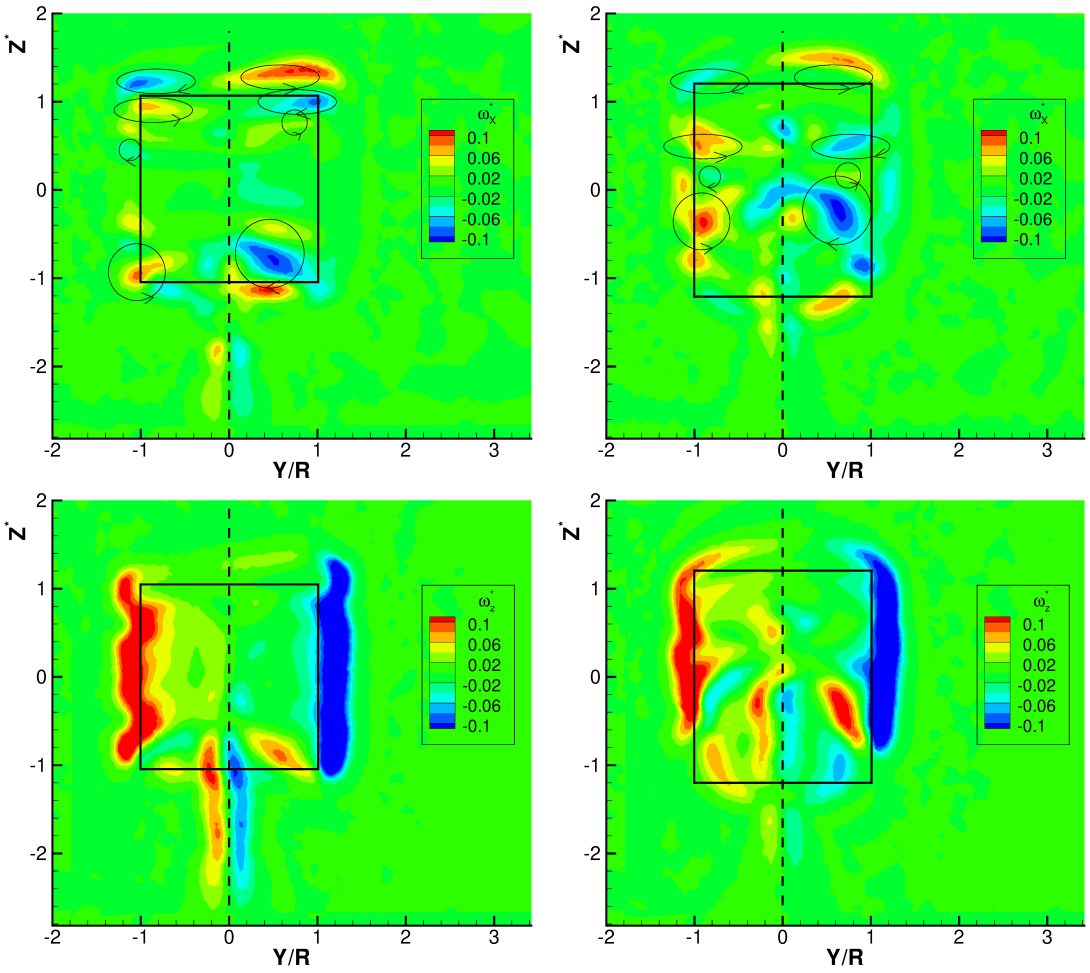

Figure 6.23: TSR=3.54 at 10 and 30 deg tilt angle condition: non-dimensional, time-averaged streamwise/spanwise vorticity, at near X/R=1.5

Chapter 7

Conclusions and Future Work

7.1 Case of study conclusions

The flow field around the VAWTs is characterized by unsteady and turbulent motion, giving rise to complex vortical structures that interact with the solid surfaces of the blades, the shaft, and the struts(if considered). In fact, in the assessment of VAWT performance, multiple factors assume significant roles and exhibit intricate interdependencies that collectively, albeit nonlinearly, contribute to defining the ultimate operational capacity of the machine. As anticipated, this particular type of wind turbine exhibits significant promise for offshore applications. Consequently, in addition to considering well-known design factors such as the shape, number of blades, aspect ratio, solidity, viscous losses, etc., it's important to investigate how flow skewness can impact the operational characteristics of the turbine.

The work was focused on three different VAWTs:

1: Troposkein

The first case of study in this Ph.D. dissertation delved into an extensive computational exploration of the aerodynamic properties and energy conversion potential of a troposkein vertical axis wind turbine. This turbine serves a dual purpose, serving as a scaled-down laboratory model for utility machinery and a practical, real-world solution for distributed power generation within communities. The rotor had previously undergone experimental study under carefully controlled conditions, during which its performance and wake characteristics were measured. These measurements have been employed within this work to evaluate the accuracy of the simulation model.

To address the computational challenges associated with the simulations of the flow around this rotor, multiple mesh configurations were used for both 2D-equatorial and complete 3D models. After thorough testing, an optimal grid resolution of 32 million elements was identified. This resolution ultimately resulted in satisfactory predictions of power coefficient and very good outcomes in terms of wake width and deficit within the examined operational conditions, which range from peak power coefficient to higher tip-speed ratios. An assessment of turbulence models was also carried out, utilizing multiple wall-resolving models, including the k-ω SST model in both its fully turbulent and low-Reynolds formulations, as well as the Spalart-Allmaras model. The 3D results indicated that, under conditions approaching the maximum Tip-Speed Ratio (TSR), the low-Reynolds version of the k-ω SST model showed better performance than SA, while the opposite trend was observed near the peak efficiency condition.
The computed flow fields were utilized to analyze the aerodynamics of the rotor and its wake,

highlighting notable distinctions compared to the established characteristics of conventional H-shape rotors. Specifically, a substantial reduction in energy conversion capability has been observed in the tip portion of the rotor blades, and the associated decrease in performance has been quantified. The rotor wake was observed to be marginally influenced by the prominent tip vortex, which commonly features in H-shape rotor wakes. The slanted configuration of the rotor, on the other hand, generates upwash and downwash flows, leading to the formation of different types of tip vortices, which are confined to specific regions near the rotor's tip mast.

The CFD model was employed to derive design recommendations for turbines within this category. This involved comparing the conventional slanted blade configuration (achieved by bending a straight blade with a uniform profile) with a blade having a uniform profile across its span (a more intricate manufacturing process). The analysis has demonstrated that the thickening of the profile resulting from the blade bending manufacturing offers a net advantage in the peak power condition. However, only minimal differences are observed at high load condition. This implies that a more cost-effective manufacturing process is advisable, not only for structural considerations but also from an aerodynamic perspective.

2: DeepWind

The second case of study has showcased numerical outcomes outcomes of the small-scale model known as the Deepwind Demonstrator. This encompasses assessments in both its upright and tilted conditions, along with an examination of how its performance shifts from a demonstrator scale to a utility-scale. These discoveries have been compared and validated with results obtained from wind tunnel experiments. Followed by a discussion regarding the numerical setup, encompassing boundary extension, grid resolution, and modeling methodology, based on 2D and 3D calculations.
Specifically, the operation of the rotor in a tilted position, which corresponds to the nominal condition for the spar-type floating structure of the DeepWind turbine, has been determined to be less efficient compared to the standard upright rotor configuration found on fixed-bottom towers. Calculations indicate that the aerodynamics of the rotor are adversely affected by the tilt, and the troposkein shape of the rotor does not allow for compensation through a larger swept area, as is the case with H-shaped rotors. An examination of performance across the span of the rotor offers a clear insight into the functioning of each section of the turbine. It reveals that in tilted conditions, the lower half of the rotor below the equatorial section significantly outperforms the upper half above the midspan. This is attributed to the favorable combination between the tilt and the inclination of the blade stacking line. This finding holds significant implications for the development of innovative rotor configurations in the future, which could capitalize on the asymmetric aerodynamics of the rotor during tilted operation.
In order to underscore the engineering relevance of the machine, a utility-scale model of the turbine has also been simulated, in the upright standing position, to evaluate the Reynolds number effect. The outcomes reveal an overall enhancement in the rotor's efficiency due to a postponed flow separation, particularly noticeable in the leeward phase of each revolution. In numerical terms, the simulations validate the machine's ability to achieve relatively high-performance levels, offering valuable insights for its prospective installations.

3: H-shaped

In the third case of study, which pertains to the H-shaped VAWT operating in both upright and tilted conditions, an extensive CFD investigation has been conducted using a high-resolution approach based on URANS discretization. The study aimed to examine the impact of rotor tip and strut losses under various flow conditions, including the tilted configuration with different

angles. The CFD simulations have been meticulously configured with appropriate discretization parameters to ensure cost-effective and dependable computational results. The CFD setup employed in this chapter is identical to that used for the preceding cases, which has undergone rigorous validation against experimental data.

The overall behavior has been investigated by considering the individual contributions of distinct parts of the machine. The significance of a localized spanwise analysis becomes even more pronounced when the turbine operates at tilted positions. The chapter presented a detailed description of the physical issues occurring within the rotor ranging between upright and 30 degrees of inclination. The computed results highlighted the relevance of fresh air encountering the lower part of the turbine. A different wake establishment and recovery has been described by promoted vertical movement inside the rotor. A suction effect drives the flow upwards and as the inclination angle increases, the wake develops with angles even larger than the value imposed by the prescribed inclination. A comprehensive analysis of wake mitigation has been conducted, involving the examination of the flow field generated behind the rotor. Additionally, information regarding the mean angle of wake development has been presented, demonstrating the advantages of employing a tilted condition in the perspective of wind farm optimization.

7.2 General observations

- The exclusive utilization of URANS in this doctoral study endures, primarily due to its demonstrated capability to yield excellent results in comparing the flow field and wake (Exp vs CFD), as seen for the first two cases. Despite the imperative acknowledgment of noticeable discrepancies between computationally derived power coefficient (Cp) values obtained through CFD and those acquired experimentally, these variations are intricately tied to the effectiveness of the discretization methodology. While recognizing the necessity to enhance simulation precision and achieve a closer alignment with experimental Cp values, implementing Large Eddy Simulation (LES) modeling is considered a potentially advantageous strategy, albeit one that entails a very high computational cost.

- Several relevant outcomes have been achieved during this Ph.D. work. Complex three-dimensional fields have been thoroughly studied in detail to shed light on the physical issues underlying the aerodynamic performance of VAWTs characterized by different designs. Local investigation of the aerodynamic performance, possibly operated in tilted conditions, has highlighted peculiar features of the Troposkien design that have not been commented on in much detail, earlier: i) Larger swept areas can be penalized by adverse aerodynamic conditions, ii) The stocking line inclination play a relevant role in tilted position mainly in the lower part of the rotor, iii) Up to sixty percent of the total power can be gathered by lower part of the machine. Time-averaged analysis of the near wake have shown the presence of the vertical vortices promoted by the rotor skewness.

- In the H-shaped design vortical structures have also been found in a tilted configuration. The structure of the near wake has been evaluated both from a qualitative point of view and also quantified to predict its evolution. The results highlighted the relevance of fresh air in the lower part of the machine, enhancing the harvesting capability of this rotor region. A wake establishment and evolution have been predicted at different tilted positions and the results obtained suggested a wake mitigation due to the suction effect inside the rotor.

Original evaluation of the blade design in the presence of skewed flow conditions finally provided useful indications to opt to design innovative wind rotors, as reported in the next section (Future work).

7.3 Future work

Starting from the observations carried out on the behavior of the H-shaped rotor presented in Chapter 6, this section aims to highlight relevant physical outcomes of the work and to exploit possible new designs. Reference is first made to the power and torque coefficients predicted for the H-shaped rotor at 20 degrees of inclination. For the sake of easiness, former figure 6.8 and 6.10 are reproposed herein in the following. These data results are of interest because allow to draw considerations about a relevant operating condition of VAWTs in the presence of skewed flows.

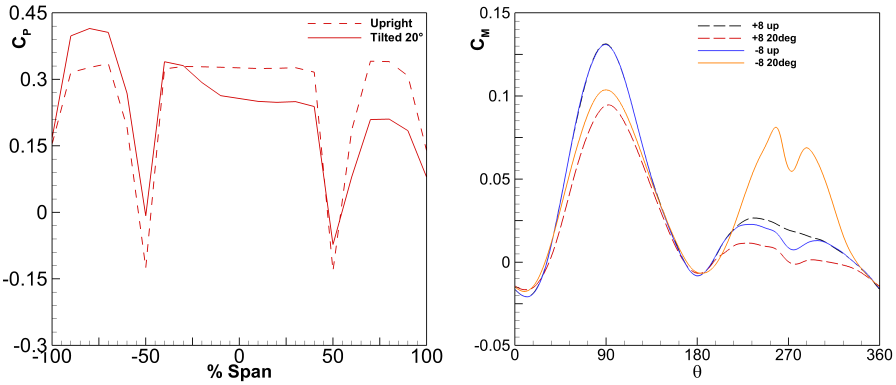

Figure 7.1: 3D Performance at TSR=3.54: upright in comparison to 20deg: $C_{p,loc}$, from bottom (-100%) to top (100%) (left) and Cm±8 (right).

As discussed in the respective section, the lower portion of the machine (from -100 to 0) experiences a notable increase in Cp with respect to the upright condition, attributable to the dual encounter with fresh air (upwind and downwind). However, this advantage diminishes the performance of the upper part of the machine (from 0 to +100), which is affected by tilting (reduced relative speed) without the benefit of encountering fresh air in the downwind region. This leads to reasoning on how to potentially retain the advantage of the lower zone while alleviating the disadvantageous effect on the upper part.

Taking advantage of the understanding and outcomes obtained and fully described in the former chapters, two modified H-V-shaped VAWTs have been designed and presented in the following aiming at an improved performance level. see Figure 7.2.
First of all the baseline configuration is defined as follows:

- **H**: The configuration stems from the analysis presented in the H-shaped Chapter XX. Here, the number of struts is reduced to one, and the turbine aspect ratio is increased to 1.2. This setup allows to get indications also about the negative impact of struct on performance under tilted conditions. A single connecting element has been used also in virtue of the employed aspect ratio.

Two different tilted HV-rotors are considered as below reported.

- **Hv1**: This solution is conceived to preserve the benefit of the lower part while mitigating the tilting effect on the upper section, particularly in the upwind region where torque production is at its peak. It's worth noting that in the upper part of this configuration, there

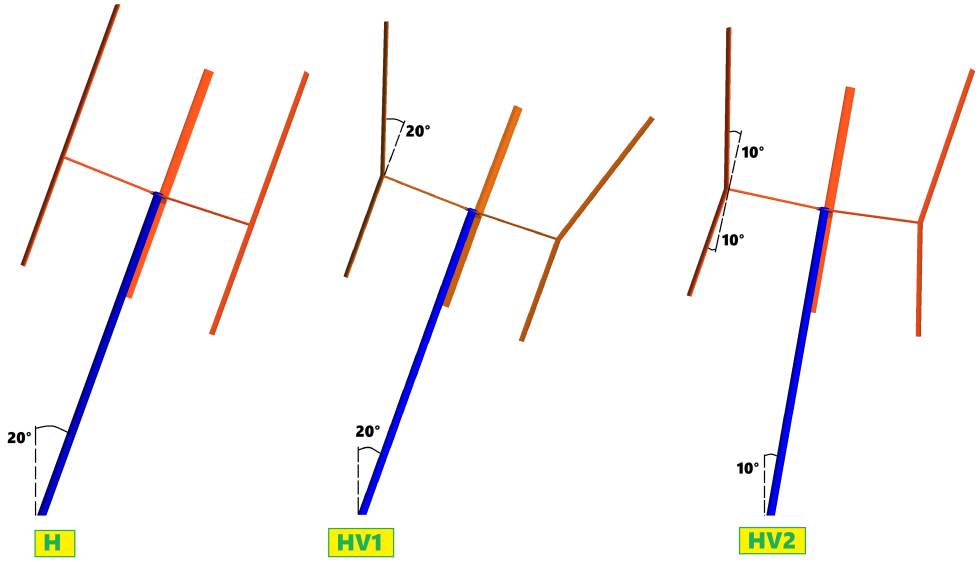

Figure 7.2: Future work: Different H-shaped configurations

is an increase in diameter, resulting in an elevated TSR and a reduction in solidity. Additionally, there is a variation in the swept area. Therefore, the impact of these parameters will be studied and taken into consideration. Studying these effects could provide valuable insights for optimizing the counter-rotating solution proposed by Norwegian startup, World Wide Wind [3].

- **Hv2**: This solution strikes a balance between reducing the inclination and consequently, minimizing its effect, while ensuring a clean flow in the downwind region through the form in the lower part of the turbine. As it appears at first glance from figure 7.2, this configuration allows the upper rotor part to operate vertically in the upwind zone (around 90 degrees), while enabling the lower rotor part to operate vertically in the downwind zone (around 270 degrees). This operating state shows the advantage that in the latter zone, the lower turbine part should encounter clean flow, except for the tower's effect.

The combined effect of fresh air, re-energization from bottom to top promoted by the joint effect of the rotor design and tilting must be properly addressed to actually handle the design and possibly get enhanced performance level. The new designed VAWTs, presented and discussed in this section, are both based on the use of a single holding strut, three blades of equal length, sharing the same airfoil profile, but featuring different blade definitions.

Nomenclature

c	blade chord $[m]$
eq	equatorial
f	frequency $[s^{-1}]$
k	turbulent kinetic energy $[m^2/s^2]$
AOA	angle of attack
C_M	moment coefficient C_M=M/$(1/4\rho_\infty V_\infty^2 H D^2)$ $[-]$
C_P	power coefficient $C_P = C_M$TSR $[-]$
D	turbine diameter $[m]$
LR	Low-Re version of the $k-\omega$ turbulence model
H	turbine span $[m]$
M	moment $[Nm]$
N	blade number $[-]$
P	power $[W]$
RANS	Reynolds Averaged Navier-Stokes
Re	Reynolds number $[-]$
SST	Shear Stress Transport
SA	Spalart-Allmaras
TSR	Tip Speed Ratio $[-]$
Tu	turbulence intensity Tu= $\sqrt{2k/3}/V_\infty$ $[-]$
U	peripheral velocity $[m/s]$
V	absolute velocity $[m/s]$
HAWT	horizontal-axis wind turbine
VAWT	vertical-axis wind turbine

FOWT	floating offshore wind turbine
X	streamwise coordinate $[m]$
Y	lateral coordinate $[m]$
W	relative velocity $[m/s]$
Z	spanwise coordinate $[m]$
α	angle of attack $[deg]$
β	half wake angle $[deg]$
δ	half wake thickness $[m]$
ρ	air mass density $[kg/m^3]$
σ	solidity $\sigma = Nc/D[-]$
ω	vorticity $[1/s]$
θ	azimuthal angle $[deg]$
∞	freestream
sw	swept position
up	upright position
$*$	non-dimensional

Bibliography

[1] https://www.energy.gov/eere/wind/articles/offshore-wind-market-report-2021-edition-released [Accessed: (September 2023)].

[2] https://seatwirl.com/ [Accessed: (September 2023)].

[3] https://worldwidewind.no/ [Accessed: (September 2023)].

[4] https://docs.qblade.org/src/theory/aerodynamics/lifting_line/lifting_line.html [Accessed: (September 2023)].

[5] Darrieus GJM. Turbine having its rotating shaft transverse to the flow of the current. US Patent no. 1.835.018, 1931.

[6] A.Rezaeiha, I.Kalkamn, and B.Blocken. "CFD simulation of a vertical axis wind turbine operating at a moderate tip speed ratio: guidelines for minimum domain size and azimuthal increment". In: *Renewable Energy* 107 (2017), pp. 373–385.

[7] Thomas D Ashwill, Herbert J Sutherland, and Dale E Berg. "A retrospective of VAWT technology." In: *Reports SANDIA2012* (2012).

[8] Muhammad Mahmood Aslam Bhutta et al. "Vertical axis wind turbine – A review of various configurations and design techniques". In: *Renewable and Sustainable Energy Reviews* 16 (2012), pp. 1926–1939.

[9] Peter Bachant et al. "Experimental Study of a Reference Model Vertical-Axis Cross-Flow Turbine". In: *PLOS ONE* 11 (2016), pp. 1–20.

[10] Francesco Balduzzi et al. "Critical issues in the CFD simulation of Darrieus wind turbines". In: *Renewable Energy* (2016).

[11] Francesco Balduzzi et al. "Darrieus wind turbine blade unsteady aerodynamics: a three-dimensional Navier-Stokes CFD assessment". In: *Energy* (2017).

[12] Francesco Balduzzi et al. "Dimensionless numbers for the assessment of mesh and timestep requirements in CFD simulations of Darrieus wind turbines". In: *Energy* 97 (2016), pp. 246–261.

[13] Francesco Balduzzi et al. "Feasibility analysis of a Darrieus vertical-axis wind turbine installation in the rooftop of a building". In: *Applied Energy* 97 (2012), pp. 921–929.

[14] Galih Bangga et al. "Improved double-multiple-streamtube approach for H-Darrieus vertical axis wind turbine computations". In: *Energy* (2019).

[15] L. Battisti et al. "Experimental benchmark data for H-shaped and troposkien VAWT architectures". In: *Renewable Energy* 125 (2018), pp. 425–444.

[16] L. Battisti et al. "Normalized performance and load data for the deepwind demonstrator in controlled conditions". In: *Data in Brief* (2016).

[17] L. Battisti et al. “Wind tunnel testing of the DeepWind demonstrator in design and tilted operating conditions”. In: *Energy* 111 (2016), pp. 484–497.

[18] Lorenzo Battisti et al. “Analysis of Different Blade Architectures on small VAWT Performance”. In: *Journal of Physics: Conference Series* (2016).

[19] Gabriele Bedon et al. “Aerodynamic Benchmarking of the Deepwind Design”. In: *Energy Procedia* 75 (2015), pp. 677–682.

[20] Gabriele Bedon et al. “Computational assessment of the DeepWind aerodynamic performance with different blade and airfoil configurations”. In: *Applied Energy* 185 (2017), pp. 1100–1108.

[21] Alessandro Bianchini et al. “A Critical Analysis on Low-Order Simulation Models for Darrieus Vawts: How Much Do They Pertain to the Real Flow?” In: *Journal of Engineering for Gas Turbines and Power* (2018).

[22] B F Blackwell, R E Sheldahl, and L V Feltz. “Wind tunnel performance data for the Darrieus wind turbine with NACA 0012 blades”. In: *Technical report SANDIA* (1976).

[23] B.F. Blackwell and R.E. Sheldahl. “Selected wind tunnel test results for the Darrieus wind turbine”. In: *Journal of Energy* 1 (1977), pp. 382–386.

[24] S. Brusca and M Lanzafame R.and Messina. “Design of a vertical-axis wind turbine: how the aspect ratio affects the turbine’s performance”. In: *International Journal of Energy and Environmental Engineering* 5 (2014).

[25] S. Brusca, R. Lanzafame, and Michele Messina. “Design of a vertical-axis wind turbine: how the aspect ratio affects the turbine’s performance”. In: *International Journal of Energy and Environmental Engineering* 5 (2014), pp. 1–8.

[26] Philippe Chatelain et al. “Vortex Particle-Mesh simulations of Vertical Axis Wind Turbine flows: from the blade aerodynamics to the very far wake”. In: *Journal of Physics: Conference Series* (2016).

[27] Zhengshun Cheng et al. “Effect of the number of blades on the dynamics of floating straight-bladed vertical axis wind turbines”. In: *Renewable Energy* 101 (2017), pp. 1285–1298.

[28] “Comparison of low-order aerodynamic models and RANS CFD for full scale 3D vertical axis wind turbines”. In: *Renewable Energy* 109 (2017), pp. 564–575.

[29] F N Coton, R A McD Galbraith, and D Jiang. “The Influence of Detailed Blade Design on the Aerodynamic Performance of Straight-Bladed Vertical Axis Wind Turbines”. In: *Proceedings of the Institution of Mechanical Engineers, Part A: Journal of Power and Energy* 210.1 (1996), pp. 65–74.

[30] Valerio D’Alessandro, Sergio Montelpare, and Renato Ricci. “Assessment of a Spalart–Allmaras Model Coupled with Local Correlation Based Transition Approaches for Wind Turbine Airfoils”. In: *Applied Sciences* 11 (2021).

[31] V. Dossena et al. “An Experimental Study of the Aerodynamics and Performance of a Vertical Axis Wind Turbine in a Confined and Unconfined Environment”. In: *Journal of Energy Resources Technology* (2015).

[32] Sandra Eriksson, Hans Bernhoff, and Mats Leijon. “Evaluation of different turbine concepts for wind power”. In: *Renewable and Sustainable Energy Reviews* (2008).

[33] F.Huijs et al. “Integrated design of a semi-submersible floating vertical axis wind turbine (vawt) with active blade pitch control”. In: *Journal of Physics* 1104 (2018), pp. 1–12.

[34] F.Ottermo and H.Bernhoff. “An upper size of vertical axis wind turbines”. In: *Wind Energy* 17 (2014), pp. 1623–1629.

[35] C.S. Ferreira. “The near wake of the vawt, 2d and 3d views of the vawt aerodynamics,” in: *Ph.D. thesis, Delft University of Technology* (2009).

[36] Callum Flannigan, James Carroll, and William Leithead. “Operations expenditure modelling of the X-Rotor offshore wind turbine concept”. In: *Journal of Physics: Conference Series* 2265 (2022).

[37] N. Franchina, G. Persico, and M. Savini. “2D-3D Computations of a Vertical Axis Wind Turbine Flow Field: Modeling Issues and Physical Interpretations”. In: *Renewable Energy* 136 (2019), pp. 1170–1189.

[38] N. Franchina et al. “Three-dimensional modeling and investigation of the flow around a troposkein vertical axis wind turbine at different operating conditions”. In: *Renewable Energy* 199 (2022), pp. 368–381.

[39] Nicoletta Franchina et al. “Three-dimensional CFD simulation and experimental assessment of the performance of a H-shaped vertical axis wind turbine at design and off-design conditions”. In: *International Journal of Turbomachinery, Propulsion and Power* 4 (2019).

[40] Snorri Gudmundsson. *General aviation aircraft design: Applied Methods and Procedures*. Butterworth-Heinemann, 2013.

[41] H.Y. Peng H.F. Lam. “Study of wake characteristics of a vertical axis wind turbine by two- and three-dimensional computational fluid dynamics simulations,” in: *Renewable Energy* (2016).

[42] Mazharul Islam, Amir Fartaj, and Rupp Carriveau. “Analysis of the design parameters related to a fixed-pitch straight-bladed vertical axis wind turbine”. In: *Wind engineering* (2008).

[43] T.Nguyen J.H. Strickland B.T. Webster. “A vortex model of the Darrieus turbine: An analytical and experimental study”. In: *Journal of Fluids Engineering* (1976).

[44] Eastman N Jacobs and Albert Sherman. “Airfoil section characteristics as affected by variations of the Reynolds number”. In: *NACA Technical Report* (1937).

[45] J. M. Jonkman and D. Matha. “Dynamics of offshore floating wind turbines—analysis of three concepts”. In: *Wind Energy* 14 (2011), pp. 557–569.

[46] Samuel Kanner and Per-Olof Persson. “Validation of a High-Order Large-Eddy Simulation Solver Using a Vertical-Axis Wind Turbine”. In: *AIAA Journal* 54 (2016), pp. 101–112.

[47] Matthias Kinzel, Quinn Mulligan, and John O. Dabiri. “Energy exchange in an array of vertical-axis wind turbines”. In: *Journal of Turbulence* 13 (2012), pp. 50–67.

[48] Brian Kinloch Kirke. “Evaluation of self-starting vertical axis wind turbines for stand-alone applications”. PhD thesis. Griffith University Australia, 1998.

[49] Sébastien Le Fouest and Karen Mulleners. “The dynamic stall dilemma for vertical-axis wind turbines”. In: *Renewable Energy* (2022).

[50] Chao Li et al. “2.5D large eddy simulation of vertical axis wind turbine in consideration of high angle of attack flow”. In: *Renewable Energy* (2013).

[51] H. Li and Z. Chen. “Overview of different wind generator systems and their comparisons”. In: *IET Renewable Power Generation* 2 (2008), pp. 123–138.

[52] Qing’an Li et al. “Study on power performance for straight-bladed vertical axis wind turbine by field and wind tunnel test”. In: *Renewable Energy* (2016).

[53] M.Collu et al. “FLOVAWT: further progress on the development of a coupled model of dynamics for floating offshore VAWTs”. In: *Proceedings of the ASME Turbo Expo* (2014).

[54] E.Aoun M.Elkhoury T.Kiwata. “Experimental and numerical investigation of a three-dimensional vertical-axis wind turbine with variable-pitch,” in: *J. Wind Eng. Ind. Aerodyn* (2015).

[55] Claessens MC. *The design and testing of airfoils for application in small vertical axis wind turbines*. 2006.

[56] R.A. McAdam, G.T. Houlsby, and M.L.G. Oldfield. “Experimental measurements of the hydrodynamic performance and structural loading of the transverse horizontal axis water turbine: Part 2”. In: *Renewable Energy* 59 (2013), pp. 141–149.

[57] Jade McMorland et al. “A review of operations and maintenance modelling with considerations for novel wind turbine concepts”. In: *Renewable and Sustainable Energy Reviews* (2022).

[58] Andrés Meana-Fernández et al. “Parametrical evaluation of the aerodynamic performance of vertical axis wind turbines for the proposal of optimized designs”. In: *Energy* 147 (2018), pp. 504–517.

[59] Andrés Meana-Fernández et al. “Parametrical evaluation of the aerodynamic performance of vertical axis wind turbines for the proposal of optimized designs”. In: *Energy* 147 (2018), pp. 504–517.

[60] Victor Mendoza and Anders Goude. “Validation of Actuator Line and Vortex Models Using Normal Forces Measurements of a Straight-Bladed Vertical Axis Wind Turbine”. In: *Energies* 13 (2020).

[61] F.R. Menter. “Two-equation eddy-viscosity turbulence model for engineering applications”. In: *AIAA Journal* 32 (1994), pp. 1598–1605.

[62] P. G. Migliore, W. P. Wolfe, and J. B. Fanucci. “Flow Curvature Effects on Darrieus Turbine Blade Aerodynamics”. In: *Journal of Energy* (1980).

[63] Laurence Morgan and William Leithead. “Aerodynamic modelling of a novel vertical axis wind turbine concept”. In: *Journal of Physics: Conference Series,* 2257 (2022).

[64] N.Franchina, G.Persico, and M.Savini. “Three-dimensional unsteady aerodynamics of a H-shaped vertical axis wind turbine over the full operating range”. In: *Journal of Wind Engineering & Industrial Aerodynamics* 206 (2020).

[65] S.Shibuya N.Fujisawa. “Observations of dynamic stall on Darrieus wind turbine blades,” in: *Journal of Wind Engineering* (2001).

[66] A. Orlandi et al. “3D URANS analysis of a vertical axis wind turbine in skewed flows”. In: *Journal of Wind Engineering and Industrial Aerodynamics* (2015).

[67] B C Owens and D T Griffith. “Aeroelastic stability investigations for large-scale vertical axis wind turbines”. In: *Journal of Physics* 524 (2014).

[68] P.Bachant and M.Wosnik. “Effects of Reynolds number on the energy conversion and near-wake dynamics of a high solidity vertical-axis cross-flow turbine”. In: *Energies* 9 (2016), pp. 1–18.

[69] Ion Paraschivoiu. *Wind turbine design: with emphasis on Darrieus concept*. Presses inter Polytechnique, 2002.

[70] Uwe S. Paulsen et al. “Outcomes of the DeepWind Conceptual Design”. In: *Energy Procedia* 80 (2015), pp. 329–341.

[71] Uwe Schmidt Paulsen et al. “Deepwind-an innovative wind turbine concept for offshore”. In: *EWEA Annual Event 2011*. European Wind Energy Association (EWEA). 2011.

[72] Uwe Schmidt Paulsen et al. “Design Optimization of a 5 MW Floating Offshore Vertical-axis Wind Turbine”. In: *Energy Procedia* 35 (2013), pp. 22–32.

[73] Giacomo Persico et al. “Time-Resolved Experimental Characterization of the Wakes Shed by H-Shaped and Troposkien Vertical Axis Wind Turbines”. In: *Journal of Energy Resources Technology* (2017).

[74] A. Posa. “Dependence of the wake recovery downstream of a vertical axis wind turbine on its dynamic solidity”. In: *Journal of Wind Engineering & Industrial Aerodynamics* 202 (2020).

[75] P.Klimas R.Sheldahl. “Aerodynamic characteristics of seven symmetrical airfoil sections through 180-degree angle of attack for use in aerodynamic analysis of vertical axis wind turbines”. In: *Technical report SANDIA* (1981).

[76] John M. Rainbird et al. “On the influence of virtual camber effect on airfoil polars for use in simulations of Darrieus wind turbines”. In: *Energy Conversion and Management* 106 (2015), pp. 373–384.

[77] Abdolrahim Rezaeiha, Hamid Montazeri, and Bert Blocken. “Towards accurate CFD simulations of vertical axis wind turbines at different tip speed ratios and solidities: Guidelines for azimuthal increment, domain size and convergence”. In: *Energy Conversion and Management* 156 (2018), pp. 301–316.

[78] A. Rossetti and G. Pavesi. “Comparison of different numerical approaches to the study of the H-Darrieus turbines start-up”. In: *Renewable Energy* 50 (2013), pp. 7–19.

[79] W Roynarin, PS Leung, and PK Datta. “The performances of a vertical Darrieus machine with modern high lift airfoils”. In: *Proceedings from IMAREST conference MAREC*. 2002.

[80] S.Mertens, G.van Kiuk, and G.van Bussel. “Performance of an h-darrieus in the skewed flow on a roof”. In: *ASME Journal of Solar Energy Engineering* 125 (2003), pp. 433–440.

[81] S.Zanforlin and S. DE Luca. “Effects of the Reynolds number and the tip losses on the optimal aspect ratio of straight-bladed vertical axis wind turbines”. In: *Energy* 148 (2018), pp. 179–195.

[82] Andrea G. Sanvito, Vincenzo Dossena, and Giacomo Persico. “Formulation, Validation, and Application of a Novel 3D BEM Tool for Vertical Axis Wind Turbines of General Shape and Size”. In: *Applied Sciences* 11 (2021).

[83] Joseph Saverin et al. “Comparison of Experimental and Numerically Predicted Three-Dimensional Wake Behavior of Vertical Axis Wind Turbines”. In: *Journal of Engineering for Gas Turbines and Power* (2018).

[84] Hidetaka Senga, Hiroki Umemoto, and Hiromichi Akimoto. “Verification of Tilt Effect on the Performance and Wake of a Vertical Axis Wind Turbine by Lifting Line Theory Simulation”. In: *Energies* 15 (2022).

[85] Sina Shamsoddin and Fernando Porté-Agel. “Large Eddy Simulation of Vertical Axis Wind Turbine Wakes”. In: *Energies* (2014).

[86] Jie Su et al. “Investigation of V-shaped blade for the performance improvement of vertical axis wind turbines”. In: *Applied Energy* (2020).

[87] G. Tescione et al. “Near wake flow analysis of a vertical axis wind turbine by stereoscopic particle image velocimetry”. In: *Renewable Energy* 70 (2014), pp. 47–61.

[88] Willy Tjiu et al. “Darrieus vertical axis wind turbine for power generation I: Assessment of Darrieus VAWT configurations”. In: *Renewable Energy* 75 (2015), pp. 50–67.

[89] A.Ramesh U.Divakaran V.R. Kishore. “Effect of wind speed on the performance of a troposkein vertical axis wind turbine,” in: *International J. of Renewable energy research* (2019).

[90] Zhenyu Wang, Yuchen Wang, and Mei Zhuang. “Improvement of the aerodynamic performance of vertical axis wind turbines with leading-edge serrations and helical blades using CFD and Taguchi method”. In: *Energy Conversion and Management* (2018).

[91] N.J. Wei et al. “Near wake structure of full-large scale vertical-axis wind turbines”. In: *Journal Fluid Mechanics* 914 (2021), pp. 1–20.

[92] Wilcox and David C. “Simulation of Transition with a Two-Equation Turbulence Model”. In: *AIAA Journal* 32.2 (1994), pp. 247–255.

[93] Worstell and Mark H. “Aerodynamic Performance of the DOE/Sandia 17-m-Diameter Vertical-Axis Wind Turbine”. In: *Journal of Energy* 5.1 (1981), pp. 39–42.

List of Figures